Jurnal

TEKNOLOGI DIRGANTARA

Journal of Aerospace Technology

Vol. 19 No. 1 June 2021 ISSN 1412- 8063

No : 21/E/KPT/2018

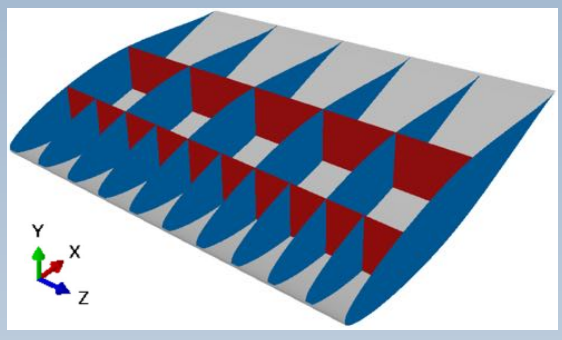

Code	Component	Thickness (mm)
	Skin	0.6
	Spar	1.2
	Rib	0.6

(a)

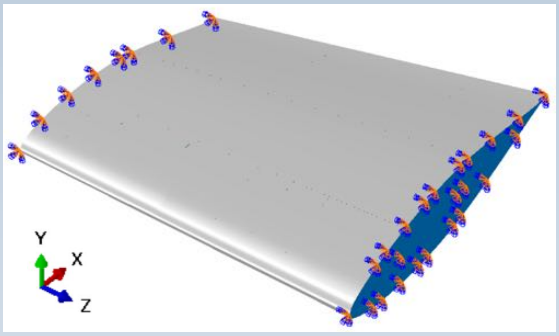

(b)

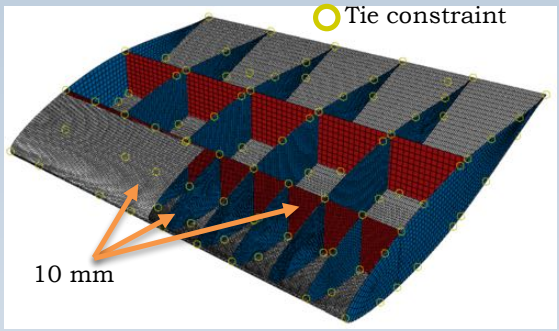

(c)

Publisher :
Lembaga Penerbangan dan Antariksa Nasional (LAPAN)
Bogor - Indonesia

Jurnal
TEKNOLOGI DIRGANTARA
Journal of Aerospace Technology

Vol. 19 No. 1 June 2021 ISSN 1412- 8063

Nomor : 21/E/KPT/2018

Contents

Jurnal TEKNOLOGI DIRGANTARA

Journal of Aerospace Technology

Vol. 19 No. 1 June 2021 ISSN 1412- 8063

Nomor: 21/E/KPT/2018

Cover image: (a) Geometric details, (b) boundary conditions, and (c) element size of the wing

Publisher Mailing Address :

LAPAN, Jl. Raya Lapan No.2 Mekarsari, Rumpin Bogor 16350, Jawa Barat
Email: publikasi@lapan.go.id Web : http://www.lapan.go.id & http://www.jurnal.lapan.go.id

Jurnal
TEKNOLOGI DIRGANTARA
Journal of Aerospace Technology
Vol. 18 No. 2 Desember 2020 ISSN 1412- 8063
Nomor: 21/E/KPT/2018

EDITORIAL

Dear readers,

We present Jurnal Teknologi Dirgantara Vol. 19, No. 1, June 2021 as many as 120 (ten) articles as follows: The Effect of Cross-section and Elliptical Hole Ratio on Crashworthiness Parameters of Crash-Box Structure (Warsiyantto et.al), Investigation of Wire Diameter of Helical Compression Spring for Payload Separation (Laksono), Properties Comparison of Open Hole and Non-Hole Carbon UD-Lycal Composite with Vacuum Bagging Manufacturing Method (Isna, et,al), Information Extraction From Lapan Satellite Ais Database For Ship Classification In The Indonesian Territorial Waters (Nugroho et,al), Powered Landing Guidance Algorithms Using Reinforcement Learning Methods For Lunar Lander Case (Nugroho et.al), Station-Keeping Simulation and Planning for LAPAN-A4 Satellite Using Finite-Burn Thruster (Zuhri and Puetro), Preliminary Power Budget Analysis for Equatorial Low Earth Orbit (LEO) Communication Satellite (Suryanti, et.al), Dynamic response of the wing during UAV collision (Warsyinato, et.al), Research on the Transmissibility of Wire Rope Insulators as Damping Equipment on the RX 200 Rocket Payload (Djatmiko, et.al), Effects of Bleeder Schedule to Fiber Mass Fraction and Composites Surface Topography on Wet Lay-up Manufacturing Process (Dewi, et.al).

Since 2021, the Jurnal Teknologi Dirgantara has published in English. I hope that the readers will benefit from it.

Bogor, June 2021 Editor in Chief

The Effect of Cross-section and Elliptical Hole Ratio on Crashworthiness Parameters of Crash-Box Structure

Budi Aji Warsiyanto[1], Muhammad Hadi Widanto [2], Ilham Musthofa [3], Ichsan Maulana [4], Sahril Afandi Sitompul [5], Endah Yuniarti [6]

[1,2,3,4,5,6]Prodi Teknik Penerbangan, Fakultas Teknologi Kedirgantaraan
Universitas Dirgantara Marsekal Suryadarma
Komplek Bandara Halim Perdanakusuma, Jakarta 13610, Indonesia

e-mail: budiajiwarsiyanto@gmail.com

Received: 19-09-2020. Accepted: 24-02-2021. Published: 30-06-2021

Abstract

This paper assesses computationally the thin-walled column structure with multi-cell and aluminum alloy 6061-O against dynamic compression in the axial direction. The dynamic explicit was employed in the Abaqus code to study characteristics of the cross-section differences. The complex proportional assessment (COPRAS) method was employed to determine a configuration that complies with the indicator parameters. The chosen cross-section configuration is further enhanced by creating elliptical holes with different diameter ratios. The results show that the thin-walled column structure with a nine-cell cross-section accompanied by an elliptical hole ratio of 0.3 indicates the potential corresponding to the indicator parameters for the crashworthiness application.

Keywords: *thin-walled column, cross-section, crashworthiness, hole, complex proportional assessment*

1. Introduction

Crashworthiness is the ability of the vehicle structure to experience deformation due to controlled crashing forces to protect passengers. Crashworthiness is also highly dependent on how the materials, construction, and design of the vehicle (Daehn, 2014).

The thin-walled column structure is used as energy absorbers and widely applied in the field of transportation, aerospace, military equipment, and other industries which have the advantages of lightweight, energy absorption capacity, low price, high strength, and stiffness (Sun et al., 2015). The thin-walled column structure is usually found in the part that functions to withstand the impact load as shown in Figure 1-1. Thin-walled columns with AA6061-O material were found to be an efficient energy-absorbing component (Zhang & Zhang, 2013).

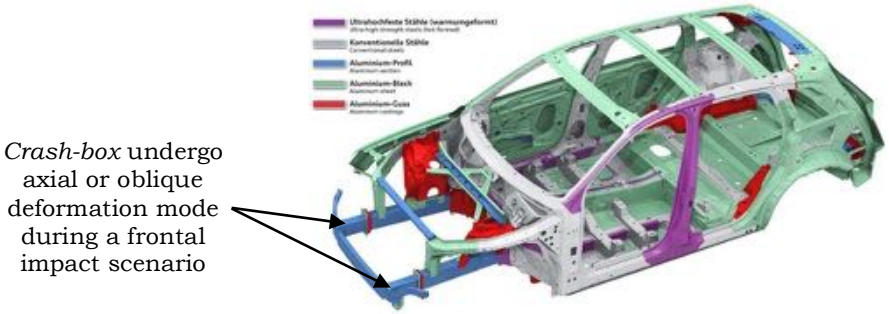

Figure 1-1: Crash-box location on vehicle structure (Baroutaji et al., 2017)

Previously, the energy-absorbing behavior of thin-walled structures has been conducted under axial and oblique loading in many studies (Baroutaji et al., 2017). A difference of the thin-walled column structures with different cross-sections such as circular, rectangle, square, hexagonal, octagonal, and ellipse (Tarlochan et al., 2013).

In 2014 – 2018, 144000 deaths were reported due to accidents in Indonesia (BPS-Statistics, 2018). The traffic accident death rate per 100,000 population stands at 12. This figure shows a very high rate compared to Singapore with 4.8 and Australia 5.2. Most researchers assume that the traffic accident death rate in Indonesia is still not fully reported. Also, the data are inconsistent and difficult to verify. Based on the trend of traffic accident death data, it is estimated that in 2020 traffic accident deaths in Indonesia will reach 40,000 per year. In fact, for the year 2035, it is estimated that there will be 65,000 traffic accident deaths per year.

Crash-box research has been carried out extensively with various cross-section configurations to obtain high energy absorption ($\boldsymbol{EA}$) and low peak crushing force ($\boldsymbol{F_{max}}$), both by numerical and experimental methods. Several researchers, such as (Chen & Wierzbicki, 2001) conducted tests on one-, two-, and three-cell columns. The test results show that the energy absorption efficiency of the three-cell column (Figure 1-2 (a)) is higher than that of the one- and two-cell columns. (Kim, 2002) optimized multi-cell cross-section configuration with four elements in each corner. The results show that the cross-section configuration of the four square elements (Figure 1-2 (b)) has a higher EA value than the circular elements. (Hou et al., 2008) conducted research on the column structure with one-, two-, three-, and four-cell cross-sections. The results show that the four-cell cross-section increases EA and minimizes F_{max} as shown in Figure 1-2 (c). (Zhang & Cheng, 2007) conducted a numerical study of the energy absorption characteristics between foam-filled square columns and multi-cell square columns. The results showed that the nine-cell column as shown in Figure 1-2 (d) was 50-100% more efficient in absorbing energy than the column filled with foam. (Najafi & Rais-Rohani, 2011) conducted tests on multi-cell cross-sections with web and corner optimization. The results show that the web-to-web cross-section (Figure 1-2 (e)) has the highest EA and lowest F_{max}. Additionally, (Rabeta & Sitompul, 2018) adds a circle and ellipse hole to the single wall crash-box to reduce F_{max}. It was found that the elliptical hole has a smaller F_{max} value than the circular hole. However, no studies have been published on the comparison of the best multi-cell of the thin-walled column structure as shown in Figures 1-2 with added holes.

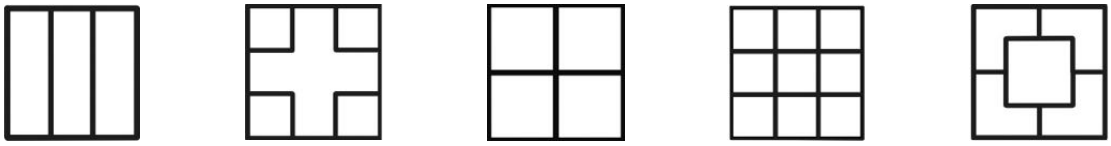

(a) (b) (c) (d) (e)

Figure 1-2: Cross-section configurations of thin-walled column structures, (a) (Chen & Wierzbicki, 2001), (b) (Kim, 2002), (c) (Hou et al., 2008), (d) (Zhang & Cheng, 2007), (e) (Najafi & Rais-Rohani, 2011)

Based on several previous studies, this study performed using the numerical method. For impact research, numerical methods can provide convenience in understanding the deformation mechanism and the response of the energy-absorbing column against an impact load. Numerical methods can reduce the need for prototype manufacturing which tends to be expensive for physical testing and helps in cases of comparisons and differences in designs. Therefore, the novelty of this research was to determine the best multi-cell of the thin-walled structures and ratio of elliptical holes based on crashworthiness indicator parameters.

2. Performance Parameter

Parameters that become indicators to determine the best cross-section based on (Baroutaji et al., 2017) as follows:

- *Peak crushing force,* $\boldsymbol{F_{max}}$

Peak crushing force is the highest force/load required to cause significant deformation. The peak crushing force is measured from the reaction force on the fixed base, which is the same principle as to how load cells are used in physical testing.

- *Energy absorption,* $\boldsymbol{EA}$
  Energy absorption is the energy absorbed by the structure to deform during an impact. The total energy absorbed by the structure is equal to the area under the instantaneous force-displacement curve as formulated as follows:

$$EA = \int_0^{dmax} FdS \tag{2-1}$$

  d_{max} and F is the maximum deformation and instantaneous force. The higher the EA value, the higher the structure's ability to absorb impact energy.

- *Mean crushing force,* $\boldsymbol{F_{mean}}$
  Mean crushing force is the mean force experienced by the structure when it is deformed. Mathematically, F_{mean} can be formulated as follows:

$$F_{mean} = \frac{EA}{d} \tag{2-2}$$

  F_{mean} optimal occurs when the value tends to be equal to the value of F_{max}.

- *Crushing force efficiency,* $\boldsymbol{CFE}$
  Crushing force efficiency is the ratio of F_{mean} and F_{max}. F_{mean} and F_{max} are important parameters to be determined because they are directly related to the decelerations that will be experienced by vehicle passengers. If the ratio approaches unity (value 1), then the F_{mean} a value close to the F_{max} the value thus minimizing the change in decelerations. In other words, if this ratio is far from unity, there is a rapid change in deceleration and this is dangerous when applied to crashworthiness design. In general, the CFE value is closer to one, the better its ability to absorb energy. Mathematically, CFE can be formulated as follows:

$$CFE = \frac{F_{mean}}{F_{max}} \tag{2-3}$$

To determine the best cross-section configuration, a multi-criteria decision making (MCDM) process is used with a complex proportional assessment (COPRAS) method as chosen by (Dehghan-Manshadi et al., 2007), (Chatterjee et al., 2011), and (Huang & Xu, 2019) in their research. This method was chosen because it is relatively easy to use. This method is related to differences in the criteria for the indicator parameters and the weight of each criterion for the indicator parameters. The COPRAS method has successfully solved design selection problems in many fields, such as construction, project management, and economics. This method consists of many steps which are described as follows:

Step 1: Creating the initial matrix (X). This first step involves creating a simple matrix that maps out design concepts for the selection of parameter criteria. This matrix is denoted as X whose writing is given as follows:

$$X = [x_{ij}]_{mXn} = \begin{bmatrix} x_{11} & x_{12} & \cdots & x_{1n} \\ x_{21} & x_{22} & \cdots & x_{2n} \\ \vdots & \vdots & \vdots & \vdots \\ x_{m1} & x_{m2} & \cdots & x_{mn} \end{bmatrix} \tag{2-4}$$
$$(i = 1,2 \cdots m), (j = 1,2 \cdots n)$$

x_{ij} is the value of component i in j component, m the number of design concepts being compared and n is the number of parameters.

Step 2: Determine the relative coefficient of normalization matrix R. The design selection problem is that many design parameters do not have the same dimensions or units. This makes the selection a little more difficult.

One way to solve this problem is to convert the entire matrix X to a non-dimensional matrix R. This makes it is easier to compare and select design concepts based on indicator

parameters. The symbol x_{ij}represents a positive (absolute) value for each parameter and $\sum x_{ij}$ is the sum of the values for one of the design concepts. The purpose of the relative coefficient is to reduce or simplify the parameter values so that they are easier to compare. The relative coefficient symbol is R which is formulated as follows:

$$R = \left[r_{ij}\right]_{mXn} = \frac{x_{ij}}{\sum_{i=1}^{m} x_{ij}} \tag{2-5}$$

Step 3: Determine the weight of each parameter which is described as follows:

Compare the two parameters. Total comparison sets (N) are equal to $N = (n(n-1)/2)$, where n is the number of parameters. In this study, $n = 3$ which represents the parameters F_{max}, EA, and CFE.

Between the two selected parameters, give a score on each criterion of the indicator parameter. For more important parameters, a score of 3 is given, while less important parameters are given a score of 1. In this study, the score $N_{ij} = 3$ for F_{max} and EA, while $N_{ij} = 1$ for CFE.

The total number of scores obtained for each parameter (W_j) is shown in equation (2-6), then calculate the weight of each parameter (w_j) with equation (2-7).

$$W_j = \sum_{i=1}^{m} N_{ij} \tag{2-6}$$

$$w_j = \frac{W_j}{\sum_{j=1}^{n} W_j} \tag{2-7}$$

Step 4: Calculating the normalized weight of matrix D.

$$D = \left[d_{ij}\right] = r_{ij}\ x\ w_j \tag{2-8}$$

d_{ij} is the normalization of the weight value of the component design concept i with the parameter j.

Step 5: Determine and summing the weighted normalized values for the beneficial and non-beneficial parameters, which are shown as follows:

$$S_{+i} = \sum_{i=1}^{n} d_{+ij} \tag{2-9}$$

$$S_{-i} = \sum_{i=1}^{n} d_{-ij} \tag{2-10}$$

d_{+ij} an d_{-ij} are the weighted normalized values for beneficial and non-beneficial elements.

Step 6: Determine relative significance or priority. The design concept priority is calculated based on the relative significance (Q_i). The larger the Q_i value, the greater the priority of the design concept. The design concept with the maximum relative significance value (Q_{max}) is the best choice for concept selection decisions. Relative significance is formulated as follows:

$$Q_i = S_{+i} + \frac{S_{-min} \sum_{i=1}^{m} S_{-i}}{S_{-1} \sum_{i=1}^{m} (S_{-min}/S_{-i})} \tag{2-11}$$

Step 7: Calculate the quantitative utility (U_i) for the design concept. Quantitative utility values are directly related to relative significance. The quantitative utility value determines the rating of the design concept which can be calculated by dividing the priority of each design concept by the maximum value. Mathematically, the quantitative utility can be written as follows:

$$U_i = \frac{Q_i}{Q_{max}} \tag{2-12}$$

The maximum value of relative significance is denoted as Q_{max}.. The quantitative utility value (U_i) 100 is considered to be the best design concept.

3. Methodology

This research is divided into two phases. In the first phase, five columns with different cross-sections were designed. The cross-section differences consisted of three-cell [3S], four square elements [4P], nine-cell [9S], four-cell [4S], and web-to-web [WW] with AA6061-O material (Kumar et al., 2018).

Column length (L) and thickness (t) was kept constant for the five cross-section configurations, namely 180 mm (Jusuf et al., 2015) and 1 mm, respectively. Next, the best cross-section will be selected based on parameter values using the COPRAS method.

The second phase is to further improve the crash performance of the selected cross-sections. Crash performance is improved by adding elliptical holes having different diameter ratios. These results will be compared and selected after going through an assessment process (COPRAS method). The initial impact speed was 3.74 ms^{-1} with an impactor mass of 290 kg (Jusuf et al., 2015). The configuration and dimensions of the column are shown in Figure 3-1 and Table 3-1.

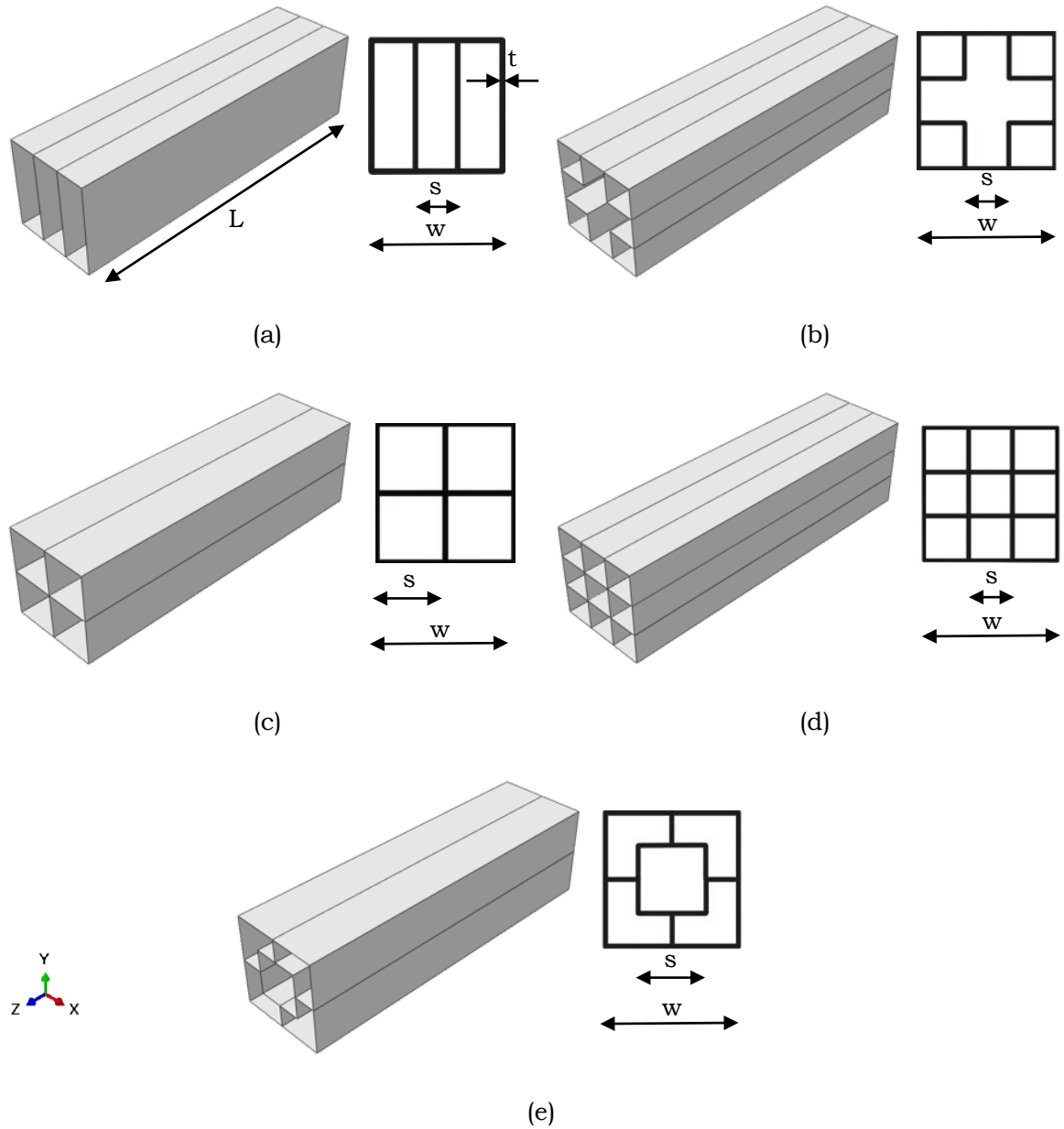

Figure 3-1: Cross-Section Configuration of Thin-Walled Column Structures: (a) Three-Cell, (b) Four Square Elements, (c) Four-Cell, (d) Six-Cell, and (e) Web-to-Web

Table 3-1: Thin-Walled Column Dimensions for Cross-Section Difference

Code		Outer wall width (mm), *w*	Inner wall width (mm), *s*
3S		48	@16
4P			
9S			
4S			@24
WW			

4. Finite Element Modeling

In this study, the finite element model is simulated using Abaqus-explicit. The entire model consists of a thin-walled column structure, impactors, and base as shown in Figure 4-1. The column structure is modeled using a 4 node shell continuum (S4R) element with 5 integration points along the direction of the element thickness. Enhanced hourglass control is used to prevent artificial zero energy deformation mode and integration point is used to prevent volumetric locking.

An element size of 2x2 mm^2 (8640 elements) was selected for the column based on the convergence mesh. The converged mesh was carried out to ensure that the mesh size was sufficient to accurately illustrate the deformation process. The convergence mesh result of the column model is shown in Figure 4-2. The contact algorithm is a "general contact" that is used to avoid column wall interpenetration. However, the computation time to be longer than other algorithms. The friction coefficient is determined to be 0.57 (Jusuf et al., 2015).

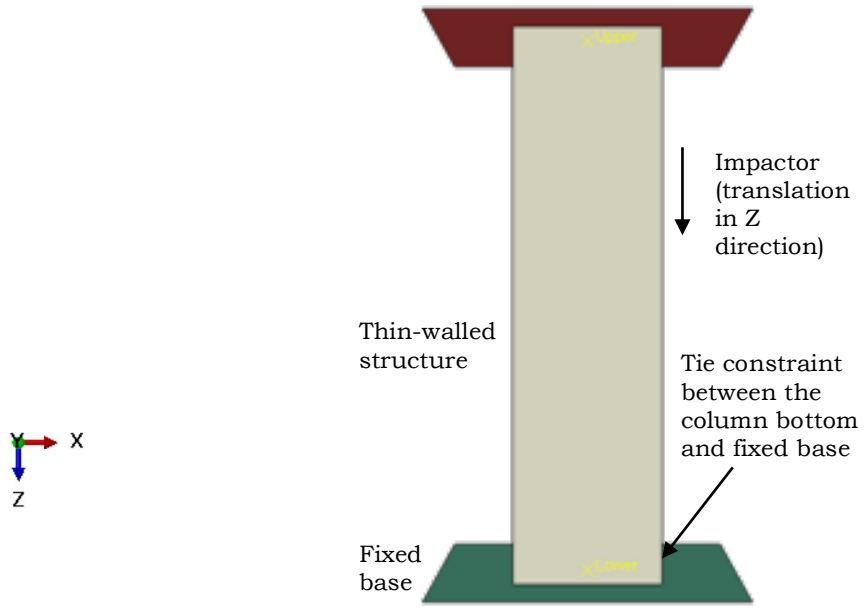

Figure 4-1: Finite Element Analysis Setup

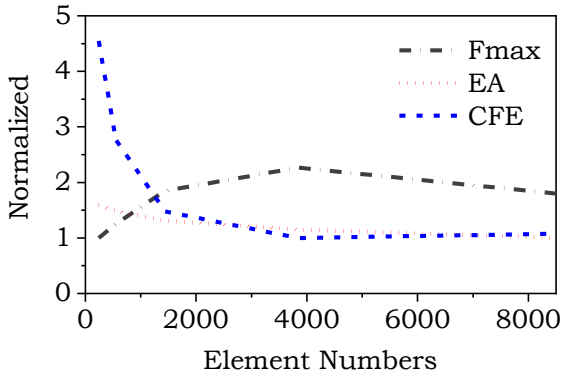

Figure 4-2: Convergence Mesh Study for Thin-Walled Model

The rigid body was employed to model the impactor. Translational displacement of the impactor only one allowable direction or in other words all other translations and rotations degree of freedom were fixed. The impact velocity of 3.74 ms-1 was chosen based on the velocity of the crash test equipment owned by the Bandung Institute of Technology. The mass of the impactor is assumed to be 25% of the mass of the passenger car, which is 1,160 kg, which means that each energy-absorbing column structure is capable of absorbing kinetic energy equivalent to the mass of 290 kg because the maximum energy that can be absorbed by the two-column structures in its application is less than 50% (Witteman, 1999). Aluminum alloy (AA6061-O) was chosen because of its ductile nature so that it is good in energy absorption applications characterized by plastic deformation. The mechanical properties of these materials are shown in Table 4-1.

Table 4-1: Mechanical Properties of AA6061-O (Zhang & Zhang, 2013)

Density ($kg.m^{-3}$)	Elastic Modulus (GPa)	Poisson's Ratio	Yield Strength (MPa)	Ultimate Strength (MPa)	Failure Strain
2.700	68	0,33	71	130,7	0,22

5. Result and Discussion

A summary of the results obtained in this study is presented in Table 5-1. The table also displays the results calculated value using the COPRAS method. The simulation results are only located in the X matrix column, while the normalized decision matrix and weighted normalized decision matrix are results calculated using the COPRAS method. A detailed discussion will be explained in the next subsection.

Table 5-1: The Decision Matrix X, Normalized, and Weighted for Profile Differences

Code		Matrix X			Normalized Matrix			Weighted Matrix		
		F_{max} (kN)	EA (kJ)	CFE	F_{max}	EA	CFE	F_{max}	EA	CFE
3S		25,10	1,77	0,54	0.1376	0.1793	0.1571	0.0574	0.0748	1.0569
4P		40,30	2,03	0,77	0.2210	0.2057	0.2214	0.0921	0.0858	0.7499
4S		31,10	2,01	0,63	0.1705	0.2036	0.1818	0.0711	0.0849	0.9130
9S		48,92	2,03	0,78	0.2682	0.2057	0.2267	0.1118	0.0858	0.7323
WW		36,97	2,03	0,74	0.2027	0.2057	0.2131	0.0845	0.0858	0.7791

5.1 Force vs. Displacement Characteristics of Different Cross-Section

The deformation of the column structure after experiencing the impact force is shown in Figure 5-1. It can be seen that the amount of progressive buckling in each cross-section configuration is different. This is due to the different inertia in each cross-section configuration. In the 3S cross-section, almost the entire column structure experiences

deformation which indicates a potential hazard when applied to the vehicle structure because it is unable to completely absorb the impact energy. The cross-section configuration with the least deformation (progressive buckling) is the 9S cross-section.

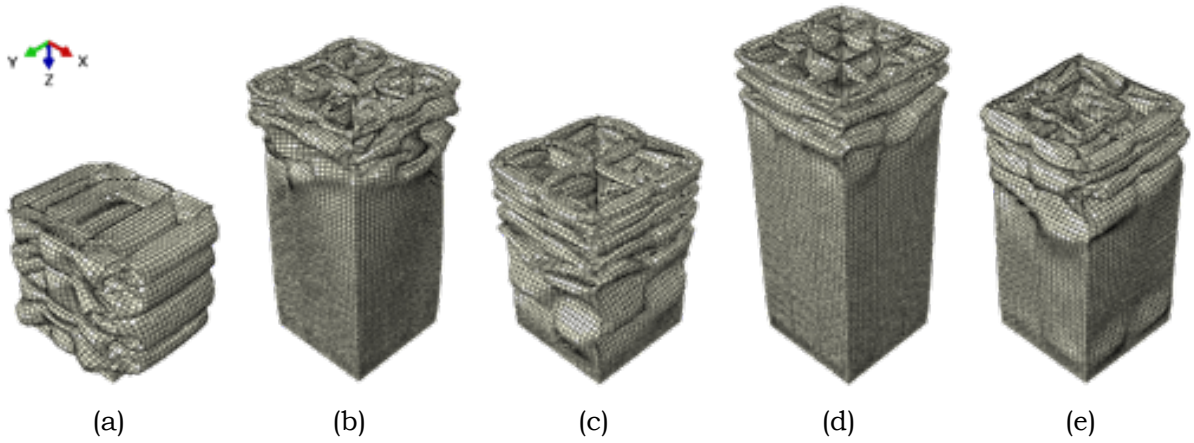

Figure 5-1: Deformation of Thin-Walled Columns After Experiencing Impact Loads for Cross-Section Differences: (a) 3S, (b) 4P, (c) 4S, (d) 9S, dan (e) WW

The instantaneous force to displacement profile for each cross-section is shown in Figure 5-2 (a). The value of the force is obtained from the reference point found on the base component with the description "Lower", while the displacement is obtained from the reference point in the impactor component with the description "Upper" as shown in Figure 4-1. The force on the base component is the reaction force due to the impact of the impactor component with a thin-walled column structure, while the displacement is obtained based on the movement of the impacting component which is in contact with the column structure. Figure 5-2 (b) shows the mean crushing force profile experienced by the column structure. From the two figures, it can be seen that the highest and lowest energy absorption (area under the curve) is found in the 9S and 3S cross-section configurations.

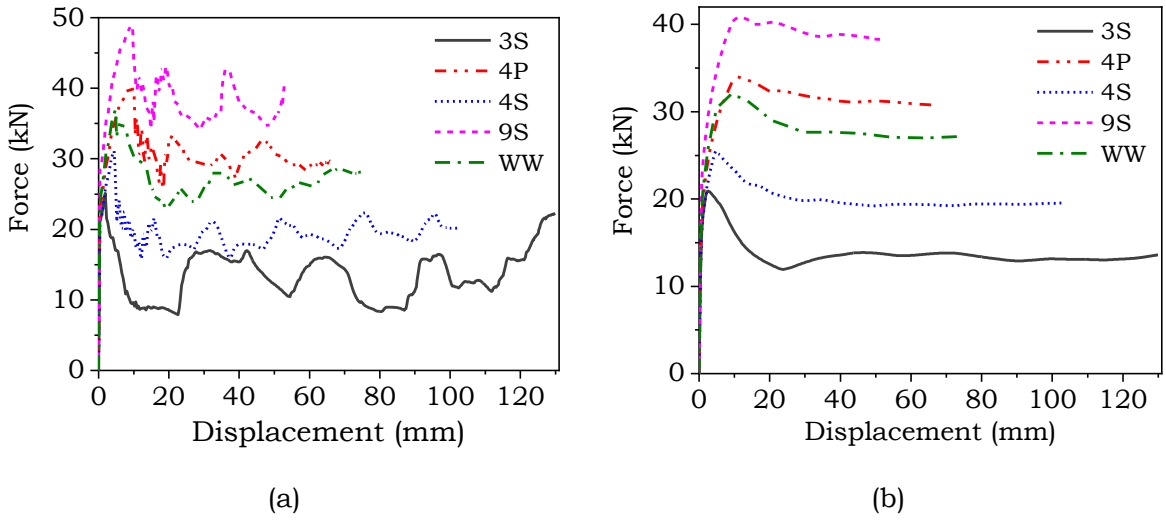

Figure 5-2: (a) Instantaneous Force vs. Displacement and (b) Mean Crushing Force vs. Displacement for Difference of the Cross-Section

5.2 Energy Absorption

In Figure 5-3, the energy absorption is plotted as a function of displacement length rather than as a function of time because to determine the energy absorption at each displacement. It is concluded that the four cross-sections (4P, 4S, 9S, and WW) have

relatively the same energy absorption value, namely, 2.02 kJ, while the three-cell (3S) cross-section has the lowest value, namely 1.80 kJ.

The next process is to choose the best column based on the crashworthiness parameters. This process involves three indicator parameters, namely peak crushing force (F_{max}), energy absorption (EA), and crushing force efficiency (CFE) which will be discussed in the next section.

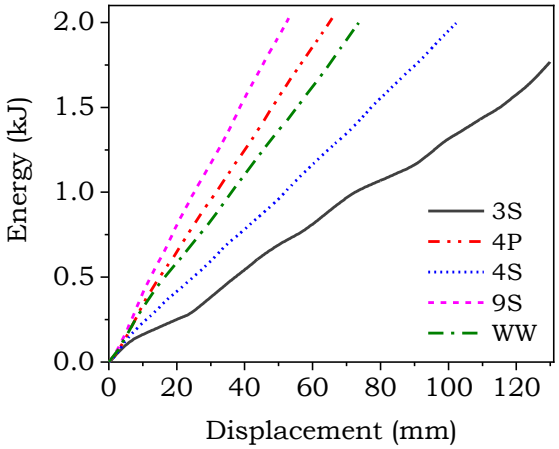

Figure 5-3: Energy Absorption Characteristics of Five Different Cross-Section

5.3 Selection of the Best Cross-Section

To determine the best cross-section, the COPRAS method is used. This method was chosen for the simplification of usability. The indicator parameters used in the cross-section selection are F_{max}, EA, and CFE.

Step 1: determine the X matrix, Step 2: determine the relative coefficient (R)normalized matrix, and Step 3: determine the weight of each indicator parameter. To get the values in step 3, need to adjust the weights from Table 5-1. It can be seen that the highest weight setting is 3 and the lowest is 1. The results of the three initial steps are shown in Table 5-2. Next, step 4 can be carried out: calculating the weighted normalized matrix (D). Step 5: determining the weighted normalized value for beneficial and non-beneficial elements. The beneficial element consists of the parameters F_{max} and EA, while the non-beneficial element is the only CFE. Step 6: determining the relative significance or priority and step 7: calculating the quantitative utility. The values of the four final steps are shown in Table 5-3.

Table 5-2: Weightage Setting for Each Crashworthiness Criteria (Huang & Xu, 2019)

Selection Criteria	**Number of Comparison Sets, $N = (3(3-1)/2 = 3)$**			W_j	w_j
	1	**2**	**3**		
F_{max}	2	3		5	5/12 = 0,417
EA	2		3	5	5/12 = 0,417
CFE		1	1	2	2/12 = 0,166
	Total, Σ			12	1

Table 5-3: Results of the COPRAS Method for Profile Differences

Code		***Beneficial S_{+i}***	***Non-beneficial S_{-i}***	Q_i	U_i	***Rank***
3S		0.1322	1.0569	0.7967	68.8796	5
4P		0.1779	0.7499	1.1146	96.3569	2
4S		0.1560	0.9130	0.9253	79.9927	4
9S		0.1976	0.7323	1.1567	100.0000	1
WW		0.1703	0.7791	1.0718	92.6586	3

Based on Table 5-3, it is found that the column structure with the 9S cross-section has the best results, followed by 4P and WW and the smallest value is 3S. Thus, a column with a cross-section of 9S was selected to investigate the defect effect in the form of an elliptical hole based on the criteria for the crashworthiness parameter.

5.4 Effect of Elliptical Holes

An elliptical hole was used to reduce F_{max} and to encourage progressive buckling in the area around the hole. An elliptical hole is created in the center of the 9S column by a total of four from the side to the side as shown in Figure 5-4 (a).

The elliptical holes are created with the difference in the ratio a/w (0.1; 0.2; 0.3; 0.4) and a constant a/b ratio (2) which details are shown in Table 5-4. As mentioned in the Introduction, elliptical holes are selected based on research (Rabeta & Sitompul, 2018) which states that the elliptical is more effective in reducing F_{max} than the circle shape.

The simulation results of the difference in the ratio of the elliptic hole diameter (a/w) for the instantaneous force to displacement parameter are shown in Figures 5-5 (a), (b), and (c). In each figure, the instantaneous and mean force profiles are displayed as well as an illustration of the thin-walled column structure when it is subjected to impact loads which cause plastic deformation (energy absorption). The stress concentration occurs in the area around the hole marked in red at the initial of the impact causing progressive buckling. Based on Table 5-5, F_{max} decreased from 48.92 kN (without holes) to 40.39 kN (hole ratio 0.3). Energy absorption tends to be constant, at 2.03 kJ. CFE increased from 0.78 for columns without holes to 0.88 for columns with a hole ratio of 0.3.

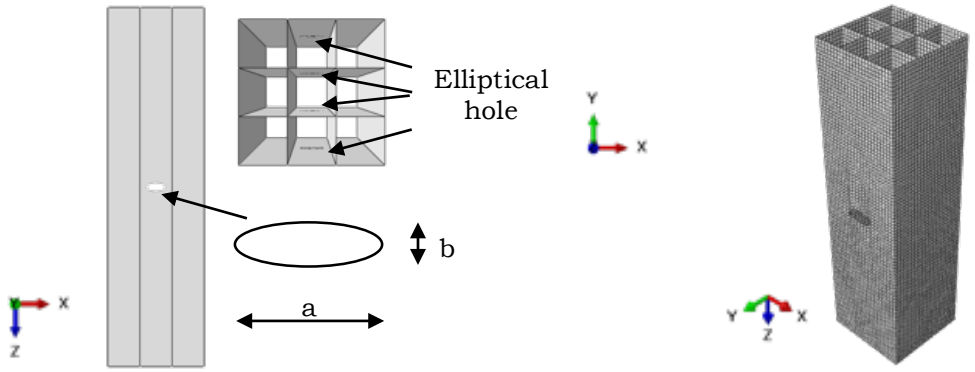

Figure 5-4: Thin-Walled Column Structure with 9S Cross-Section and Elliptical Holes: (a) Geometry dan (b) *Mesh*

Table 5-4: Elliptical Hole Dimensions

a/w	a (mm)	w (mm)	b (mm)
0,1	4,8		2,4
0,2	9,6	48	4,8
0,3	14,4		7,2

As with the previous section (cross-section differences), the COPRAS method was used to determine the best elliptic hole ratio (steps are shown in Tables 5-5 and 5-6). It is found that the column with a hole ratio of 0.3 ranks one of the three models being compared. Ranks two and three are the models with a hole ratio a/w of 0.2 and 0.1, respectively.

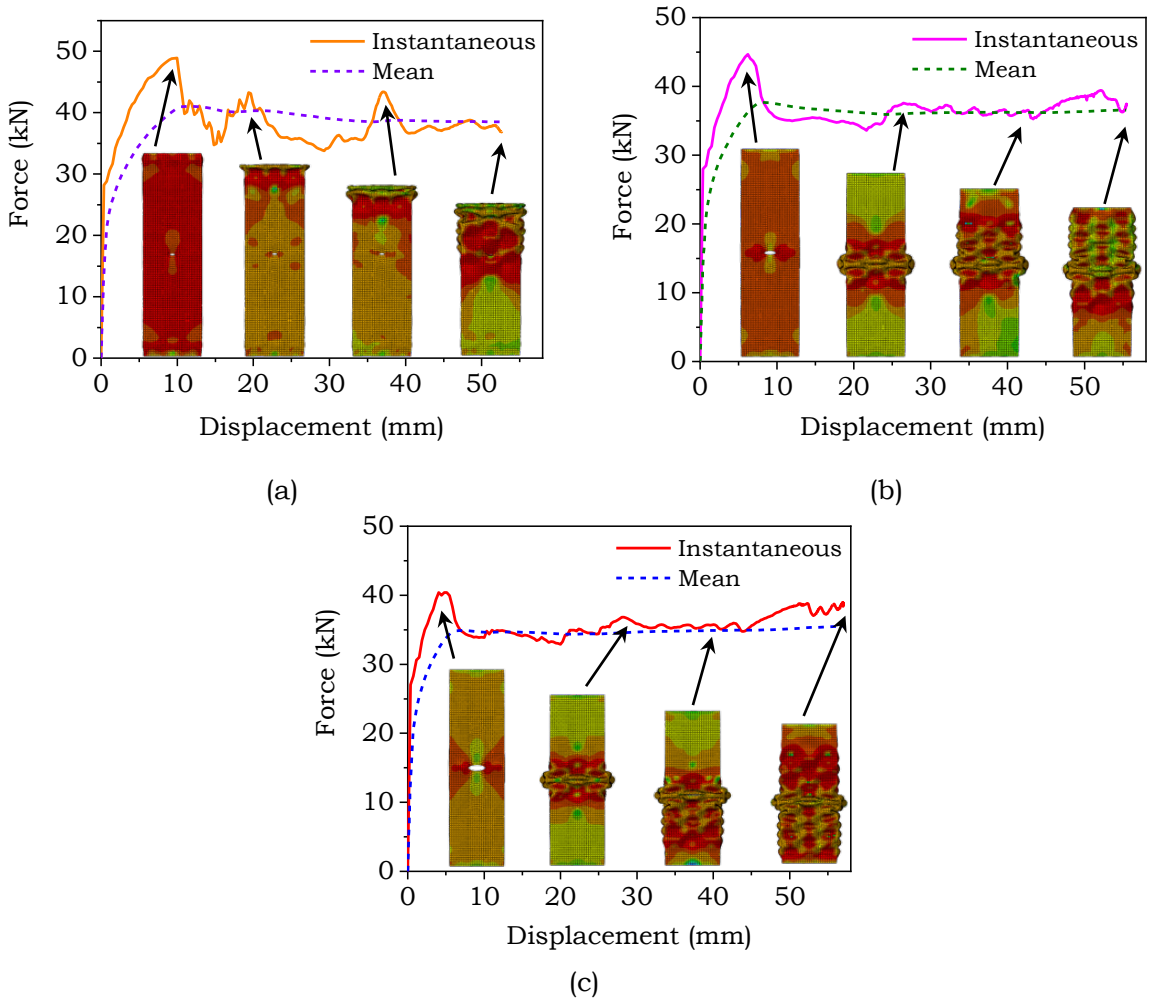

Figure 5-5: Force vs. Displacement Profile in a 9S Cross-Section with a Hole Ratio: (a) 0.1, (b) 0.2, and (c) 0.3

Table 5-5: The Decision Matrix X, Normalized, and Weighted for Hole Ratio Differences

Hole Ratio	Matrix X			Normalized Matrix			Weighted Normalized		
	F_{max} (kN)	EA (kJ)	CFE	F_{max}	EA	CFE	F_{max}	EA	CFE
0,1	48,93	2,03	0,79	0,3652	0,3341	0,3173	0,1523	0,1393	0,5231
0,2	44,65	2,03	0,82	0,3333	0,3334	0,3294	0,1390	0,1390	0,5039
0,3	40,39	2,02	0,88	0,3015	0,3325	0,3532	0,1257	0,1387	0,4699

Table 5-6: Results of the COPRAS Method for Hole Ratio Differences

Hole Ratio	*Beneficial* S_{+i}	*Non-beneficial* S_{-i}	Q_i	U_i	*Rank*
0,1	0,2916	0,5231	0,7667	96,6658	3
0,2	0,2780	0,5039	0,7711	97,2221	2
0,3	0,2644	0,4699	0,7931	100,0000	1

6. Conclusion

Numerical investigations of the axial impact response of thin-walled column structures and ductile metal alloy (AA6061-O) materials with different cross-sections and elliptical hole diameter ratios were carried out. It was found that the nine-cell cross-section (9S) was best for crashworthiness applications based on the parameters F_{max}, EA, and CFE. Also, the addition of an elliptical hole reduces the F_{max} value and increases the

CFE. This is due to the progressive buckling process which is more effective in the area around the hole. Therefore, it is concluded that the nine-cell (9S) cross-section with an elliptical hole ratio of 0.3 shows good potential for crashworthiness applications so that can reduce serious injuries to passengers in the vehicle.

Acknowledgment

This research was supported by Mr. Prio Adhi Setiawan as a Senior Advisor at the German Indonesian Association of Experts and Scholars.

References

Baroutaji, A., Sajjia, M., & Olabi, A. G. (2017). On the Crashworthiness Performance of Thin-Walled Energy absorbers: Recent Advances and Future Developments. *Thin-Walled Structures*, *118*(May), 137–163. https://doi.org/10.1016/j.tws.2017.05.018

BPS-Statistics. (2018). *Land Transportation Statistics 2018. BPS RI*.

Chatterjee, P., Athawale, V. M., & Chakraborty, S. (2011). Materials selection using complex proportional assessment and evaluation of mixed data methods. *Materials and Design*. https://doi.org/10.1016/j.matdes.2010.07.010

Chen, W., & Wierzbicki, T. (2001). Relative merits of single-cell, multi-cell, and foam-filled thin-walled structures in energy absorption. *Thin-Walled Structures*, *39*, 287–306. https://doi.org/10.1016/S0263-8231(01)00006-4

Daehn, G. S. (2014). Sustainable design and manufacture of lightweight vehicle structures. In *Alternative Fuels and Advanced Vehicle Technologies for Improved Environmental Performance: Towards Zero Carbon Transportation*. https://doi.org/10.1533/9780857097422.2.433

Dehghan-Manshadi, B., Mahmudi, H., Abedian, A., & Mahmudi, R. (2007). A novel method for materials selection in mechanical design: Combination of non-linear normalization and a modified digital logic method. *Materials and Design*. https://doi.org/10.1016/j.matdes.2005.06.023

Hou, S., Li, Q., Long, S., Yang, X., & Li, W. (2008). Multiobjective Optimization of Multi-Cell Sections for the Crashworthiness Design. *International Journal of Impact Engineering*, *35*(11), 1355–1367. https://doi.org/10.1016/j.ijimpeng.2007.09.003

Huang, H., & Xu, S. (2019). Crashworthiness Analysis and Bionic Design of Multi-Cell Tubes Under Axial and Oblique Impact Loads. *Thin-Walled Structures*, *144*. https://doi.org/10.1016/j.tws.2019.106333

Jusuf, A., Dirgantara, T., Gunawan, L., & Putra, I. S. (2015). Crashworthiness analysis of multi-cell prismatic structures. *International Journal of Impact Engineering*. https://doi.org/10.1016/j.ijimpeng.2014.11.011

Kim, H. S. (2002). New Extruded Multi-Cell Aluminum Profile for Maximum Crash Energy Absorption and Weight Efficiency. *Thin-Walled Structures*, *40*(4), 311–327. https://doi.org/10.1016/S0263-8231(01)00069-6

Kumar, A. P., Mohamed, M. N., Jusuf, A., Dirgantara, T., & Gunawan, L. (2018). Axial Crash Performance of Press-Formed Open and End-Capped Cylindrical Tubes – A Comparative Analysis. *Thin-Walled Structures*, *124*, 468–488. https://doi.org/10.1016/j.tws.2017.12.037

Najafi, A., & Rais-Rohani, M. (2011). Mechanics of Axial Plastic Collapse in Multi-Cell, Multi-Corner Crush Tubes. *Thin-Walled Structures*, *49*(1), 1–12. https://doi.org/10.1016/j.tws.2010.07.002

Rabeta, B., & Sitompul, S. A. (2018). Analysis Numerical Discontinuity of Thin-Walled Tube Subjected Low-Velocity Impact. *SENATIK 2018*, *4*(Prosiding Seminar Nasional Teknologi Informasi dan Kedirgantaraan). https://doi.org/10.28989/senatik.v4i0.144

Sun, G., Tian, X., Fang, J., Xu, F., Li, G., & Huang, X. (2015). Dynamical bending analysis and optimization design for functionally graded thickness (FGT) tube. *International Journal of Impact Engineering*, *78*, 128–137. https://doi.org/10.1016/j.ijimpeng.2014.12.007

Tarlochan, F., Samer, F., Hamouda, A. M. S., Ramesh, S., & Khalid, K. (2013). Design of thin-wall structures for energy absorption applications: Enhancement of

crashworthiness due to axial and oblique impact forces. *Thin-Walled Structures*, *71*, 7–17. https://doi.org/10.1016/j.tws.2013.04.003

Witteman, W. J. (1999). *Improved Vehicle Crashworthiness Design by Control of the Energy Absorption for Different Collision Situations* (Issue 1999). https://doi.org/10.6100/IR518429

Zhang, X., & Cheng, G. (2007). A Comparative Study of Energy Absorption Characteristics of Foam-Filled and Multi-Cell Square Columns. *International Journal of Impact Engineering*, *34*(11), 1739–1752. https://doi.org/10.1016/j.ijimpeng.2006.10.007

Zhang, X., & Zhang, H. (2013). Energy Absorption of Multi-Cell Stub Columns Under Axial Compression. *Thin-Walled Structures*, *68*, 156–163. https://doi.org/10.1016/j.tws.2013.03.014

Investigation of Wire Diameter of Helical Compression Spring for Payload Separation

Shandi Prio Laksono

Rocket Technology Center, National Institute of Aeronautics and Space (LAPAN), Indonesia

e-mail: shandi.prio@lapan.go.id

Received: 26-11-2020. Accepted: 07-04-2021. Published: 30-06-2021

Abstract

The payload is designed to be separated from the rocket at certain altitude. One of the critical component in the payload separation system is the helical compression spring. The helical compression spring ensures safe release of the payload. The spring must satisfy some parameters such as static failure and buckling, also spring has enough energy storing to release the payload during launch. The objective of this paper is to do investigation of wire diameter of helical compression spring which can be used in the payload separation system of sounding rocket based on several constraints. The results obtained show that with payload weight of 60 kg, minimum wire diameter should be 8 mm with mean coil diameter of 80 mm. The maximum separation velocity of 1.76 m/s was obtained by using wire diameter of 8 mm and mean coil diameter of 96 mm.

Keywords: *payload; spring; separation, diameter, rocket.*

Nomenclature

d	=	wire diameter, mm
D_o	=	outside diameter, mm
D_i	=	inside diameter, mm
D	=	mean coil diameter, mm
L_f	=	free length, m
L_s	=	solid length, m
k	=	spring rate, N/m
δ	=	deflection, m
G	=	shear modulus of the material, GPa
N_a	=	number of active coils

1. Introduction

Space launch vehicle and sounding rocket are used to place a satellite into orbit or payload in the upper atmosphere to gather scientific data. The Launch vehicle or sounding rocket places a satellite or payload into orbit or upper atmosphere by using a separation system to release it.

The separation system is a critical point for launching a satellite or payload (Hu et al., 2008). A reliable separation system ensuring the separation is free of collision and minimizing disturbance to the payload or satellite (Li et al., 2014). The launch failures of Atlas Centaur in 1970 and Chinese Long March in 1992. Also, improper in release of Titan's satellite in 1990, Pegasus in 1991 and Delta-2 in 1995 are examples of the failure of separation system (Samani, M., & Pourtakdoust, 2014).

As shown in the figure 1-1, the payload is placed in the forward end of the rocket or launch vehicle. The nose cone or fairing section is commonly used to protect the payload from aerodynamics force (Liu, Y., Li, Z., Sun, Q., Fan, X., & Wang, 2012). The payload is separated from the rocket at an altitude over 100 km (Hu et al., 2008).

ISAS (The Institute of Space and Astronautical Science) of JAXA (Japan Aerospace Exploration Agency) is operating three kinds of the sounding rockets which are S-310, S-520, and SS-520. The smallest rocket, S-310 is able to reach up to 200 km with a maximum payload weight of 50 kg (Abe et al., 2009). The SS-520 sounding rocket has a capability for launching a payload weight of 140 kg to an altitude of 800 km (Inatani, Y., Ishii, N., Nonaka, S., & Abe, 2016).

Separation system has two main functions. The first is to rigidly hold payload or satellite and rocket or launch vehicle together. The second is to influence separation of payload or satellite upon command from rocket or launch vehicle (Tayefi & Ebrahimi, 2009). Separation systems typically consist of the helical compression spring (Hu, X., Chen, X., Tuo, Z., & Zhang, 2012). The spring with length of 180 mm was capable for separating Cubesat of 1 kg at the separation velocity of 1.8 m/s (Kolawole et al., 2018).

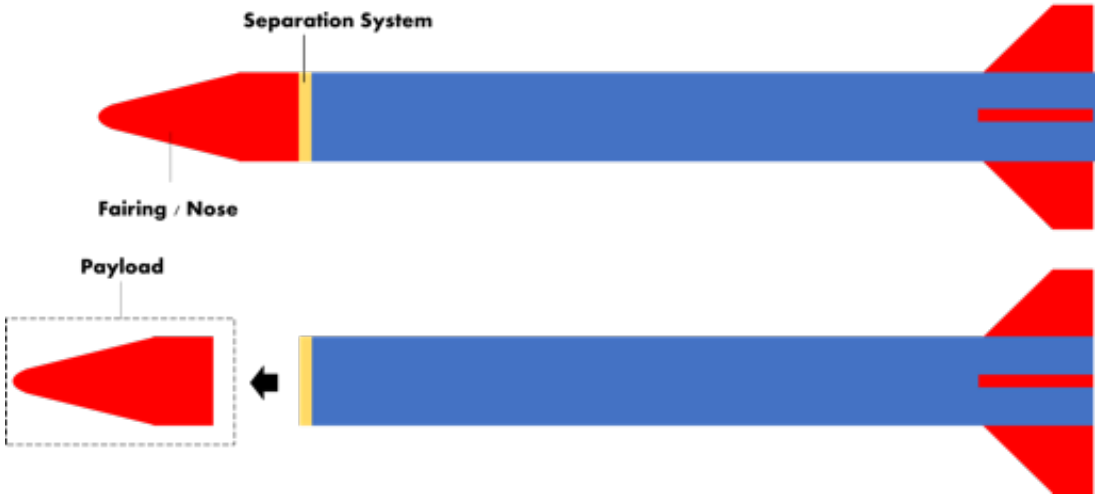

Figure 1-1: Payload Separation

2. Methodology

The objective of this research is to do investigation of wire diameter of helical compression spring which can be used for payload separation system based on several constraints. In the separation system, as shown in the figure 2-1 helical compression spring is subjected to axial load due to payload weight and deflected to its solid length. When the payload needs to be separated during flight, the release mechanism decouples the payload from the rocket and spring exert force to the payload. The spring needs to be able to withstand the payload weight without any failure.

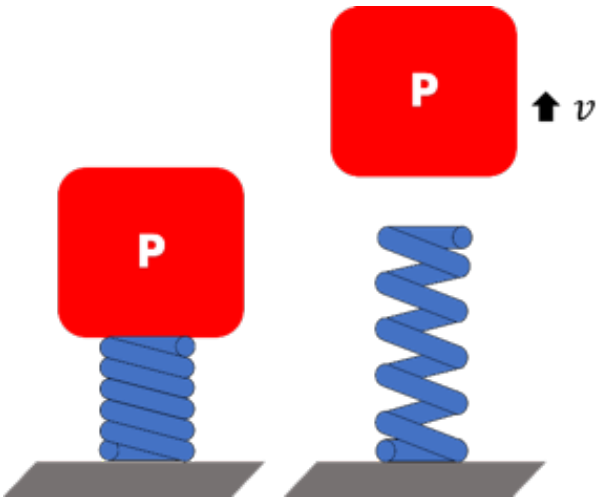

Figure 2-1: Payload and Spring.

2.1. Helical Compression Spring

A Helical compression spring is a spring with an open-coil configuration that resistance to compressive force. They have capability for energy absorption and easy to use. They usually used in machinery or equipment for controlling vibration, reducing forces due to shock loading, applying forces to members, and storing energy (Sawanobori, T., Akiyama, Y., Tsukaharat, T., & Nakamura, 1985).

A Helical compression spring is typically made from round wire, wrapped into a straight-cylindrical shape with a constant pitch between adjacent coils. Square or rectangular wire may also be used. Without an applied load, the spring's length is called the free length. When a compression force is applied, the coils are become more closely together until touch each other, at that time the length the minimum possible is called the solid length (Pattar, S., Sanjay, S.J., & Math, 2014). Figure 2-2 shows a dimensional parameter of round-wire helical compression spring.

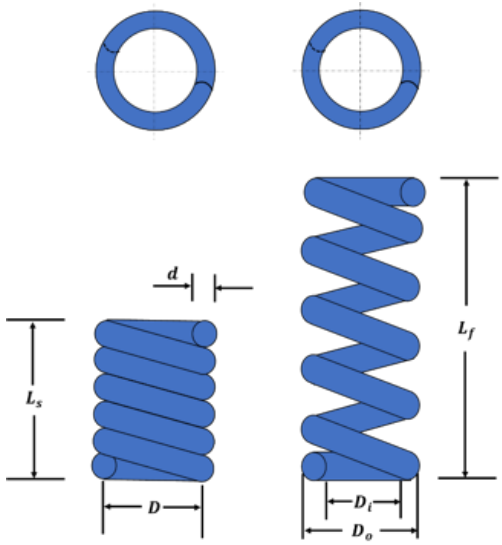

Figure 2-2: Dimensional Parameter of Helical Compression Spring.

Manufacturing of helical springs need determination of the spring parameters such as the mean coil diameter D, wire diameter d and spring index C. Other parameters such as the total number of coils N_a, free length L_f, also important design parameters to be considered (Kolawole et al., 2018). Spring index is the ratio of the mean diameter of the coil to the diameter of the wire as expressed by equation below:

$$C = \frac{D}{d} \tag{2-1}$$

Spring rate (stiffness) is the load required per unit deflection of the spring as expressed by equation below:

$$k = \frac{F}{\delta} = \frac{d^4 G}{8\, D^3 N_a} \tag{2-2}$$

$$\delta = \frac{8FD^3 N_a}{d^4 G} \tag{2-3}$$

2.2. Stress in Helical Compression Spring

The major stresses produced in helical springs are shear stresses due to twisting (Chary & Reddy, 2016). As shown in the figure 2-3, round-wire helical compression spring, loaded by the axial force.

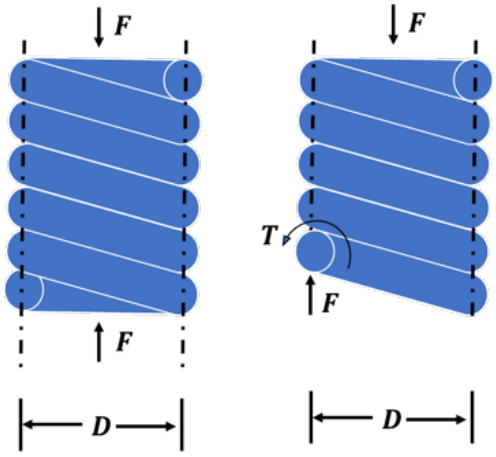

Figure 2-3: Free Body Diagram of Helical Compression Spring Axially Loaded.

The maximum stress in the wire may be calculated by superposition of the torsional shear stress $\tau_1$and direct shear stress τ_2 given by the equation below.

$$\tau_{max} = \tau_1 + \tau_2 \tag{2-4}$$

the torsional shear stress in a bar subjected to a twisting moment T is given by the equation below:

$$\tau_1 = \frac{Tr}{J} \tag{2-5}$$

where

$$J = \frac{\pi d^4}{32} \tag{2-6}$$

and

$$r = \frac{d}{2} \tag{2-7}$$

by substituting equation$(2-6)$ and $(2-7)$ into $(2-5)$, we obtain:

$$\tau_1 = \frac{8FD}{\pi d^3} \tag{2-8}$$

direct shear stress is given by the equation below:

$$\tau_2 = \frac{F}{A} \tag{2-9}$$

where

$$A = \frac{\pi d^2}{4} \tag{2-10}$$

substituting equation $(2-10)$ into $(2-9)$, we obtain:

$$\tau_2 = \frac{4F}{\pi d^2} \tag{2-11}$$

substituting equation $(2-8)$ and $(2-11)$ into $(2-4)$, we obtain:

$$\tau_{max} = \frac{8FD}{\pi d^3} + \frac{4F}{\pi d^2} \tag{2-12}$$

substituting equation$(2-1)$ into $(2-12)$, we obtain:

$$\tau_{max} = \frac{8FD}{\pi d^3}\left(1 + \frac{0.5}{C}\right) \tag{2-13}$$

then the maximum shear stress is given by the equation below:

$$\tau_{max} = K_s \frac{8FD}{\pi d^3} \tag{2-14}$$

where K_s a shear-stress correction factor and is defined by the equation below:

$$K_s = 1 + \frac{0.5}{C} \tag{2-15}$$

The ultimate tensile strength is given by the equation below:

$$S_{ut} \cong Ad^b \tag{2-16}$$

where

$$A = 1753{,}3\ MPa$$

$$b = -0.182$$

The yield shear strength is given by the equation below:

$$S_{sy} = 0.577\ (0.75)\ S_{ut} \tag{2-17}$$

2.3. Buckling in Helical Compression Spring

Buckling of steel helical compression spring with steel material and squared and ground ends is given by the equation below:

$$L_f < 2.63 \frac{D}{\alpha} \tag{2-18}$$

where α is a constant related to end condition and α values for end conditions can be seen in the table 2-1.

Table 2-1: End Condition Constants (Budynas, R.G., Nisbett, J.K, & Shigley, 2008)

End Condition	α
Spring supported between flat parallel surfaces (fixed ends)	0.5
One end supported by flat surface perpendicular to spring axis (fixed); other end pivoted (hinged)	0.707
Both ends pivoted (hinged)	1
One end clamped; other end free	2

MATLAB software was used to calculate some parameters such as maximum shear stress, yield shear strength, spring rate, deflection, free length, energy storing, and separation velocity. Calculation of the helical compression spring parameters are constrained by the following conditions:

- Payload weight: 60 kg
- Number of springs used: 1
- Cross-section of wire: round
- Solid length of spring: 200 mm
- Material of spring: Hard drawn-wire (ASTM A227)
- Shear modulus of spring: 80 GPa
- Mean Diameter of Coil: 80 ≤ D ≤ 100 mm
- Type of ends: squared and grounds

Figure 2-4 shows the flowchart of this research.

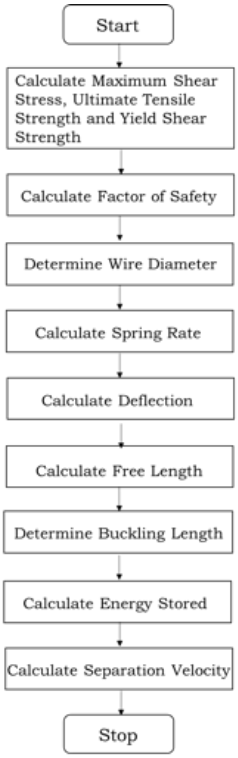

Figure 2-4: Flowchart of research

3. Result and Analysis

Figure 3-1 shows the relationship between wire diameter and maximum shear stress with mean coil diameter of 80, 90, and 100 mm. As shown in the figure, shear stress decreased with increase in wire diameter. The combination between wire diameter of 5 mm with mean coil diameter of 80, 90 and 100 mm resulted in maximum shear stress of 1,008 MPa, 1,131 MPa and 1,253 MPa, respectively. Meanwhile, the ultimate tensile strength and yield shear strength of wire diameter of 5 mm were 1,313 and 568.3 MPa, respectively. In addition, the combination between wire diameter of 10 mm with mean coil diameter of 80, 90 and 100 mm resulted in maximum shear stress of 129.9 MPa, 145.1 MPa and 160.4 MPa, respectively. Meanwhile, the ultimate tensile strength and yield shear strength of wire diameter of 10 mm were 1,151 MPa and 498.2 MPa, respectively.

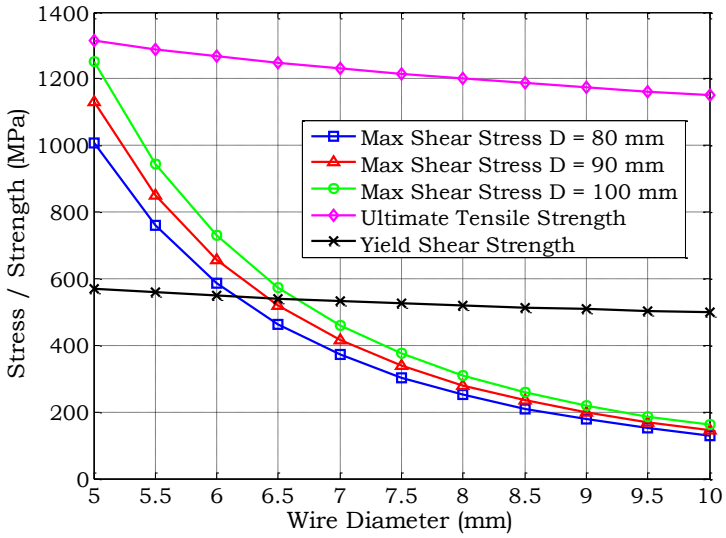

Figure 3-1: Wire Diameter vs Maximum Shear Stress.

Figure 3-2 shows the relationship between wire diameter and safety factor. As shown in the figure, safety factor increased with increase in wire diameter. Also, smaller mean coil diameter has higher safety factor. The wire diameter of 7 mm in all range of mean coil diameter 80, 90 and 100 mm has safety factor higher than 1. It means that yield shear strength of wire diameter of 7 mm is higher than its maximum shear stress. Based on these results, we considered wire diameter of 7 mm, 8 mm and 9 mm as diameter which examined to be used in payload separation system.

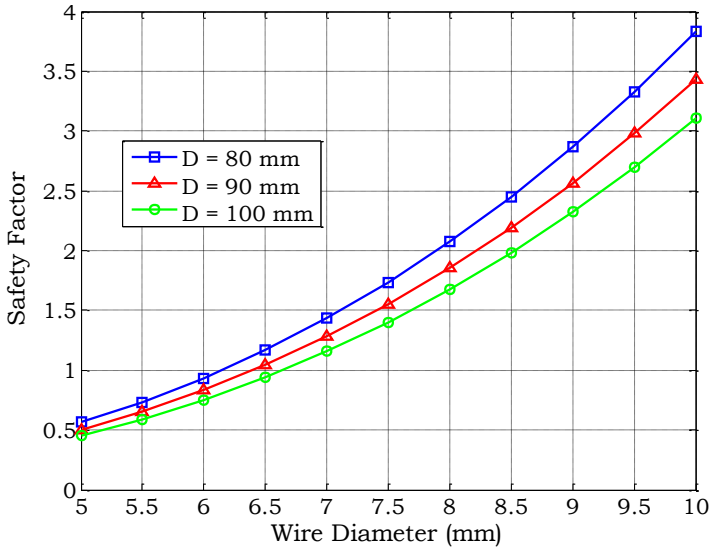

Figure 3-2: Wire Diameter vs Safety Factor.

Figure 3-3 shows the relationship between mean coil diameter and spring rate. As shown in the figure, spring rate decreased with increase in mean coil diameter. The combination between wire diameter of 7 mm with mean coil diameter of 80 and 100 mm, resulted in spring rate of 1,737 N/m and 889.3 N/m, respectively. Meanwhile, the combination between wire diameter of 8 mm with mean coil diameter of 80 and 100 mm, resulted in the spring rate of 3,478 N/m and 1,781 N/m, respectively. In addition, the combination between wire diameter of 9 mm with mean coil diameter of 80 and 100 mm, resulted in spring rate of 6,407 N/m and 3,281 N/m, respectively.

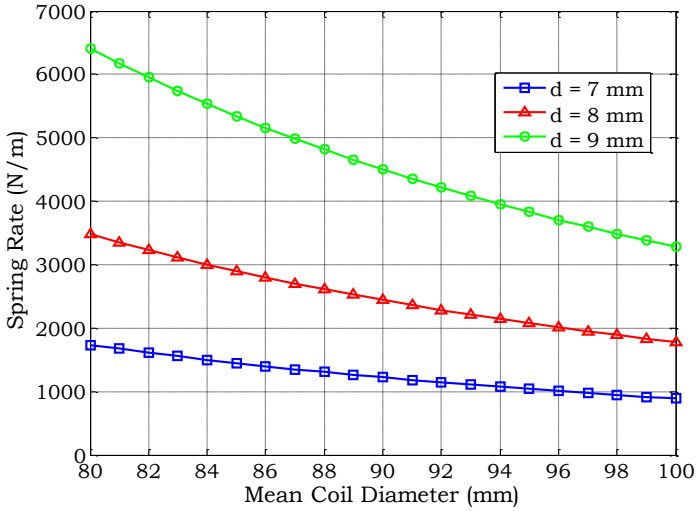

Figure 3-3: Mean Coil Diameter vs Spring Rate.

Figure 3-4 shows the relationship between mean coil diameter and deflection. As shown in the figure, deflection increased with increase in mean coil diameter. The deflection of 0.346 m was obtained by using wire diameter of 7 mm and mean coil diameter of 80 mm. Meanwhile, the combination between wire diameter of 8 mm and 9 mm with mean coil diameter of 80 mm, resulted in deflection of 0.173 m and 0.094 m, respectively.

In addition, the deflection of 0.675 m was obtained by using wire diameter of 7 mm and mean coil diameter of 100 mm. Meanwhile, the combination between wire diameter of 8 mm and 9 mm with mean coil diameter of 100 mm, resulted in deflection of 0.337 m and 0.183 m, respectively.

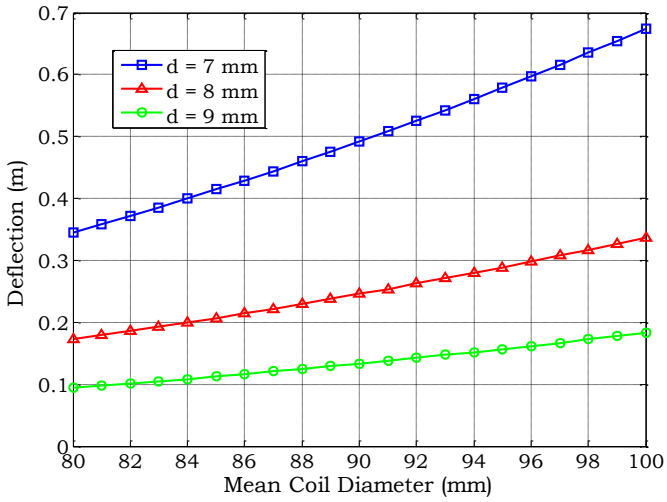

Figure 3-4: Mean Coil Diameter vs Deflection.

Figure 3-5 shows the relationship between mean coil diameter and free length. As shown in the figure, free length increased with increase in mean coil diameter. The free length of 0.546 m was obtained by using wire diameter of 7 mm and mean coil diameter of 80 mm. Meanwhile, the combination between wire diameter of 8 mm and 9 mm with mean coil diameter of 80 mm resulted in free length of 0.373 m and 0.294 m, respectively. The buckling criteria suggested that the free length shouldn't more than 0.42 m. So, the combination between wire diameter of 7 mm with coil diameter of 80 mm wasn't satisfied buckling criteria. Meanwhile, the combination between wire diameter of 8 mm and 9 mm with mean coil diameter of 80 mm were satisfied the buckling criteria. In addition, the free length of 0.875 m was obtained by using wire diameter of 7 mm and mean coil diameter of 100 mm. Meanwhile, the combination between wire diameter of 8 mm and 9 mm with mean coil diameter of 100 mm resulted in free length of 0.537 m and 0.383 m, respectively. The buckling criteria suggested that the free length shouldn't more than 0.526 m. So, the combination between wire diameter of 7 and 8 mm with coil diameter of 100 mm weren't satisfied the buckling criteria. Wire diameter of 7 mm wasn't satisfied the buckling criteria in the all range of mean coil diameter from 80 mm to 100. Meanwhile, wire diameter of 8 mm satisfied the buckling criteria only until mean coil diameter of 96 mm. The wire diameter of 9 mm satisfied the buckling criteria in the all range of mean coil diameter.

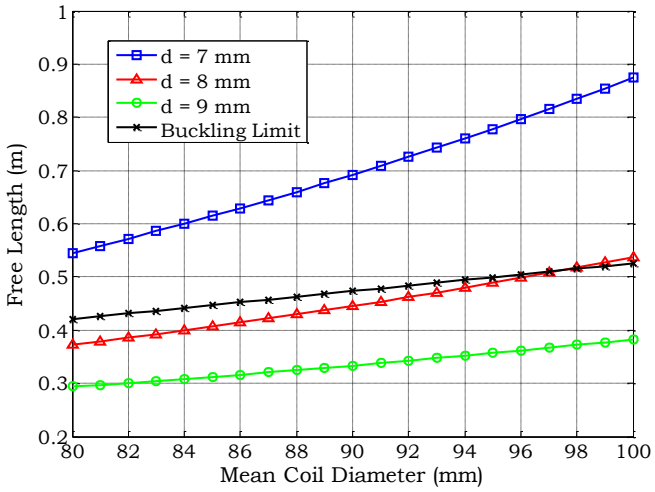

Figure 3-5: Mean Coil Diameter vs Free Length.

Figure 3-6 shows the relationship between mean coil diameter and energy storing. As shown in the figure, energy strong increased with increase in mean coil diameter. The energy storing of 103.6 N.m was obtained by using wire diameter of 7 mm and mean coil diameter of 80 mm. Meanwhile, the combination between wire diameter of 8 mm and 9 mm with mean coil diameter of 80 mm resulted in energy storing of 51.75 N.m and 28.09 N.m, respectively. In addition, energy storing of 202.4 N.m was obtained by using wire diameter of 7 mm and mean coil diameter of 100 mm. Meanwhile, the combination between wire diameter of 8 mm and 9 mm with mean coil diameter of 100 mm resulted in energy storing of 101.1 N.m and 54.87 N.m, respectively.

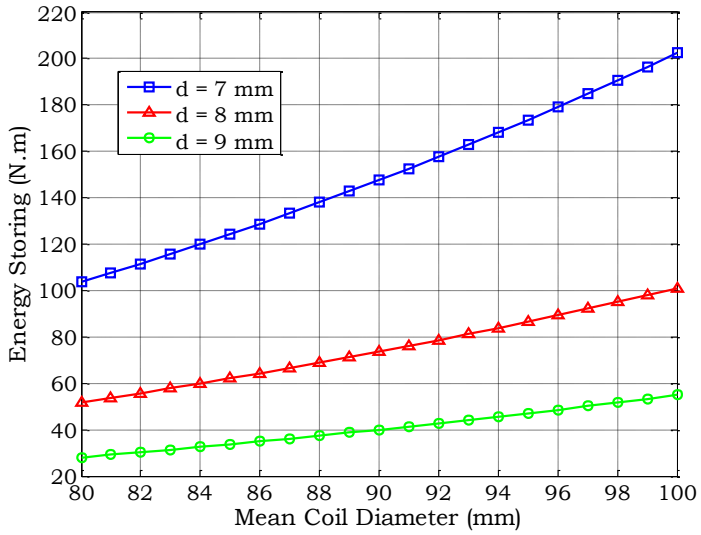

Figure 3-6: Mean Coil Diameter vs Energy Storing.

Figure 3-7 shows the relationship between mean coil diameter and separation velocity. The separation velocity of 1.86 m/s was obtained by using wire diameter of 7 mm and mean coil diameter of 80 mm. Meanwhile, the combination between wire diameter of 8 mm and 9 mm with mean coil diameter of 80 mm resulted in separation velocity of 1.31 m/s and 0.97 m/s, respectively. In addition, the separation velocity of 2.6 m/s was obtained by using wire diameter of 7 mm and mean coil diameter of 100 mm. Meanwhile, the combination between wire diameter of 8 mm and 9 mm with mean coil diameter of 100 mm resulted in separation velocity of 1.84 m/s and 1.35 m/s, respectively. Even, wire diameter of 7 mm, resulted the highest separation velocity, this wire diameter shouldn't be used due to buckling problem which may be occurred.

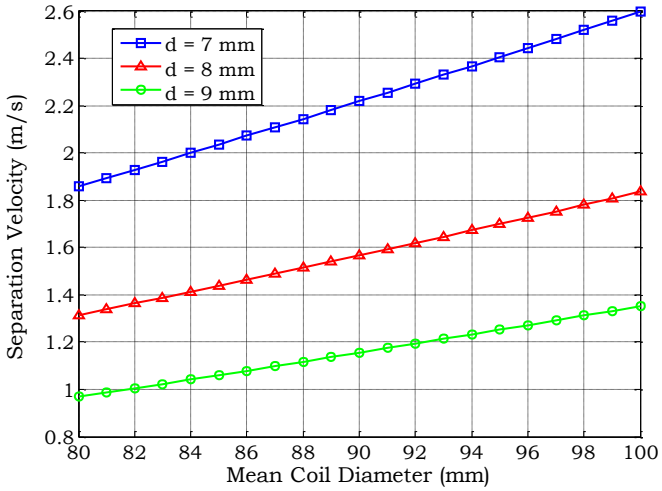

Figure 3-7: Mean Coil Diameter vs Separation Velocity.

4. Conclusions

Investigation of wire diameter of helical compression spring for payload separation has been conducted. The obtained result show that with payload weight of 60 kg, the minimum wire diameter should be 8 mm with mean coil diameter of 80 mm. In order to avoid buckling problem, for wire diameter of 8 mm, the maximum mean coil diameter which can be used was 96 mm. Wire diameter of 9 mm was free from buckling problem in the range of mean coil diameter of 80 – 100 mm. The maximum separation velocity of 1.76 m/s was obtained by using wire diameter of 8 mm and mean coil diameter of 96 mm.

Acknowledgements

Author wishes to thanks to Bambang Sapto Wibowo and Arief Budi Sanjaya for discussion about separation system. Authors also thanks to LAPAN for the support in publishing this research.

References

Abe, T., Nakamura, M., Ishii, N., & Inatani, Y. (2009). Recent Activities and Future Direction of Japanese Sounding Rocket Experiments for Scientific Purpose. *Proc. 19th ESA Symposium on European Rocket and Balloon Programmes and Related Research*, *2009*(September).

Budynas, R.G., Nisbett, J.K, & Shigley, J. E. (2008). *Shigley's Mechanical Engineering Design 8th Edition* (8th ed.). McGraw-Hill.

Chary, C. K., & Reddy, S. (2016). Design and Analysis of Helical Compression Spring of IC Engine. *International Advanced Research Journal in Science, Engineering and Technology*, *3*(10), 153–158. https://doi.org/10.17148/IARJSET.2016.31029

Hu, X., Chen, X., Tuo, Z., & Zhang, Q. (2012). Dynamics and transient perturbation analysis of satellite separation systems. *Proceedings of the Institution of Mechanical Engineers, Part G: Journal of Aerospace Engineering*, *227*(12), 1968–1976. https://doi.org/10.1177/0954410012466780

Hu, H., Wang, J., & Lu, W. (2008). Simulation and analysis of fairing jettison from sounding rocket. *Journal of Aeronautics, Astronautics and Aviation*, *40 A*(4), 237–244.

Inatani, Y., Ishii, N., Nonaka, S., & Abe, T. (2016). Recent Activities and Future Direction of Japanese Sounding Rocket Experiments for Scientific Purpose. *International Seminar on Aerospace Science and Technology IV*, 144–152.

Kolawole, S. O., Adewale, H., & Christian, O. (2018). Optimal Helical Spring Design for a P-Pod Using Chaotic Backtrack Search Algorithm. *International Journal of Scientific & Engineering Research*, *9*(8), 71–76. http://www.ijser.org

Li, J., Yan, S., & Tan, X. (2014). Dynamic-envelope analysis of clamp-band joint considering pyroshock of satellite separation. *Journal of Spacecraft and Rockets*, *51*(5), 1390–1400. https://doi.org/10.2514/1.A32382

Liu, Y., Li, Z., Sun, Q., Fan, X., & Wang, W. (2012). Separation dynamics of large-scale fairing section A fluid-structure interaction study.pdf. *Proceedings of the Institution of Mechanic Al Engineers Part G Journal of Aerospace Engineering*. https://doi.org/10.1177/0954410012462317

Pattar, S., Sanjay, S.J., & Math, V. . (2014). Static Analysis of Helical Compression Spring. *International Journal of Research in Engineering and Technology*, *03*(15), 835–838. https://doi.org/10.15623/ijret.2014.0315158

Samani, M., & Pourtakdoust, S. H. (2014). Analysis of Two - Stage Endo - Atmospheric Separation Using Statistical Methods. *Journal of Theoretical and Applied Mechanics*, *1992*, 1115–1124.

Sawanobori, T., Akiyama, Y., Tsukaharat, T., & Nakamura, M. (1985). Analysis of Static and Dynamic Stresses in Helical Spring. *Bulletin of Japan Society of Mechanical Engineers*, *28*, 725–734.

Tayefi, M., & Ebrahimi, M. (2009). Design and analysis of separation systems based on an optimization approach. *47th AIAA Aerospace Sciences Meeting Including the New Horizons Forum and Aerospace Exposition*, *January*, 1–10. https://doi.org/10.2514/6.2009-436

Properties Comparison of Open Hole and Non-Hole Carbon UD-Lycal Composite with Vacuum Bagging Manufacturing Method

Lathifa Rusita Isna[1], Afid Nugroho[1], Rezky Agung P [1], Redha Akbar R[1]

[1]Aeronautic Technology Center, National Institute of Aeronautics and Space (LAPAN), Indonesia

e-mail: lathifa.rusita@gmail.com

Received: 02-12-2020. Accepted: 22-04-2021. Published: 30-06-2021

Abstract

Carbon fiber reinforced polymer is one of some composite materials that have high strength with lightweight material. To apply this composite to the amphibious airplane structure, it should through the experimental tensile test to know the tensile strength and modulus of elasticity of the composite. In this experiment, we use Carbon UD fiber and Lycal resin as the composite material manufactured with Vacuum Bagging Method. Specimens and testing process refer to ASTM D3039 for non-hole specimen and ASTM D5766 for the open-hole specimen of a tensile test standard for composite matrix polymers. The result of the experimental test shows that the tensile modulus of elasticity for non-hole composite is 34.92 ± 0.13 GPa, with the Ultimate Tensile Strength of this composite is 1081± 0.03 MPa, and the modulus of elasticity for open-hole composite is 41.87± 0.02 GPa, with the Ultimate Tensile Strength of this composite is 899.04± 0.02 MPa. The simulation yields nearly the same stress-strain graph as the result of an experiment. The result shows that the open hole composite has the ultimate tensile strength lower than non-hole composite, it's due to when the open hole composite tested with the tensile force, the stress will be concentrated in the hole area which becomes a trigger failure that may decrease the tensile strength value.

Keywords: *composite, carbon fiber, vacuum bagging, tensile testing, hole specimen.*

1. Introduction

Composite is the material that mostly uses for airplane structure. The composite development has increased significantly year by year. The advantages of composite material for the airplane structure are due to the high strength and the lightweight of this material that good for improving the structural performance. Carbon fiber generally has excellent tensile properties, low densities, high thermal and chemical stabilities in the absence of oxidizing agents (X. Huang, 2009). Carbon fiber reinforces polymer is one of some composite materials that have high strength with lightweight material. G Padhi et al say that aircraft structural design refers to the pyramidal structure of testing, ranging from specimen tests to full-scale structure tests (G. Padhi et.al, 2004). At the fundamental level, open-hole tension tests are a part of the qualification process for composite parts that need to be joined to other parts in aircraft structures (MIL-HDBK-17-F). In order to find the material selection data and develop the data allowable composite data, several mechanical tests were carried out on these composites.

The tensile test is used to know the tensile strength and modulus of elasticity of the composite. The previous research by R.M. O'Higgins and colleagues already determined the open hole tension (OHT) characteristics of carbon fiber reinforced plastic (CFRP) and high-strength S2-glass fiber reinforced plastic (GFRP), the result of both composite showed similar damage and failure sequence that consisted of matrix cracks in the ±45° and 90° plies followed by extensive delamination before failure (R.M. O'Higgins, 2008). More recently work by Go Yamamoto and colleagues showed the observations of the tensile test comparison of carbon UD/Epoxy composite with four different types of Epoxy, it was revealed that the extent of concentrated stress acting on the intact fiber surface can be changed by modifying the mechanical properties of the matrix polymer (G. Yamamoto, 2019)

In this experiment, we use Carbon UD fiber and Lycal resin as the composite material manufactured with Vacuum Bagging Method. Specimens and testing process refer to ASTM D3039 for non-hole specimen and ASTM D5766 for the open-hole specimen of a tensile test standard for composite matrix polymers. The tensile experimental test of these Carbon Fiber Reinforce Polymer (CFRP) composites have been done to compare.

2. Methodology

2.1. Research Methodology

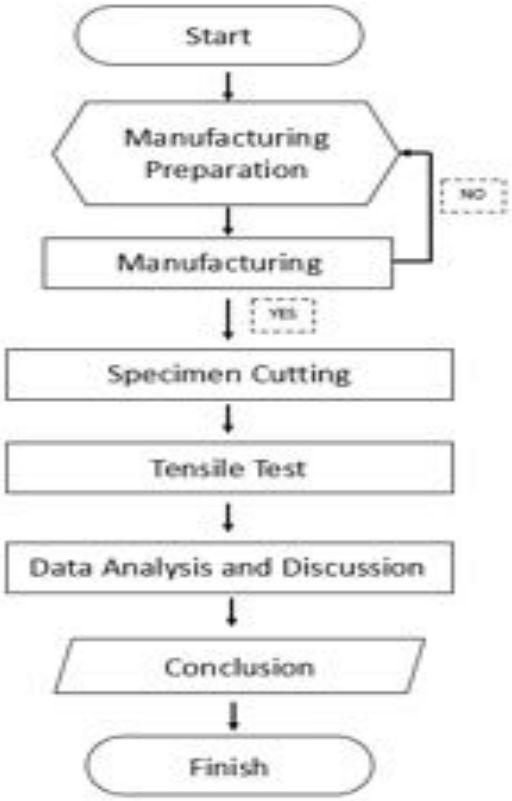

Figure 2-1: Research Methodology

2.2. Specimen Preparation

The specimens were made using Carbon UD, and Thermoset resin lycal GLR 1011 (N) with a hardener. The fiber volume fraction 40%. The manufacturing method using the vacuum bagging technique, Fig.2-2 shows the process of vacuum bagging technique (M. S. Ismail, 2019). The specimens were then cured at room temperature for 24 hours. Material cut with geometry as follows for tensile test non-hole specimen has thickness 1 mm, width: 15 mm, length: 250 mm, for tensile test hole specimen has thickness 1 mm, width: 15 mm, length: 250 mm, and diameter of the circular hole is manufactured by drilling at the center of the specimens 2.5 mm

2.3. Testing Method

All testing has been done using universal testing machine UTM RTF -2410 with capacity 100 kN and based on ASTM D3039 for tensile test non-hole specimen and ASTM D5766 for tensile test hole specimen. Fig.2-3. shows tensile and shear testing arrangement.

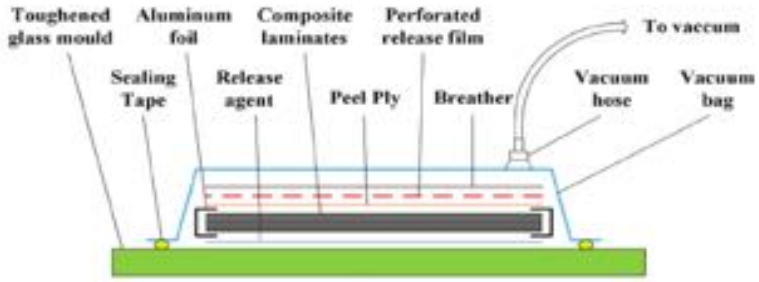

Figure 2-2: Vacuum Bagging Technique Process (M. S. Ismail, 2019)

Table 2-1: Composite Sample

Specimen Code	Specimen Content	Fiber Orientation
A	Carbon UD/Lycal	[0]
B	Carbon UD/Lycal with (Open Hole)	[0]

Figure 2-3: Testing Arrangement for Tensile Test Specimen

3. Result and Analysis

3.1. Data Analysis

The tensile test for non-hole specimens has been held using ASTM D3039 procedure standard. This test is used to obtain the composite tensile stiffness and strength. The maximum stress (σ) of the specimen can be determined by the following equation (ASTM D3039, 2017):

$$\sigma_i = P_i/A \tag{3-1}$$

The Maximum Strain (ε) on the mid-span of the specimen can be determined by the following equation:

$$\varepsilon_i = \delta_i/L_g \tag{3-2}$$

The Modulus of Elasticity E is a comparison between stress and strain which can be calculated by the following equation:

$$E^{chord} = \Delta\sigma/\Delta\varepsilon \tag{3-3}$$

The tensile test for hole specimen has been held using ASTM D5766 procedure standard ASTM D5766. The maximum ultimate open hole tensile strength (F_x^{OHTu}) of the specimen can be determined by the following equation:

$$F_x^{OHTu} = P^{max}/A \tag{3-4}$$

The Width to Diameter Ratio ($w/D\ ratio$) of the specimen can be determined by the following equation:

$$w/D\ ratio = \frac{w}{D} \tag{3-5}$$

The Diameter of Thickness Ratio of the specimen ($D/h\ ratio$) can be determined by the following equation:

$$D/h\ ratio = \frac{D}{h} \tag{3-6}$$

According to B. G. Green et .al, there are three types of failure mechanism category that occurs in the specimen after the test: first is pull-out, it occurred where the fiber dominated failure with extensive sub-critical damage; second is Brittle, it occurred where fiber dominated failure with little sub-critical damage, the fiber failure controls the laminate failure, and third is delamination that occurred when the matrix dominated failure along the entire gauge section that causes failure of the laminate (B.G. Green et.al, 2007).
To determine the failure typical modes of the composite after the tensile test, we refer to ASTM D3039, the typical mode of failure specimen can be determined by looking at the shape of failure as the following picture in figure 3-1.

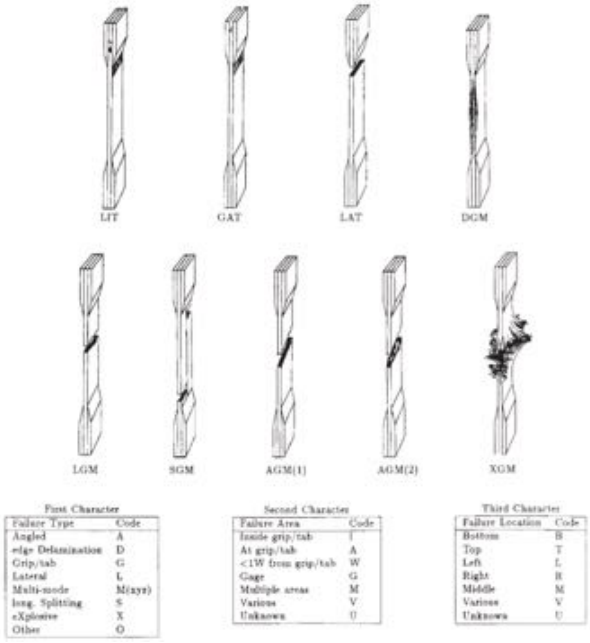

Figure 3-1: Failure Typical Modes ASTM D3039

3.2. Result

Tensile test of Carbon UD/ Lycal composite non-hole and the open hole that manufactured by Vacuum Bagging method has tested. The test was held with Universal Testing Machine RTF 2410 with 100 kN load Capacity. Below is the picture of the specimen before the test:

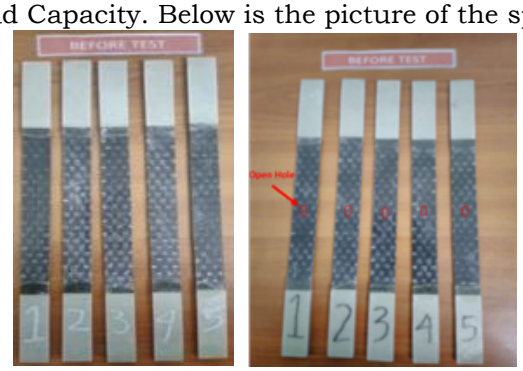

(a) (b)

Figure 3-2: Composite Sample Before Test a) Non-Hole and b) Open Hole

Refer to ASTM D5766, the diameter of the hole was counted from w/D ratio that equal to 6. So, the diameter of the hole is 2.5 mm.

The specimen after test showed as below picture,

(a) (b)

Figure 3-3: Composite Sample After Test (a) Non-Hole Composite (b) Open Hole Composite

Figure 3-3 shows that there is no different failure mechanism between the non-hole and open hole specimens tensile test, both of them had a damage splitting and delamination between fiber and matric that occurred across the entire gauge length of the specimen and parallel along the fiber direction. In line with this failure mechanism, according to ASTM D3039, the typical mode of both specimens is XGM (explosive, gage, in the middle). This finding is also supported with the previous research by Waleed H et.al which found In all open-holed carbon/epoxy specimens, the crack initiated in the vicinity of the hole at low very stress and then propagated parallel to the fiber direction, i.e. fiber-matrix splitting, and parallel to the applied load due to the transmission of shear forces between fiber and matrix (Waleed H et.al, 2019). The tensile test result shows in table 3-1.

Table 3-1: Tensile Test Result

Data	A Average	B Average
Stress (MPa)	1081,00 ± 0.03	899.04 ± 0.02
Elastic Modulus (GPa)	34.92 ± 0.45	41.87 ± 0.02
Break Point Strain (%GL)	0.45 ± 0.37	0.28 ± 0.5

The measured average value of the tensile strength of the non-hole composite is 1081,00 ± 0.03 MPa and the Elastic modulus is 34.92 ± 0.45 GPa, while the open hole composite has the average tensile strength value 899.04 ± 0.02 MPa and the modulus of elasticity 41.87 ± 0.02 GPa. This present value for the non-hole specimen is still lower than previous research by Waleed H et.al with the sample Carbon/Epoxy composite that has a strength value of 2.9 GPa and modulus of elasticity 155 GPa. In contrast, the stress value of the open-hole specimen is much higher than the Waleed H result which was only 358 MPa. The difference in the strength value is due to the dissimilar resin and kind of fiber we used so the compatibility of resin to the fiber is also divergent. The actual size of diameter and specimens have also affected the results.

A comparison of both sample's laminate stress-strain and modulus reduction curves is presented in Figures 3-4.

The open hole in the middle of the specimen becomes an initial failure while it took the tensile load. The stress concentration at the hole was an increase that causes the initiation and propagation in the region around the hole. From the result, we calculated that the Ultimate Tensile Strength (UTS) of the open-hole composite decreased 16.83% from the non-hole composite, and the modulus elasticity increased 16.60 %. The illustration of the different percentages shown in Figures 3-5.

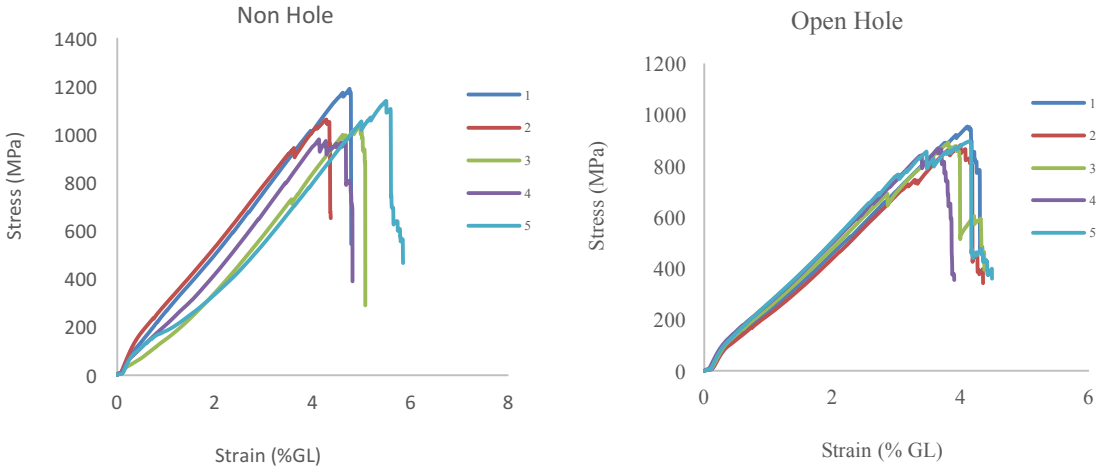

Figure 3-4: Stress- Strain Graph of (a) Non-Hole Composite (b) Open Hole Composite

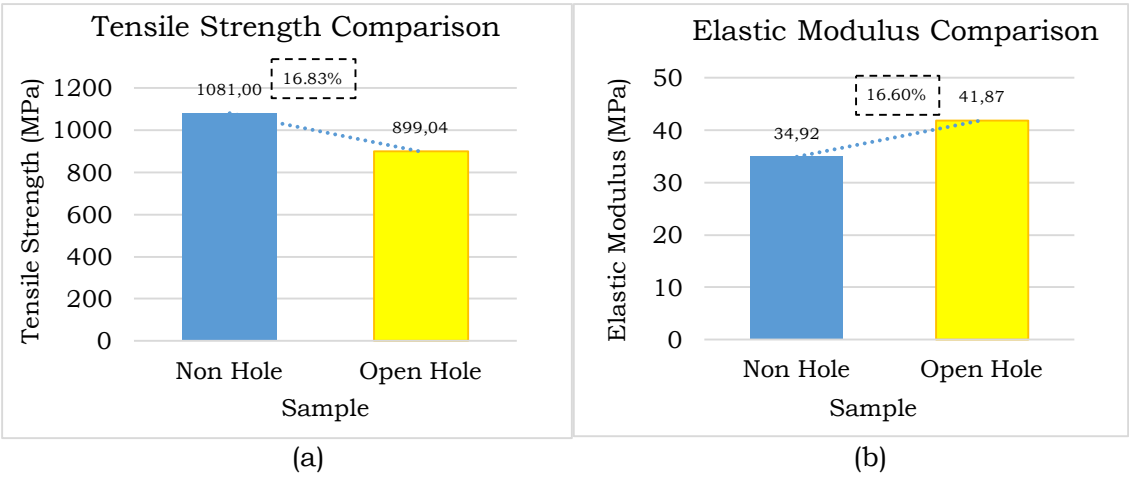

Figure 3-5: Comparison Graph of (a) Tensile Strength (b) Elastic Modulus

The simulation for the tensile test was done in FE software Abaqus. Specimen size and ply stacking configuration follow the experiment. Material properties for simulation were taken from the result of the experiment and parametric studies of another similar material. The Stress-strain graph comparing the results of simulation and experiment is shown below.

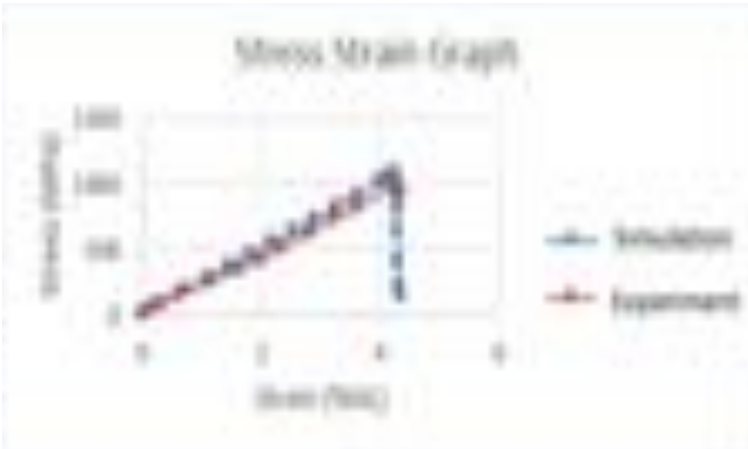

Figure 3-6: Stress-Strain Graph Comparison of Simulation and Experiment

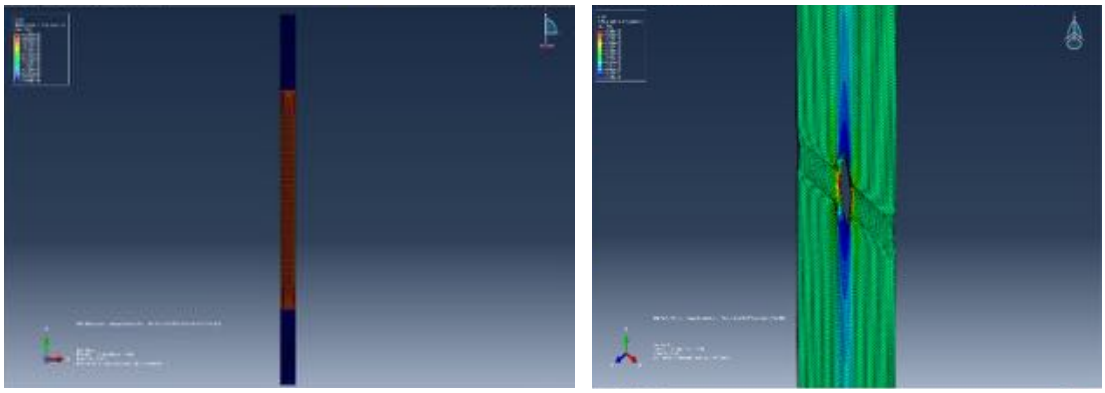

(a) (b)

Figure 3-7: Finite Element Simulation Result of (a) Non-Hole Composite (b) Open Hole Composite

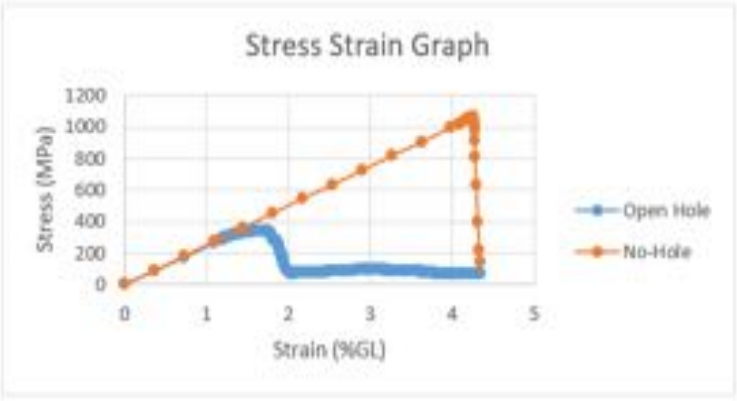

Figure 3-8: Stress-Strain Graph Comparison of Non-Hole and Open Hole Simulation

The simulation yields nearly the same stress-strain graph as the result of the experiment. The maximum stress in the experiment is 1081 MPa, while the simulation result yields 1064.98 MPa for non-hole specimens. Basse on the simulation results of the maximum stress value, when compared with the simulation, has a difference of 1.5%. Open hole simulation shows a significant reduction in maximum stress. The maximum stress on an open-hole specimen is 342.61 MPa, while in a non-hole specimen the maximum stress is 1064.98 MPa. There is approximately a 65% reduction of maximum stress in open hole specimens, compared to the non-hole specimen. High-stress concentration was observed in the hole sides, while the highest stress in the non-hole specimen was observed near tab edges. If we compare the results of simulations and experiments on open hole specimens, the maximum stress value has a difference of 61.9%. The simulation can be used to predict the result of the tensile test simulation. But when comparing it should be noted that the properties of carbon UD fiber and lycal resin, defined in the finite element model, have been determined experimentally, which could affect the accuracy of the calculation. it should be also taken into account that experimental data may differ slightly from the actual properties of the composites. Further research to find the proper material properties is needed, so the simulation can predict the experiment result accurately.

4. Conclusions

The result of the experimental test shows that the tensile modulus of elasticity for non-hole composite is 34.92 ± 0.13 GPa, with the Ultimate Tensile Strength of this composite is 1081± 0.03 MPa, and the modulus of elasticity for open-hole composite is 41.87± 0.02 GPa, with the Ultimate Tensile Strength of this composite is 899.04± 0.02 MPa. The UTS difference is 16.83% with the non-hole composite higher than an open hole and the modulus elasticity difference is 16.60% with the open hole specimen higher than the non-hole specimen. There is no different failure mechanism between the non-hole and open hole specimens tensile test, both of them had a damage splitting and delamination between fiber and matric that occurred across the entire gage length of the specimen and parallel along the fiber direction. The

simulation yields nearly the same stress-strain graph as the result of the experiment. The maximum stress in the experiment is 1081 MPa, while the simulation result yields 1064.98 MPa for non-hole specimens. This data will be used for the N219 Amphibious aircraft material database.

Acknowledgements

This research was supported and funded by Aeronautic Technology Centre – National Institute of Aeronautics and Space (LAPAN – Indonesia). The authors would like to thank to Mr. Gunawan Setyo Prabowo as head of Aeronautic Technology Centre for the support to this research.

The authors would like to thank the JTD LAPAN team, as the editor and publisher of this manuscript.

Contributorship Statement

LRI acts as main idea provider, prepared the specimen, tested the specimen, analyzed the results of test, and prepared the manuscript. AN prepared the specimen, tested the specimen, analyzed the results of test and simulation. RAP prepared the specimen, tested the specimen, analyzed the results of specimen, and prepare the specimen. RAR designed the simulation, simulated the test, analyzed the simulation results, and prepared the manuscript.

References

ASTM International, "D3039/D3039M-17 Standard Test Method for Tensile Properties of Polymer Matrix Composite Materials." ASTM International, 100 Barr Harbor Drive, PO Box C700, West Conshohocken, PA 19428-2959. United States, pp. 1–13, 2017.

ASTM International, "D5766/D5766M-02a Standard Test Method for Open Hole Tensile Strength of Polymer Matrix Composite Laminates," in *ASTM Book of Standards*, vol. 15.03, 2002, pp. 1–6.

B. G. Green, M. R. Wisnom, and S. R. Hallett, "An experimental investigation into the tensile strength scaling of notched composites," *Compos. Part A Appl. Sci. Manuf.*, vol. 38, no. 3, pp. 867–878, 2007, doi: 10.1016/j.compositesa.2006.07.008

G Padhi, C.T.Mccarthy, M.A. Mccarthy. "Experimental and Numerical Study of the Open-Hole Tensile Strength of Carbon / Epoxy Composites". Mechanics of Composite Materials · 2004.DOI:10.1023/B: MOCM.0000039744 .98869.0d.

G. Yamamoto, K. Koizumi, and T. Okabe, "Tensile Strength of Unidirectional Carbon Fiber-Reinforced Plastic Composites," in *Intech Open*, Sendai, Japan: Intech Open, 2019.

MIL-HDBK-17-F, Composite Materials Handbook, US DOD, published by ASTM International, Pennsylvania, USA.

M. S. Ismail, T. K. Kwan, M. I. Hussain, and Z. M. Zain, "Automatic compaction device for composite panel production at layup process: A case study," *Univers. J. Electr. Electron. Eng.*, vol. 6, no. 5, pp. 68–74, 2019, doi: 10.13189/ujeee.2019.061508.

R. M. O'Higgins, M. A. McCarthy, and C. T. McCarthy, "Comparison of open hole tension characteristics of high strength glass and carbon fibre-reinforced composite materials," *Compos. Sci. Technol.*, vol. 68, no. 13, pp. 2770–2778, 2008, doi: 10.1016/j.compscitech.2008.06.003.

W. H. Alhazmi *et al.*, "Notch tensile strength of carbon fiber/epoxy composite plate with a center hole under static and cyclic loading," *Procedia Struct. Integr.*, vol. 17, pp. 292–299, 2019, doi: 10.1016/j.prostr.2019.08.039

X. Huang, "Fabrication and properties of carbon fibers," *Materials (Basel).*, vol. 2, pp. 2369–2403, 2009, doi: 10.3390/ma2042369.

An Information Extraction of LAPAN Satellite's AIS Database for Ship Classifications on the Territorial Waters of Indonesia

Muazam Nugroho[1], Nurrochman Ferdiansyah[1], Dicka Ariptian Rahayu[1], Rizki Permala[1], Patria Rachman Hakim[1], Wahyudi Hasbi[1]

[1]Satellite Technology Center, National Institute of Aeronautics and Space (LAPAN), Indonesia

e-mail: muazam.nugroho@lapan.go.id

Received: 23-03-2021. Accepted: 06-05-2021. Published: 30-06-2021

Abstract

LAPAN participates in maritime surveillance with Automatic Identification System (AIS) payloads on the LAPAN-A2 and LAPAN-A3 satellites. AIS data consists of dynamic messages and static messages. A complete data set is needed to facilitate monitoring and analysis of ship traffic. This complete data contains the ship's identity (static message) and its navigation status (dynamic message). This data set can be obtained by processing data in the database. This study focuses on extracting information from the LAPAN satellite AIS database with combining AIS data from dynamic and static messages to get the number of vessels grouped by vessel type in the territory of Indonesia with coordinates 95BT / 141BT, -11LS / 6LU with the data period January to December 2019 monthly. The information extraction on AIS satellite data for the classification of vessel types has been completed. The result of the information extraction is the greater the period of static data, the lesser the ship type is unknown / null, with average percentage of null vessel type is 73.76%, 56.93%, and 39.58% for static data for a period of 1 month, 3 months, and 1 year respectively. The results also show cargo ships have the highest number of vessels, with the number of vessels shows a downward trend along the year of 2019.

***Keywords**: AIS, database, LAPAN satellite, marine traffic*

1. Introduction

Indonesia is an archipelago country, with sea area larger than land area, making Indonesia one of the largest maritime countries in the world. The Indonesian sea area is one of the busiest shipping lanes in the world. Many ships passing through Indonesian territory, such as cargo ships, passenger ships, and fishing vessels. Large areas of the sea and dense maritime traffic require a good monitoring system to maintain security and reduce the level of problems or law violations at sea. The existence of a monitoring system on the movement of ships in Indonesia can reduce the level of the number of problems that occur in Indonesian seas (Judianto & Wahyudiono, 2014).

Automatic Identification System (AIS) is a technology used for monitoring of ship traffic around the world. AIS operates on the VHF channel with a frequency of 161,975 MHz and 162,025 MHz for the purpose of sending and receiving ship-specific information (ITU, 2012). Some of the information obtained from the AIS system includes Maritime Mobile Service Identity (MMSI), Position, Course, Call Sign, and AIS base station (Hu et al., 2012). AIS devices operate using a time division multiple access (TDMA) system, which makes it possible to send around 2000 reports per minute (Stupak, 2014). Messages sent by AIS devices from ships can be received by fellow ships, terrestrial-based AIS receiving stations, and satellite-based AIS receiving stations (space-borne AIS). The space-borne AIS has an advantage in the radius of receiving AIS messages because of its height (Ball, 2013). The National Aeronautics and Space Agency (LAPAN) participated in Indonesia's maritime surveillance by launching two micro satellites containing the AIS receiver, namely the LAPAN-A2 satellite in 2015 and LAPAN-A3 in 2016. The LAPAN-A2 satellite has a near-equatorial orbit with an altitude of 650 km while the LAPAN-A3 satellite has a sun-synchronous polar orbit with an altitude of 515 km. LAPAN-A2 with its orbit allows it to pass through Indonesian territory 14 times a day, while the polar orbit on the LAPAN-A3 satellite allows for global coverage (Karim et al., 2018). With these

different types of orbit, the two satellites could complement each other's AIS data recorded by each satellite.

Several studies have been conducted regarding the use of AIS data. (Yitao et al., 2017) proposed a route extraction method based on satellite-AIS which includes data preprocessing, structural similarity calculation, clustering and route extraction. (Zhou et.al, 2019) presents a methodology for clustering ship behavior in an area and classifying ships into these clusters based on the static ship characteristics. (Kundakci & Nas, 2018) developed a desktop application to enable visualization of vessel movements to map the ship movements according to vessel types and enables analysts to evaluate waterway traffic density in the target area. The AIS system is used in numerous applications that can contribute to a significant increase in the safety of passengers, crew, cargo and ships, as well as the marine environment (Stupak, 2014).

This study focuses on extracting information from the AIS LAPAN database to obtain information on the number of vessels based on unique MMSI which are grouped according to the type of ship entering Indonesian waters with coordinates 95BT / 141BT, -11LS / 6LU in the period January to December 2019. The method used in this study focuses mainly on AIS data processing in the database, such as database merging, data cleaning, view creation, and data retrieval using SQL queries. The purpose of this paper is to provide an overview of the classification of ships passing in Indonesian territorial waters during a time period.

2. Methodology

The method used in this study focuses mainly on AIS data processing in the database, such as database merging, data cleaning, view creation, and data retrieval using SQL queries. The process of extracting information from the LAPAN satellite AIS database is described in the following flowchart:

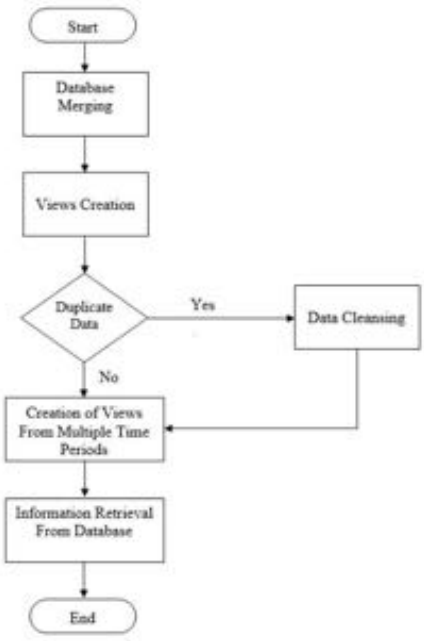

Figure 2-1: process of extracting information from the LAPAN satellite AIS database

It is explained in the IMO document (2002) that AIS messages transmitted by ships has four different types with different transmission times:

1. Static Information, which is information entered during the installation of AIS onboard and can also be changed if there is a change in the legal documents of the ship, such as a change in the name and ownership of the ship.
2. Dynamic Information, which is information that contains the ship's navigation status which will automatically change according to the data obtained from sensors connected to the AIS tool.
3. Sailing information, which is information entered and updated manually by the crew.
4. Short safety-related messages.

Details of the AIS information can be seen in the following figure:

Static information	Dynamic information	Voyage related information
Every 6 minutes and on request by a competent authority	*Dependent on speed and course alteration*	*Every 6 minutes, when data is amended or on request*
MMSI (Maritime Mobile Service Identity)	**Ship's position**	**Ship's draught**
Call sign and **name**	**Position Time stamp** in UTC	**Hazardous** cargo (type)
IMO Number	**Course over ground** (COG)	**Destination** ETA (Estimated Time of Arrival)
Length and beam	**Speed over ground** (SOG)	
Type of ship	**Navigational status** (underway, at anchor, moored...)	
Location of position fixing antenna	Rate of turn (ROT)	

Figure 2-2: information transmitted by ship (IMO, 2002)

In static message there is a field of MMSI (Maritime Mobile Service Identity) which is a unique code for the ship. The making of the MMSI code is regulated in the ITU-R M.585-8 document, it explains that the MMSI code has a nine-digit length with the format $M_1I_2D_3X_4X_5X_6X_7X_8X_9$ where the initial three digits represent the code of origin of the ship's country. Static message and shipping message are transmitted every 6 minutes or when there is a request from the authorities while for dynamic information the transmission interval is carried out according to the status and speed of the ship:

Ship's dynamic conditions	Nominal reporting interval
Ship at anchor or moored and not moving faster than 3 knots	3 min[1]
Ship at anchor or moored and moving faster than 3 knots	10 s[1]
Ship 0-14 knots	10 s[1]
Ship 0-14 knots and changing course	3 1/3 s[1]
Ship 14-23 knots	6 s[1]
Ship 14-23 knots and changing course	2 s
Ship >23 knots	2 s
Ship >23 knots and changing course	2 s

Figure 2-3: transmission data interval

2.1. Database Processing

As previously mentioned, LAPAN-A2 and LAPAN-A3 satellites carry the AIS receiver payload into orbit. LAPAN-A2 satellite in near-equatorial orbit receives AIS messages around the equatorial line, while with its polar orbit, LAPAN-A3 satellite receives AIS messages which are more evenly distributed around the world. The data stored in the satellite is routinely acquired by the earth station and stored in a database management system. The AIS data from these two satellites are stored in different databases. For the purposes of utilization, AIS data from separate databases are combined to complement each other in order to obtain more complete information.

The reason for using a database system to store data is that the database offers speed, accuracy, reporting, and thoroughness as its advantages (Suehring, 2002). To store satellite AIS data into a database, a Database Management System (DBMS) is required. MySQL is a DBMS with a relational system, also known as a relational database management system (RDBMS). Relational databases store data in separate tables (MySQL, 2021).

In the database, AIS messages are separated into tables based on the type of information. Dynamic messages (which have position coordinate fields) are entered in the Position Report table, whereas static messages are entered in the static table. The purpose of this paper is to obtain information on ship types in a certain area and at a certain time, then the information needed is the position data, the time contained in the position report table and the ship type data in the static table.

The method used in this study focuses on processing the AIS database for the LAPAN-A2 and LAPAN-A3 satellites. A summary of the research methods is described below:

2.1.1. Database Merging

The AIS database for the LAPAN-A2 and LAPAN-A3 satellites is combined into a new database. The table format in the database is made exactly the same as the database before it is merged. What is different is that the new database contains AIS messages originating from the LAPAN-A2 and LAPAN A3 satellites, and the information period is grouped into monthly period.

Figure 2-4: Merging of the AIS database for the LAPAN-A2 and LAPAN-A3 satellites

2.1.2. Views Creation

In a MySQL database, a view can be defined as a virtual table. The contents of this table can come from other tables or a combination of several tables. The purpose of creating a View is to make it easier to write queries and speed up data display, especially if the query is repeated (DuBois, 2014). In this study, making a view from each monthly database aims to retrieve the ship type data in the static table into the location message row in the Position Report table.

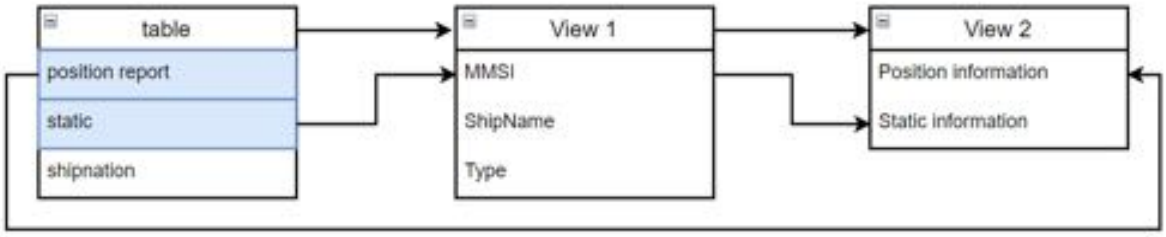

Figure 2-5: Creation of Views on the LAPAN satellite AIS database

There are 2 views created. The first view (View 1) contains a list of ships with unique data on MMSI, ship name, and vessel type. This data is obtained from a static table. The second view (View 2) contains a combined data from the Position Report table with data from View 1 based on MMSI. This combination will provide data on the ship's position complete with the name and type of ship. Data from View 2 is what data retrieval and analysis is carried out.

2.1.3. Data Cleansing

Filter queries use distinct on a static table to filter MMSI, ship name and type so there is no duplication, in other words, only 1 unique MMSI value represents 1 ship. Furthermore, the max (time) filter is applied in the Position Report table to obtain a more valid vessel type.

2.1.4. Creation of Views from multiple time periods

Static data in the database is usually incomplete, which is no static data from the MMSI in the Position Report data, which will cause the ship type to be unknown / NULL. This could be due to not receiving messages from the ship or errors during the transmission of AIS messages.

Table 2-1: Period of analyzed Position Report data and static data

no	Position Report	Static Data 1 month	Static Data 3 months	Static Data 1 year
1	Jan-19	Jan-19	Jan, Feb, Mar 2019	Jan - dec 2019
2	Feb-19	Feb-19		
3	Mar-19	Mar-19		
4	Apr-19	Apr-19	Apr, May, Jun 2019	
5	May-19	May-19		
6	Jun-19	Jun-19		
7	Jul-19	Jul-19	Jul, Aug, Sep 2019	
8	Aug-19	Aug-19		
9	Sep-19	Sep-19		
10	Oct-19	Oct-19	Oct, Nov, Dec 2019	
11	Nov-19	Nov-19		
12	Dec-19	Dec-19		

In this study, a view was made of creating views by taking static data from several different time periods, namely the period of one month, 1 quarter, and 1 year. The purpose of retrieving static data from several time periods is to see how much influence the static data period has on the completeness of the data. The initial hypothesis is that the greater the static data period, the more complete the information will be. Table 2-1 describes the data period analyzed.

To combine the data in separate tables, a field is needed in both tables. This field is the MMSI (Maritime Mobile Service Identity) field. Here are the relationships between tables to produce the desired information:

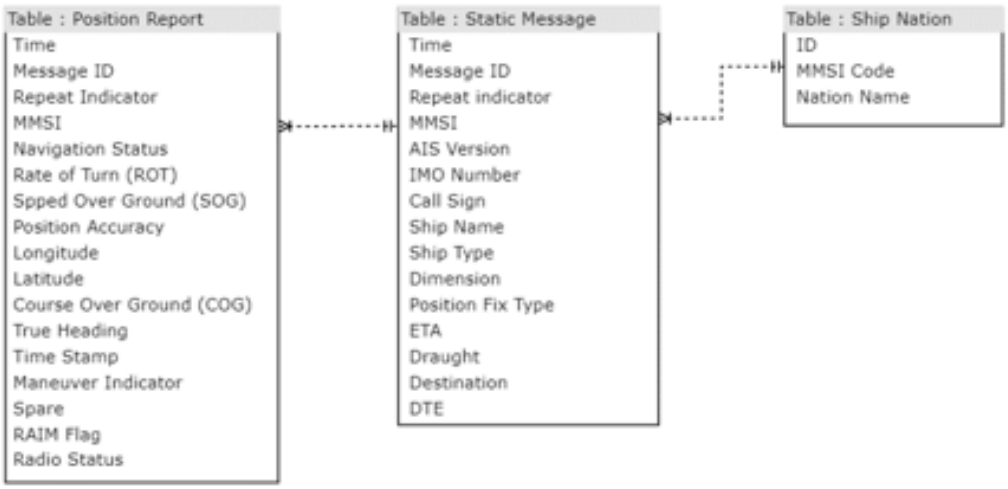

Figure 2-6: Relationships between tables in a database

2.2. Information Retrieval from the Database

Data retrieval is done by performing a MySQL query to calculate the number of unique MMSIs with time and region filters according to the needs. The following is the MySQL query used:

```
mysql>  SELECT  type, COUNT(*) FROM (select * from View2 where date(time) >='2019/01/01' and
        DATE(time)<='2019/01/31' and (lattd>=-11 and lattd<=6) and (longtd>=95 and
        longtd<=141) )
        AS A JOIN
        (select distinct mmsi, max(time) AS time from PositionReport where date(time)>=
        '2019/01/01' and DATE(time)<='2019/01/31' and (longtd>=95 and longtd<=141)
        and (lattd>=-11 and lattd<=6) group by mmsi)  AS B ON A.MMSI=B.mmsi AND
        A.Time=B.Time GROUP BY type;
```

This query will generate a number of unique MMSIs at a predetermined time and region with the vessel type of the MMSI.

3. Result And Discussion

After going through the data selection and classification process, the AIS satellite LAPAN-A2 and LAPAN-A3 data were obtained in the 95BT / 141BT, -11LS / 6LU areas in the period January to December 2019 which had the following data:

1. Ship Classification data with 1-month static data period

The following is the number of vessels by type in the period from January to December 2019 in the area 95BT / 141BT, -11LS / 6LU with static data for a period of 1 month:

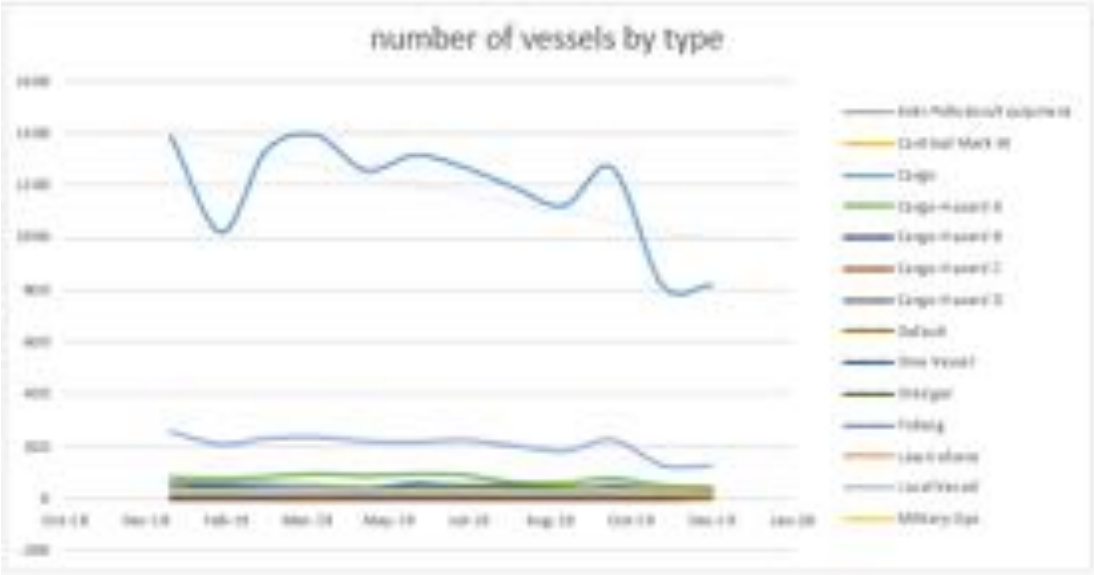

Figure 3-1: Graph of the number of vessels by type with a static data period of 1 month (without nulls)

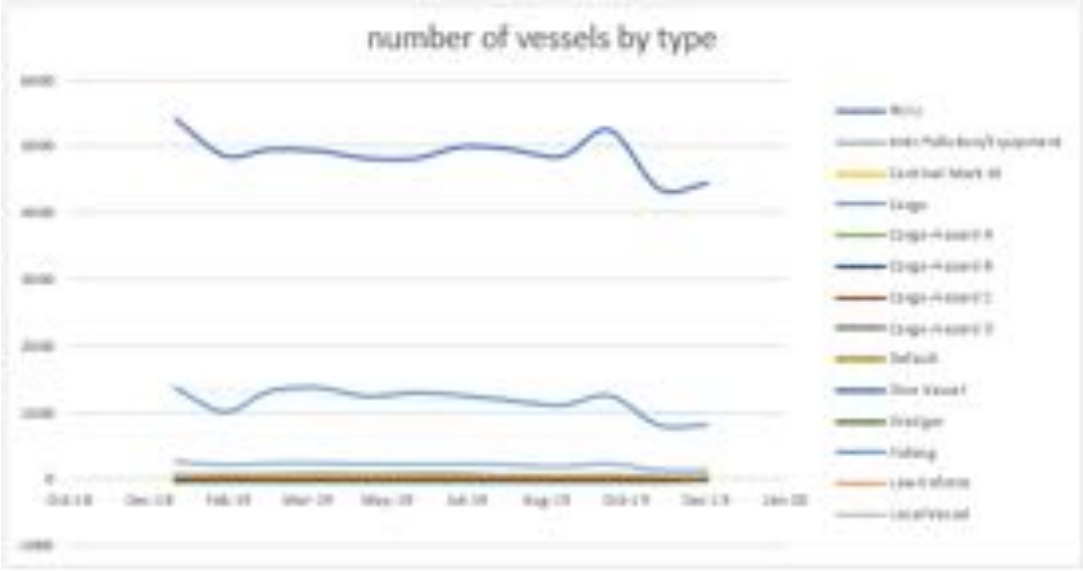

Figure 3-2: Graph of the number of vessels by type with a static data period of 1 month (with nulls)

From the graph above, it can be seen that the top 3 types of vessels are the unknown ship type (NULL), cargo type, and tanker type. Table 3-1 shows details of the number of unique MMSIs based on the 3 types of vessels:

Table 3-1: number of unique MMSIs from top 3 vessel type

		Ship Type	
month	**NULL**	**Cargo**	**Tanker**
Jan-19	5425	1386	251
Feb-19	4862	1021	204
Mar-19	4957	1334	225
Apr-19	4938	1390	231
May-19	4822	1257	215
Jun-19	4821	1315	212
Jul-19	5004	1269	219
Aug-19	4954	1192	199
Sep-19	4852	1122	177
Oct-19	5256	1265	220
Nov-19	4353	816	123
Dec-19	4434	820	121

2. Ship Classification data with 3-month static data period

The following is the number of vessels by type in the period from January to December 2019 in the area 95BT / 141BT, -11LS / 6LU with static data for a period of 3 month:

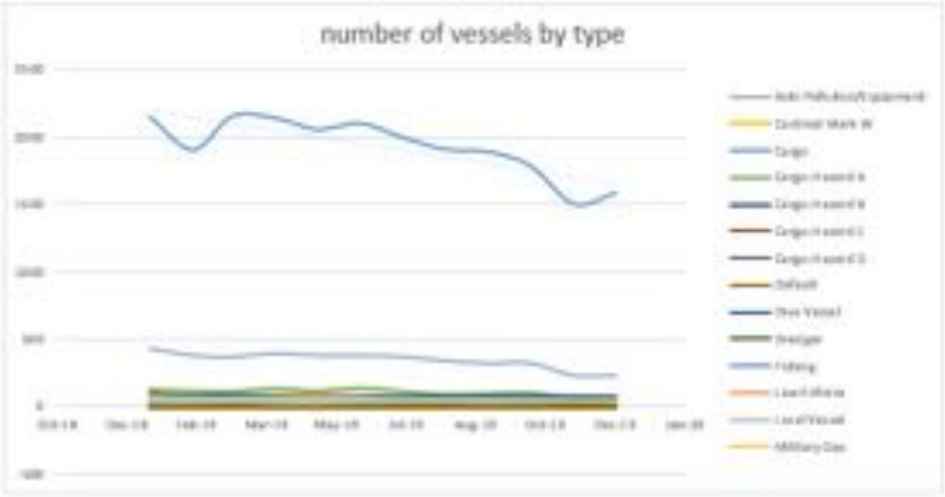

Figure 3-3: Graph of the number of vessels by type with a static data period of 3 month (without nulls)

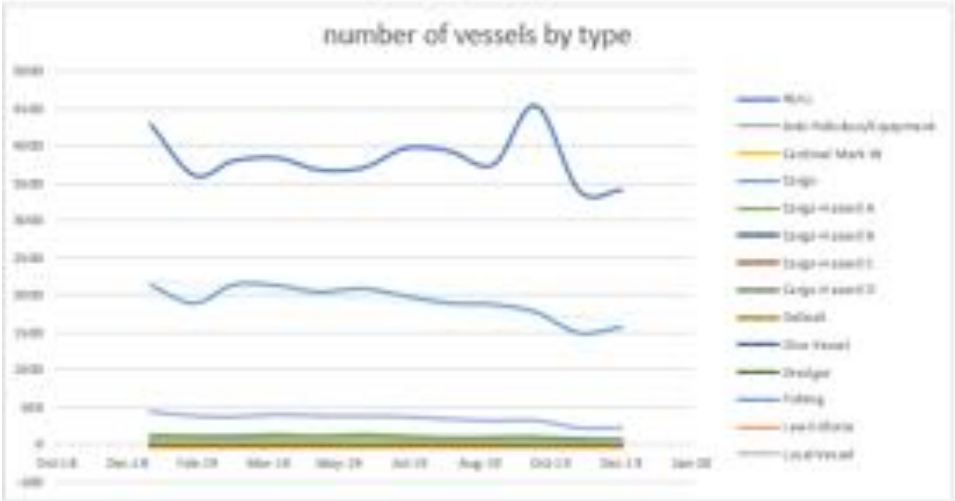

Figure 3-4: Graph of the number of vessels by type with a static data period of 3 month (with nulls)

From the graph above, it can be seen that the top 3 types of vessels are the unknown ship type (NULL), cargo type, and tanker type. Table 3-2 shows details of the number of unique MMSIs based on the 3 types of vessels:

Table 3-2: number of unique MMSIs from top 3 vessel type

	Ship Type		
month	**NULL**	**Cargo**	**Tanker**
Jan-19	4291	2148	428
Feb-19	3605	1902	378
Mar-19	3800	2152	367
Apr-19	3838	2140	393
May-19	3677	2054	377
Jun-19	3707	2100	376
Jul-19	3969	1996	369
Aug-19	3928	1908	338
Sep-19	3747	1888	320
Oct-19	4535	1785	322
Nov-19	3393	1504	230
Dec-19	3411	1586	231

3. Ship Classification data with 1-year static data period

The following is the number of vessels by type in the period from January to December 2019 in the area 95BT / 141BT, -11LS / 6LU with static data for a period of 1 year:

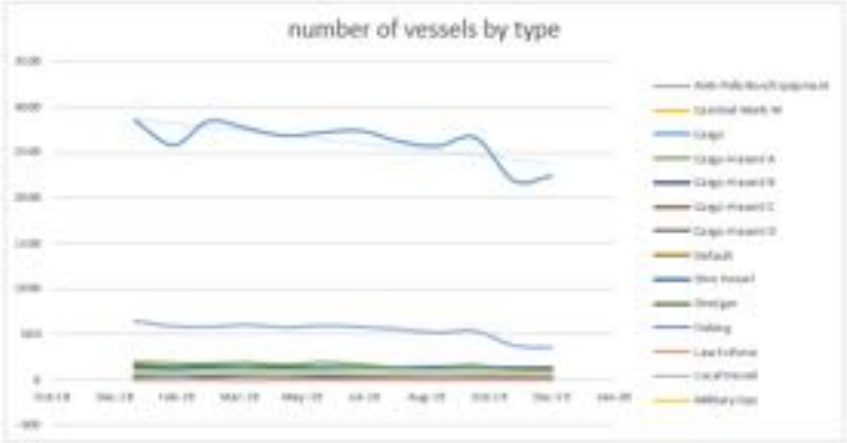

Figure 3-5: Graph of the number of vessels by type with a static data period of 1 year (without nulls)

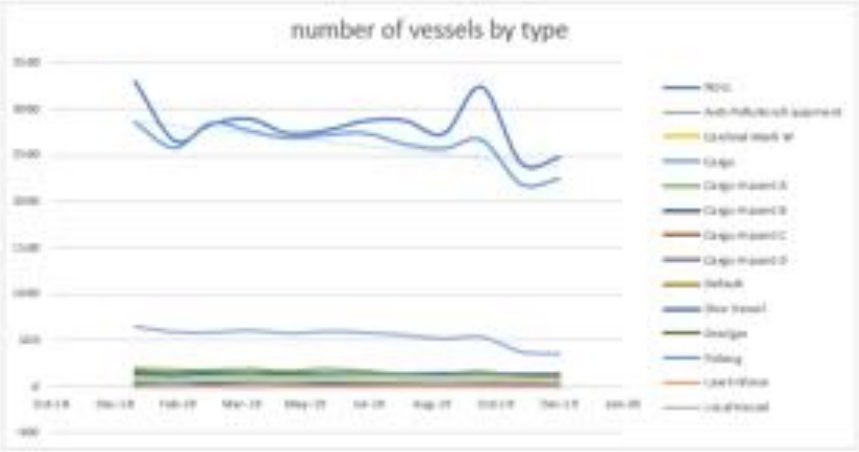

Figure 3-6: Graph of the number of vessels by type with a static data period of 1 year (with nulls)

From the graph above, it can be seen that the top 3 types of vessels are the unknown ship type (NULL), cargo type, and tanker type. Table 3-3 shows details of the number of unique MMSIs based on the 3 types of vessels:

Table 3-3: number of unique MMSIs from top 3 vessel type

	Ship Type		
month	**NULL**	**Cargo**	**Tanker**
Jan-19	3290	2845	651
Feb-19	2652	2574	591
Mar-19	2824	2837	584
Apr-19	2887	2759	606
May-19	2730	2680	576
Jun-19	2764	2714	596
Jul-19	2865	2732	582
Aug-19	2870	2615	556
Sep-19	2726	2566	518
Oct-19	3231	2658	536
Nov-19	2408	2185	371
Dec-19	2470	2240	348

4. Conclusion

By utilizing the AIS data in the database, we can get some statistical information on ships that are in Indonesian waters in the period from January to December 2019. Before this information can be obtained, it needs to be processed first in the database, one of which is by creating a view / relation table so that the data obtained to be complete.

In this study, information extraction on AIS satellite data for the classification of ship types has been completed. The result of extracting this information is that the greater the period of static data, the lesser the ship type is unknown / null, the average percentage of ship types null is 73.76% for a static data period of 1 month, 56.93% for a static data period of 3 months, and 39.58% for static data for a period of 1 year. In the period from January to December 2019, the largest type of ship was cargo, and it can be seen that the number of cargo ships has a downward trend along the year of 2019.

Acknowledgements

Authors sincerely appreciate Mr. Ir. Mujtahid, M.T. as the Head of Satellite Technology Center and LAPAN Satellite's operators for their support regarding AIS data used on this research.

Reference

A. Karim, R. Permala, M. Mukhayadi, W. Hasbi. LAPAN-A2 and LAPAN-A3 Automatic Identification System (AIS) Satellitte Data Correction using Interpolation and Extrapolation Method. Jurnal Teknologi Dirgantara vol. 16 no.2 December 2018. http://dx.doi.org/10.30536/j.jtd.2018.v16.a3049

Ball H., 2013. Satellite AIS for Dummies Special Edition. John Wiley & Sons Canada, Ltd. Mississauga. ISBN: 978-1-118-48494-4

DuBois Paul, 214. MySQL Cookbook, Third Edition. O'Reilly Media, Inc. Sebastopol, CA. ISBN: 978-1-449-37402-0

IMO: Recommendation on Performance Standards for a ship-borne Automatic Identification System (AIS). MSC 74(69) Annex 12. London: IMO, 2002

International Telecommunications Union. Interim Solutions for Improved Efficiency in the Use of the Band 156–174 Mhz by Stations in the Maritime Mobile Service ; International Telecommunications Union: Budapest, Hungary, 2012

Judianto, C. T., A. Wahyudiono. Automatic Identification System And Surveillance Technology For Indonesia Marine Security On Lapan-A2 Satellite. International Seminar of Aerospace Science and Technology II: 115 – 122, 2014

Kudakci B., Nas S. Mapping Marine Traffic Density By Using Ais Data: An Application In

The Northern Aegean Sea. Polish Maritime Research 4 (100) 2018 Vol. 25 page 49-58, 2018. https://doi.org/10.2478/pomr-2018-0131

MySQL. (2021). MySQL Documentation. Retreived March 19, 2021, from https://dev.mysql.com/doc/refman/8.0/en/what-is-mysql.html

Q. Hu, Yi Jiang, X. Sun, S. Zhang. Development of Automatic Indetification System Autonomous Positioning System. Journal Sensors, (2012). https://doi.org/10.3390/s151128574

Suehring Steve, 2002. MySQL Bible. Wiley Publishing, Inc. New York. ISBN: 0-7645-4932-4

T. Stupak. Influence of Automatic Identification System on Safety of Navigation at Sea. Journal of Marine Navigation and Safety of Sea Transportation Vol. 8 No. 3, 337-341, 2014. http://dx.doi.org/10.12716/1001.08.03.02

Yitao W., Lei Y., Xin S. Route Mining from Satellite-AIS Data Using Density-based Clustering Algorithm. 3rd International Symposium on Big Data and Applied Statistics, 2017. http://dx.doi.org/10.1088/1742-6596/1616/1/012017

Zhou Y, Daamen W, Vellinga T., Hoogendoorn S.P. Ship classification based on ship behavior clustering from AIS data. Ocean Engineering volume 175 1 March 2019 Pages 176-187, 2019. https://doi.org/10.1016/j.oceaneng.2019.02.005

Powered Landing Guidance Algorithms Using Reinforcement Learning Methods for Lunar Lander Case

Larasmoyo Nugroho[1], Novanna Rahma Zani[2], Nurul Qomariyah[2]
Rini Akmeliawati[3], Rika Andiarti[4], Sastra Kusuma Wijaya[5*]

[1]Rocket Technology Center, National Institute of Aeronautics and Space (LAPAN), Indonesia
[2]Electronics Department, Politeknik Elektronika Negeri Surabaya, Indonesia
[3]School of Mechanical Engineering, University of Adelaide, Australia
[4]Deputy of Aerospace Technology, National Institute of Aeronautics and Space (LAPAN), Indonesia
[*5]Physics Department, Universitas Indonesia, Depok, Indonesia

e-mail: larasmoyo.nugroho@lapan.go.id,
novannarahmazani@gmail.com, nurulnq11082000@gmail.com,
rini.akmeliawati@adelaide.edu.au, rika.andiarti@lapan.go.id,
*corresponding e-mail: skwijaya@sci.ui.ac.id

Received: 23-03-2021. Accepted: 22-04-2021. Published: 30-06-2021

Abstract

Any future planetary landing missions, just as demonstrated by Perseverance in 2021 Mars landing missions require advanced guidance, navigation, and control algorithms for the powered landing phase of the spacecraft to touch down a designated target with pinpoint accuracy (circular error precision < 5 m radius). This requires a landing system capable to estimate the craft's states and map them to certain thrust commands for each craft's engine. Reinforcement learning theory is used as an approach to manage the mapping guidance algorithm and translate it to engine thrust control commands. This work compares several reinforcement-learning-based approaches for a powered landing problem of a spacecraft in a two-dimensional (2-D) environment and identifies their advantages or disadvantages. Three methods in reinforcement learning, namely Q-Learning, and its extensions such as DQN and DDQN. They are benchmarked in terms of rewards and training time needed to land the Lunar Lander. It is found that the Q-Learning method also called Heuristic produced the highest efficiency. Another contribution of this paper is to show the combination usage of online weights θ between the action selection process and action evaluation process, yields a higher reward, instead of separating them, which significantly enhances their optimization performance. The simulations of the powered guidance performance in a 2-D simulation environment highlight the effectiveness of DQN to handle multiple neural networks better than DDQN.

***Keywords**: planetary landing, lunar lander, Q-Learning, DQN, DDQN.*

Nomenclature

QL	=	Q-Learning Method also called as Heuristic Method
DQN	=	Deep Q-Learning Network
DDQN	=	Double Deep Q-Learning Network
MDP	=	Markov Decision Process
TD	=	Temporal Differential

1. Introduction

Nowadays, landing rockets are already part of our daily life. Back then, this feat of engineering even at the level of concept seemed very inconvenient and mind-grinding to be fulfilled. Nevertheless, constant human's eagerness and experiences gained in interplanetary missions gave a stream of new technical insights and increasing know-hows. One such case is the landing mission of Apollo's Lunar Lander Module named as the Eagle. The success of the Eagle's landing mission on the moon has become a solid reference for rocket technologies in landing on earth's surface that eventually adopted and

mastered by Space-X to land Falcon rocket as reusable launch vehicle and Starship as their next RLV. (Klumpp, 1974)(Latyshev et al., 2021)

Future highly anticipated, science-driven, robotic and human missions to Mars will require a high degree of landing accuracy. Surely, the next generation of Mars landers will necessitate more advanced guidance and control capabilities to satisfy the increasingly stringent accuracy requirements driven by the desire to explore Mars regions that still necessitated to be researched further intensively. Probably the most demanding mission segments for a Mars mission is the powered descent phase, where the goal is to achieve a soft pinpoint landing, which we will define as the norm of the position error less than 5m and the magnitude of the landing velocity below 2 m/s, with the velocity vector directed primarily downward, and negligible deviation from an upright attitude and zero rotational velocity. In a powered descent phase, a few of the lander's sensors such as radar altimeter are blinded and hindered by the heat shield, therefore the lander's guidance, navigation, and control system should quickly estimate the state of the lander before drifted several km downrange and crossrange, and subsequently estimates states again to attain a soft landing at the designated position, usually under one minute after the heat shield is jettisoned. (Gaudet, Linares, & Furfaro, 2018)

Landing accuracy is important for several reasons. First, given accurate high-resolution maps of the Martian surface, the pinpoint-landing problem subsumes the hazard avoidance problem, as a hazard-free landing site can be targeted. Second, dropping a rover nearest to a specific landing zone could avert malfunctioning rover due to large diverted distance. In fact, some terrain conditions could prohibit the rover to go through unless the spacecraft lander delivered the rover with a high degree of accuracy. As a plus, reducing the distance the rover travels could relax the design requirements for the rover, especially battery in rover mass. Of course, accurate landing to just a few meters could reduce mission risk and expand the feasibility of missions. (Gaudet, Linares, & Furfaro, 2018)

2. Methodology

The Lunar Lander project is a simulation to solve the challenges of a lunar lander using reinforcement learning (RL). Open AI Gym is an open-source platform that provides an environment for applying RL to many classic 2-D engineering problems such as the Cart Pole and Lunar Lander. In this paper, we observe the performance of a few reinforcement learning (RL) algorithms in a specific environment that is OpenAI Gym's Lunar Lander-v2 continuous state space.

Generalized reinforcement learning algorithms such as Q-Learning do well in finding optimal policies for stochastic Markov Decision Problem (MDP) with discrete state and action spaces, nevertheless, problems arise when state spaces are continuous. (Von Dollen, 2017)

2.1. Related Works

The adaptation of Q-Learning that are well suited for discrete states problem into continuous states problem usually lies in the overestimation of actions values that produced high positive bias of the Q-learner in approximating the maximum expected value using the maximum action value. (Von Dollen, 2017)

Neural networks and other estimators could be used as a strategy to estimate value functions, besides binning the continuous state space into discrete variables.

Hado van Hasselt introduced the concept of Double Deep Q-Learning Network (DDQN) where two estimators are introduced to separate the concerns of the expected value from the maximization of the action values, and while this method may show an underestimation of expected values, it could help the agent to yields convergence to optimal policies faster in comparison to Deep Q-learning (DQN). (Hasselt et al., 2016)

The environment starts by sending state values to the agent, whose knowledge will then become a reference for selecting an action in response to the state. After that, the agent will update his knowledge with the reward value obtained from the environment to evaluate his last action. Terminal state value is sent by the environment when a predetermined episode is reached by the loop. In reinforcement learning, the selection of actions for each state value obtained during learning greatly affects the success of learning. Random selection of actions is usually called exploration while selecting actions based on the largest value function is called exploitation.

There is a case in the lunar lander landing motion, which is the part of the rewards obtained during training that will affect the landing lunar lander movement. This landing motion can be arranged using several methods in reinforcement learning. Reinforcement Learning assumes that there are agents located in the environment (Ermacora et al., 2016)(Brockman et al., 2016). The agents are required to continuously update their own beliefs about the world, about which actions are good and which are not in order to become an example of an efficient learner (Cini et al., 2020). Some of the reinforcement learning methods that will be discussed and implemented in the lunar lander's mission are the DQN and DDQN. The results of the training from the implementation of several of these methods will be compared to find out what method is the most optimal in carrying out the landing mission.

2.2. Problem Definition

Our problem is based on the OpenAI Gym's LunarLander-version 2 environment. OpenAI Gym is a toolkit for developing and comparing reinforcement learning algorithms exerted to a physically rigid body in a 2-dimensional space environment. In particular, this project focuses on the Apollo's Eagle Module landing problem, and the goal is to teach the "lunar lander" agent to successfully land on randomly generated surfaces of the "moon". The following formally defines the state space, action space, and the reward for this RL problem, according to (Mnih et al., 2015).

State-space. The state-space for LunarLander-v2 is an eight-dimensional vector.

1. providing information of the agent's position in space, X and Y
2. horizontal (Vx) and vertical velocity (Vy)
3. pitch orientation in space (θ)
4. angular velocity ($\dot{\theta}$)
5. two flags left_leg, right_leg indicating whether the left foot/right foot is in contact with the ground.

Action space. The input actions provided by the RL agent comprised of firing a thruster to the left or the right, burning the center main engine, or shutting it off, with a total of 4 discrete input actions.

Environment. The environment has a landing pad at coordinate point (0,0) in the frame. Fuel is infinite. (Yu, 2019)

Reward. The agent receives -0.3 points for firing its main engine for each frame, and landing on the landing pad is 100-140 points, which can be lost if the agent moves away from the pad. 10 points will be rewarded when each leg contact with the ground. The episode is terminated if the agent lands or crashes, in which case receiving -100 points for a crash or +100 for a successful landing. 100 to 140 points will be rewarded when the lander moves from the top of the screen to the landing pad, and the variation ranges depending on the lander's positioning on the pad.

Goal. The Markov Decision Problem is considered solved and achieved a score of 200 points or higher on average over 100 consecutive landing attempts.

Remarks. The total maximum reward attainable is about 260 per episode. Even sometimes, 310+ reward could be reached.

Difficulty: The LunarLander-v2 continuous state must adapt in real-time the changes in the shape of the landing surface every time. The lander agent must learn to land in all situations.

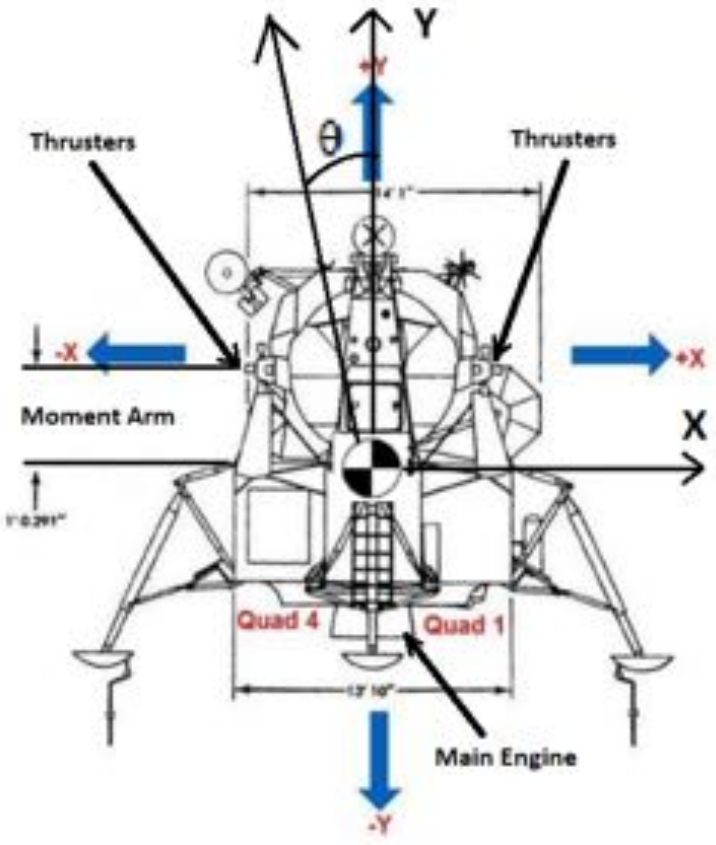

Figure 2-1: Eagle lunar lander module (Meen, 2020).

2.3. Reinforcement Learning Methods

Reinforcement Learning (RL) is an important method for solving the Markov decision process (MDP) problem (Sutton & Barto, 1998). In Reinforcement Learning, agents learn mappings from state environments to actions. Through interaction with the environment, agents obtain reward signals and change behavior selection policies. Therefore, agents can obtain the greatest rewards from the environment and maximize long-term accumulative rewards.

The RL agent interacts with the environment from time to time. At any time t, the agent receives state s_t in state space S and selects action a_t from action space A, based on mapping policy $\pi(a_t|s_t)$. This behavior namely agent behavior is mapping from state s_t to actions a_t, receiving scalar reward r_t by reward function R(s, a), and transitioning to next state s_{t+1} using state transition probability $P(s_{t+1}|\ s_t, a_t)$, following the environment model. Episodically, rewards are given until the agent reaches the terminal state and then this process continues restarts.

$$R_t = \sum_{k=0}^{\infty} \gamma^k r_{t+k} \tag{2-1}$$

is the accumulated reward with the discount factor $\gamma \in (0,1)$. The agent aims to maximize the long-term return expectations of each state. The problem is set in a discrete state and action space. It is not difficult to expand it into continuous spaces (Sutton & Barto, 1998).

2.3.1 Q-Learning

One of the most important breakthroughs in reinforcement learning is the development of the Temporal Differential/TD Off-Policy control algorithm known as Q-Learning (Watkins, 1989). Its simplest form called one-step Q-Learning is defined by:

$$\boldsymbol{Q(S_t, A_t)' = Q(S_t, A_t) + \alpha[R_{t+1} + \gamma\, max._a\, Q(S_{t+1}, A_{t+1}) - Q(S_t, A_t)]} \tag{2-2}$$

with

Q' = *policy value at the current state*

Q = *policy value at the previous state*

R = *reward*

α = *Learning Rate*, $0 < \alpha \leq 1$, specifies the rate measure at which the old value will be replaced by the new value

γ = *Discount rate*, $0 \leq \gamma \leq 1$, determine the value of the reward in the future, the smaller the value, the agent will be more concerned with the immediate rewards, not rewards in the future

$\max_a Q(S_{t+1}, a)$ = the maximum value of the action-value function at state t+1 for an action a.

In the Q-Learning case, the algorithm attempts to learn a state-action value Q (s, a), whose value is the maximum discounted reward that can be achieved by starting in state x, taking an action a, and following the optimal policy π^* thereafter. for each state-action pair, a separate Q(s, a) value exists when the action space is discrete. (Mitić et al., 2011)

The studied action-value function Q, directly approximates the optimal action-value function Q∗, regardless of the policy followed. This simplifies algorithmic analysis and enables early proof of convergence. The policy still affects the determination of which state-action pairs to visit and update. However, all it takes for that true convergence is that all pairs are constantly being updated. As we observed, this is a minimum requirement in the sense of what method is guaranteed to find the optimal behavior in the general case should require it. Under these assumptions and variants of the usual stochastic forecast conditions on the order of the step size parameters, Q has been shown to converge the probability of Q∗ to 1. The Q-learning algorithm is shown in the procedural form in Table 2-1.

Table 2-1: Q-Learning Pseudocode Algorithm

Q-Learning
Initialize Q(s,a) Repeat: Initialize **s** Repeat: Choose a from s using policy derived from Q (e.g., ξ-greedy) Take action a, observe s', r Q(s,a) ← Q (s,a) + α [r + γ $\max_a$ Q(s',a') – Q(s,a)] Q*←Q s ← s' until s is terminal

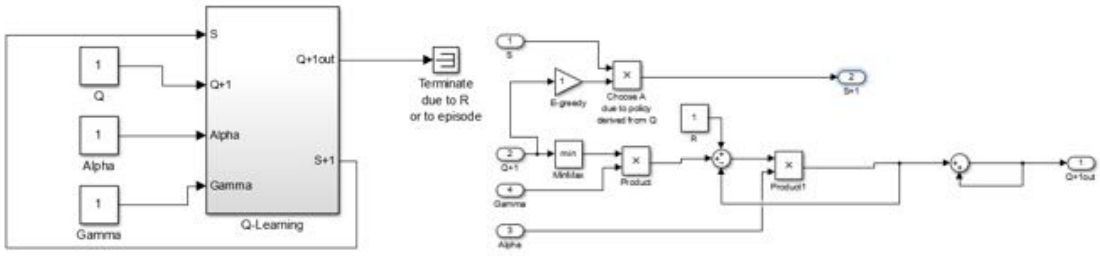

Figure 2-2: Q-Learning control diagram (left) and Bellman equation diagram (right).

2.3.2 Role of Heuristic in Powered Landing Guidance

A heuristic is a rule about the nature of the problem, which is based on a well-known environment model and its purpose is to direct the search towards the goal so that it becomes more efficient. The heuristic function h:(S→R+) given in each state s∈S is an estimate of the distance between the current state and the goal state. The value h(s), the

closer s to the goal state, is getting smaller. If s is in terminal state, then h(s) = 0. Therefore Heuristic is literally Q-Learning in the deterministic environment (Basic & Snajder, 2020).

The heuristic control determines the control force, the control force generates the net force, the net force determines the acceleration, the acceleration gradually adjusts to the speed, and the landing velocity value becomes the collision speed. Therefore, it is not an easy task to manage the collision speed around the desired level. In addition, the heuristics to be used must also set the length of time needed to land at a low enough value because the long landing duration requires extensive fuel use. The two criteria, minimizing the speed of the collision and minimizing the length of time it takes to land, contradict each other, which makes the soft-landing problem a challenging task. The control heuristic, which aims to meet these two criteria, should allow the vehicle to descend to the surface rather quickly, but allow it to slow down safely to a low-speed value before landing (Tanyolaç & Yasarcan, 2012).

2.3.3 Enhancement of Q-Learning

Various achievements have been achieved in the study of RL, and some classical algorithms, such as Q-learning (Watkins, 1989), have been introduced. For MDP problems with small state space and action space, the traditional RL algorithm is an effective solution. However, in most cases where the state space or action space is very large or stochastic, it usually makes traditional RL algorithms slow down or fail to converge to optimal policies. Therefore, the introduction of a neural network and parametrization of the value function or policy function is the main solution to extend the capability of the Q-Learning method.

2.3.3.1 Deep Q-Learning Network (DQN)

Neural Network (NN) is a popular non-linear approach function. The Deep Q-Learning Network was proposed by Mnih et al. in 2015 by combining Q-Learning (QL) and Convolutional Neural Network (Bengio, 2013), which effectively blending the value function of reinforcement learning inside the deep neural networks. Two main approaches of Q-Learning enhancement are utilized, the Deep Q-Learning Network (DQN) and Double Deep Q-Learning Network (DDQN), in which the latter used two multi-layered-NN architecture parallel.

The first significant mechanism is the experience replay mechanism, which utilizes previously used samples or reinforcement learning to solve the solution convergency. In addition to this is the target network, which is used to select and evaluate actions and ensure the computational stability of the NN. DQN is well aware that deep reinforcement learning computation extends to research and application of traditional RL, and makes Deep Reinforcement Learning (DRL) a hotspot of artificial intelligence (Sutton & Barto, 1998).

By continuously updating the neural network DQN skip the Q-table to update the Q value but utilizes the neural network to update the Q value and find the optimal path of action. DQN used two neural networks: target-network to get the value of Q for evaluation, and main-network, which is used to get the value of Q with a relatively fixed parameter. (Quan et al., 2020) The mathematical description of the loss function of DQN is depicted as the Eq. (2-3), θ^{-} is the parameter in the target network

$$\mathrm{L}(\theta) = \mathrm{E}\left\{\left(Q_{target} - Q_{main}(s_t, a_t, \theta)\right)^2\right\} \tag{2-3}$$

$$Q_{target} = r_{t+1} + \gamma \cdot \max_{a_{t+1}} Q_{target}(s_{t+1}, a_{t+1}, \theta^{-}) \tag{2-4}$$

The same value is used to select and measure any action at once by the max operation in standard Q-learning and DQN. Overly optimistic value estimation may be resulted from this approach. However, the DQN paper ignited the interest of the AI community in the field of deep reinforcement learning and lead to several extensions of DQN.

2.3.3.2 Double Deep Q-Learning Network (DDQN)

In this work, DQN's extension namely Double Deep Q-Learning Network will be implemented and benchmarked to other methods to solve a landing spacecraft task as adapted from previous work by (Kersandt, 2018) for UAVs. In order to avoid overly optimistic value estimation that might occur in DQN and standard Q-Learning, DDQN came into being (Hasselt et al., 2016). This overestimation of values is also called

maximization bias, where the maximum operator uses the same values for selecting the best action as well as an estimator for the maximum true values. Overestimation will dampen the convergence to the optimal policy (Sutton & Barto, 1998). Separating the process of selecting the optimal action from the estimation of optimal actions is a simple method to reduce the impact of overestimation as much as possible (Hasselt, 2010). Double DQN contains two networks. The policy network is used to select the action (action with best-predicted Q) in real-time. At intervals, models are stabilized to update the target networks. Changes to Q values may lead to changes in closely related states (i.e. states close to the one we are in at the time) and as the network tries to correct for errors it can become unstable and suddenly lose signficiant performance. Target networks (e.g. to assess Q) are updated only infrequently (or gradually), to avoid instability problem.

The amendment from simple DQN is to decouple training of Q for the current state and target Q derived from the next state which is expressed in the DDQN formula as shown by Eq. (2-5) and (2-6). The basis of improving DQN to DDQN is by separating the targeted Q-value,

$$Q_{target} = r_{t+1} + \gamma Q(s_{t+1}, \max_{a_{t+1}} Q(s_{t+1}, s_{t+1}, \theta); \theta^{-}) \quad (2\text{-}5)$$

where θ^{-} is the parameter in the target network, from the policy-estimated Q-value,

$$Q_{policy} = r_{t+1} + \gamma Q(s_{t+1}, \max_{a_{t+1}} Q(s_{t+1}, s_{t+1}, \theta); \theta) \quad (2\text{-}6)$$

Notice that the selection of the action, in the argmax, is still due to the online weights θ. This means that, as in Q-learning, we are still estimating the value of the greedy policy according to the current values, as defined by θ. However, we use the second set of weights θ^{-} to fairly evaluate the value of this policy. The roles of θ^{-} and θ are switched to update symmetrically the second set of weights.

To get the best action when training, the policy network produces the best-predicted Q, and periodically this Q updates the target network. So, when training, the action is selected using Q values from the policy network, but the policy network is updated to better predict the Q value of that action from the target network. The policy network is instantiated throughout the target network every n steps (e.g. 1000) (Allen, 2021).

3. Implementations and Results

This work is implemented the Lunar Lander problem in 2-Dimensional OpenAI Gym using three methods, Q-Learning or Heuristic, Deep Q-Learning Network, and Double Deep Q-Learning Network.

Lunar Lander Heuristic has a state that has been defined as the output divided into 8, namely horizontal position, vertical position, horizontal velocity, vertical velocity, angle velocity, angular velocity, left leg contact, right leg contact. Sharing in these inputs determines 4 actions, namely do nothing, fire main, fire left, fire right. Thus, the 8 outputs are called state components and the 4 actions are the agent control inputs.

3.1 Results of the Implementation of the Heuristic / Q-Learning on the Lunar Lander

The state components in the 2-D Lunar Lander problem are presented below.

Table 3-1: Heuristic State Components

Output State Components
pos = self.lander.position vel = self.lander.linearVelocity state = [(pos.x - VIEWPORT_W/SCALE/2) /(VIEWPORT_W/SCALE/2), (pos.y - (self.helipad_y+LEG_DOWN/SCALE)) / (VIEWPORT_H/SCALE/2), vel.x*(VIEWPORT_W/SCALE/2)/FPS, vel.y*(VIEWPORT_H/SCALE/2)/FPS, self.lander.angle, 20.0*self.lander.angularVelocity/FPS, 1.0 if self.legs[0].ground_contact else 0.0, 1.0 if self.legs[1].ground_contact else 0.0]

These heuristic functions below map h: S → R+ given in each state s∈S an estimate of the distance between that state and the goal state.

Table 3-2: Heuristic Functions on the Lunar Lander Problem

Reward Shaping Heuristic Functions

#Ten points for legs contact
shaping = \
- 100*np.sqrt(state[0]*state[0] + state[1]*state[1]) \
- 100*np.sqrt(state[2]*state[2] + state[3]*state[3]) \
- 100*abs(state[4]) + 10*state[6] + 10*state[7]
if self.prev_shaping is not None:
reward = shaping - self.prev_shaping
self.prev_shaping = shaping
 	
#Less fuel spent is better, about -30 for heurisic landing
reward -= m_power*0.30
reward -= s_power*0.03
done = False
if self.game_over or abs(state[0]) >= 1.0:
done = True
reward = -100
if not self.lander.awake:
done = True
reward = +10
return np.array(state, dtype=np.float32), reward, done, {}

The results of training from the lunar lander using the PID heuristic method can be seen in the reward value in Figure 3-1.

Figure 3-1: Graph of reward value on Lunar Lander with the heuristic method.

It can be seen that only in 1 episode with 435 steps, reward 200 is reached, this means the Heuristic method could find the solution in just one pass. It could be regarded as a normative behavior due to the deterministic nature of the functions. The introduction of the stochastic part to the functions will be a game-changer though and to be implemented in DQN and DDQN.

This whole research is conducted in Python running on Anaconda Navigator, using a Spyder Editor, and the following results are taken from the Lunar Lander Heuristic or Q-Learning method.

From Table 3-2 above, we can get the plotting of state data for each step as presented in Figures 3-1 to 3-5, so that we could figure out how the flight characteristics' movement of the vehicle is.

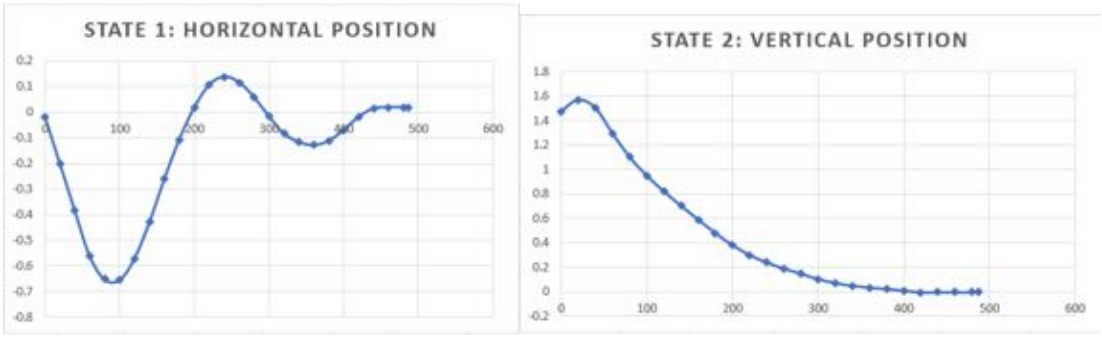

Figure 3-2: Horizontal position (m) as first state, and vertical position (m) as second state.

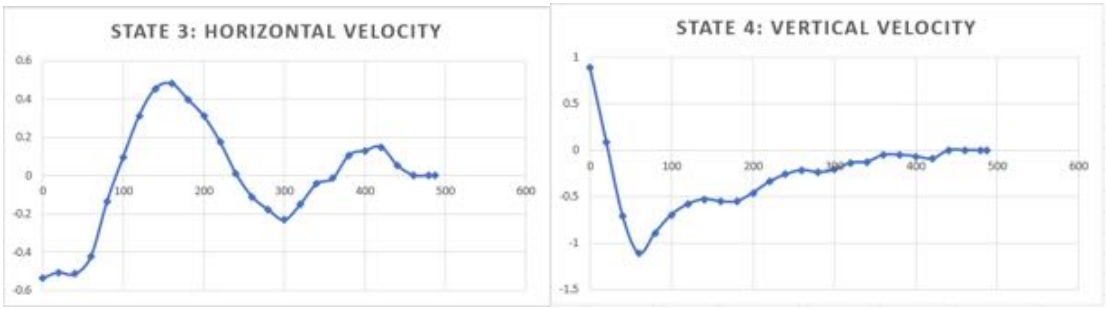

Figure 3-3: Horizontal velocity (m/s) and vertical velocity (m/s) as the third and fourth states.

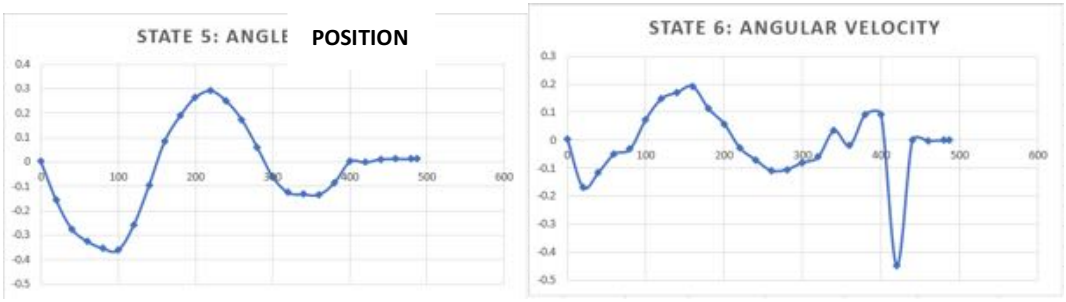

Figure 3-4: Angle position (rad) and angular velocity (rad/s) as the fifth and sixth states.

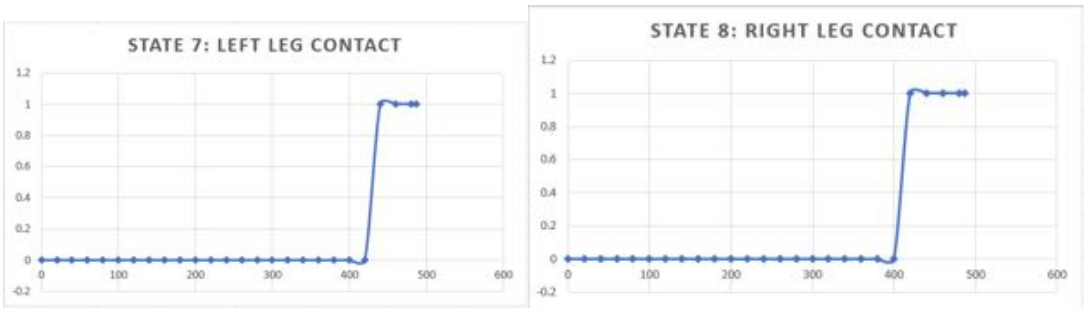

Figure 3-5: Left and right leg contact as seventh and eighth state movements.

Figure 3-6 below plots the three input commands (main engine, side thruster, and pitch controller), accompanied with the acceleration responses of the Lunar Lander, right after given the command. It can be seen that the input commands are in form of pulses.

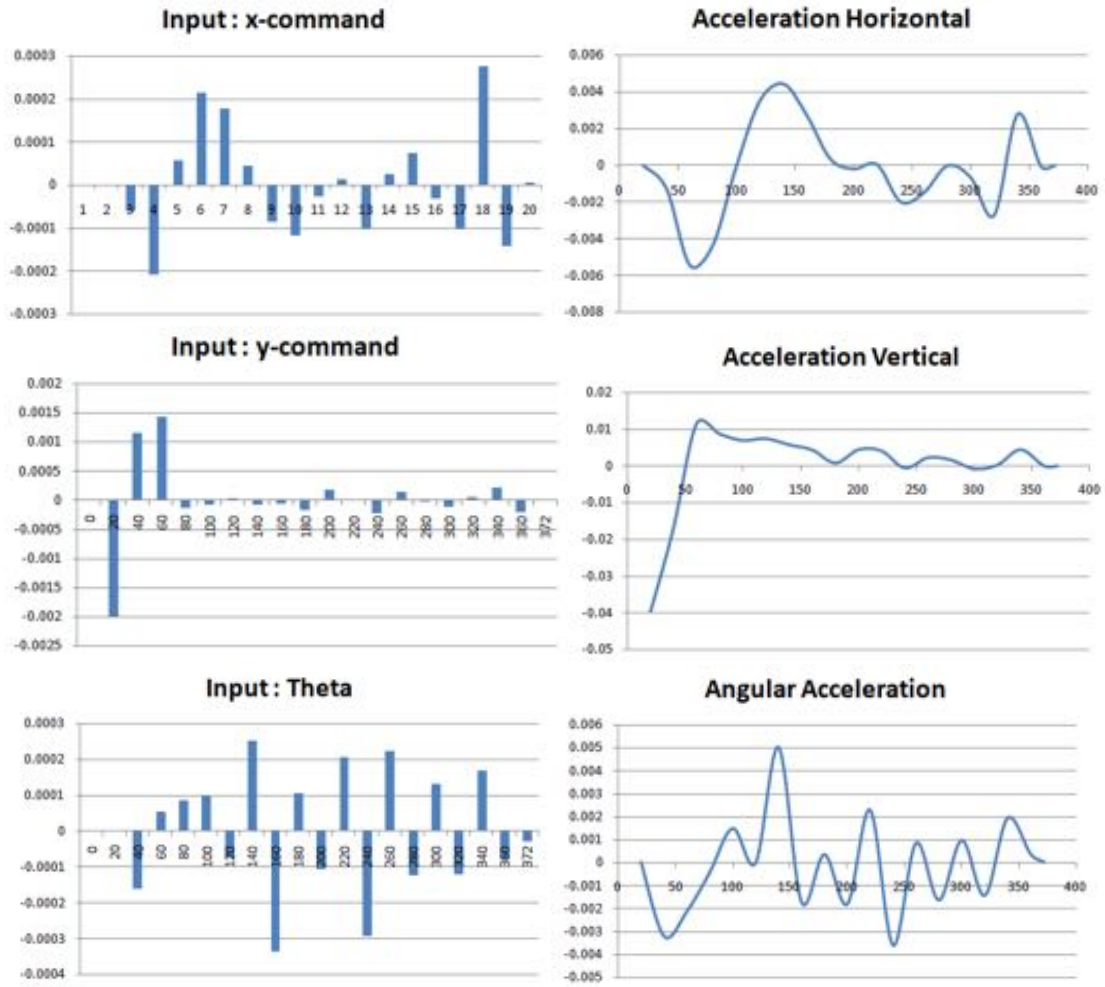

Figure 3-6: Input commands : Side Thrusters (X – N/s^3), Main Thruster (Y – N/s^3), Angular Thrusters (Theta – N/s^3) and Extra States : Horizontal acceleration (m/s^2), Vertical acceleration (m/s^2), Angular acceleration (rad/s^2).

In addition to the whole state components' plots, below is the trajectory result of the Lunar Lander landing scenario trained by the heuristic method.

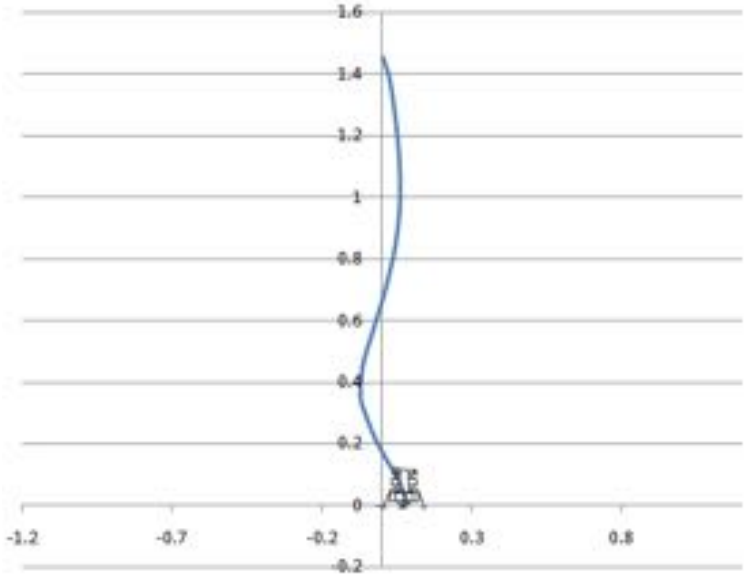

Figure 3-7: A Lunar Lander heuristic landing trajectory (m).

The heuristic or Q-Learning method yields a smooth and efficient landing maneuver. Nevertheless, why the trajectory is not simply a straight vertical line? The initial conditions dictate those undesired flight characteristics: the horizontal motion push to the right 0.6 m/s and the vertical motion pulls upright to 0.8 m/s. These make the Lunar Lander starts in a vertical jumping motion that is eventually corrected by Heuristic Powered Guidance Strategy and gravity force.

3.2 Results of the Implementation of the DQN and DDQN on the Lunar Lander

In the following implementations, the stochastic part plays important role in shaping the rewards due to the existence of the NN policy model and target model.

Table 3-3: Training Parameters in DQN and DDQN

Hyperparameters of DQN	Hyperparameters of DDQN
self.action_space = action_space	self.action_space = action_space
self.state_space = state_space	self.state_space = state_space
self.epsilon = 1.0	self.epsilon = 0.9
self.epsilon_min = 0.01	self.epsilon_min = 0.01
self.epsilon_decay = 0.996	self.epsilon_decay = 0.9993
self.gamma = 0.99	self.gamma = 0.99
self.learning_rate = 0.001	self.learning_rate = 0.0001
self.memory = deque(maxlen=1000000)	self.memory = deque(maxlen=5000)
self.batch_size = 64	self.minibatch_size = 64
self.model = self.build_model()	self.model = self.build_model()
self.target_model = self.build_model()	self.target_model = self.build_model()
	self.epochs = 1000
	self.verbose = 0

In this paper, two hidden layers of the neural network are selected as the structure of the target network and the current network. The number of hidden layer neurons is 64. The number of input and output neurons corresponds to the number of input states and actions, which are 4 and 8, respectively. The activation function is relu. According to the characteristics of relu function, the learning rate is 0.0001. To keep the training process relatively stable, the epoch is set at 1000, which means in 1 episode 1000 steps are done. The control cycle is selected as 10 ms as the cycle of actual vehicles required. In order to improve the generalization control ability of the agent, initial values are initialized in a certain range in every episode. The maximum number of training episodes is 1000. When the cost function (7) of network training is less than 10^{-6} and lasts for a period of time, the training is stopped.

$$cost = \sum_{j=1} \frac{1}{2}(y_j - Q(s_j, a_j; \theta))^2 \tag{3-1}$$

To analyze the training process, the cumulative reward of each episode and the total cumulative cost of training were recorded for analysis as planned in Eq. (2-1). The cumulative reward of each episode can indirectly reflect the change of the agent's control ability in the training process. Since the simulation time is 10 seconds and the control period is 10 milliseconds, the immediate reward is counted up to 1000 times per episode.

To proceed to our next action in the environment, even to move randomly, we do a .predict(). Three float values are shown to map the actions. By using argmax we construct the Q-value table. The updating process of the neural network is done by doing .fit() using that updated Q-value. Those 3 Q-values are fitted to make one updated Q-value. Past DQN models are used for each action, and each model used a regressor to output the Q-values.

DDQN intends to diminish overestimations by omitting the max operation in the target network in action selection and action evaluation. Updating target network periods in DDQN remain as same as DQN by copying the online network. This type of DDQN is considered the most conservative way of upgrading DQN. Besides keeping the DQN algorithm intact, this DDQN is desired to get the most benefit of Double Q-learning with the least computation.

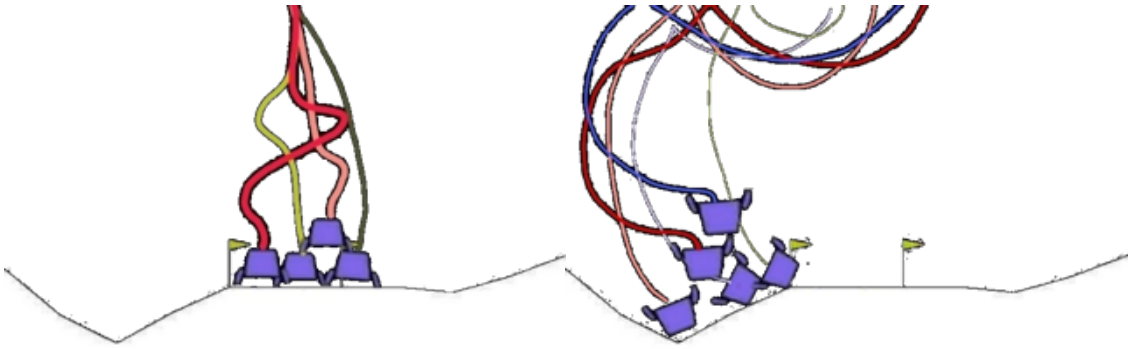

Figure 3-8: Lunar Lander' DQN (left) last 4 episodes landing and DDQN (right) la st 5 episodes landing.

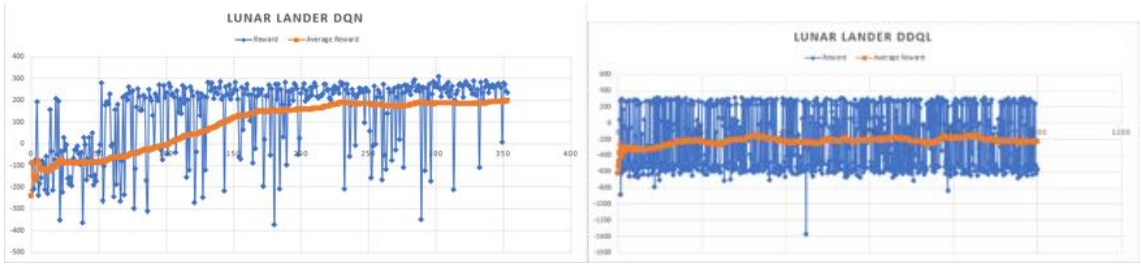

Figure 3-9: Reward gained from LL DQN (left) and LL DDQN (right) network training.

From the two figures above, the DQN method provided a convergent solution, while the DDQN failed to do so. This huge discrepancy could be explained as the result of a different strategy to approach the problem of estimation to the action values which leads to such contrasting loss values. Loss values are formulated in Eq. (2-3) which is affected dominantly by the subtraction of Q-target values and Q-realtime values, as shown in Eq. (2-4). In DQN the Q-target values follow Eq. (2-4) which are taken from max Q_t(s, a), while in DDQN, those values are computed using Eq. (2-5) which are taken from Q without max. The subtraction term is visualized in Figure 3-10.

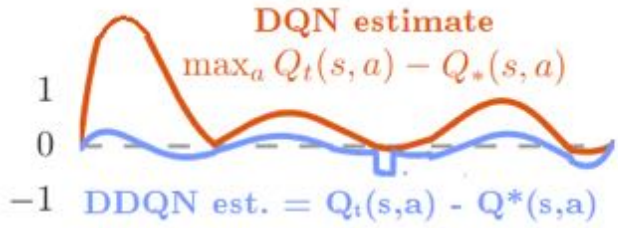

Figure 3-10: Difference in action values estimator between DQN and DDQN.

The smaller magnitude of estimation does not necessarily mean a lower degree of error or bias, on the other side, this could dampen the correcting process of action's values depending on the case. The DQN estimator could be considered overestimate, but eventually, in our case, it helps to increase training reward significantly as shown in Figure 3-9. In contrast, the DDQN training rewards couldn't go beyond negative, which explained the cause the DDQN Lunar Lander never touchdowned.

After conducting training on the Heuristic/Q-Learning, DQN, and DDQN methods, the following is a table of comparison of the training results for each method in the lunar lander.

Table 3-4: Comparison of Lunar Lander Training Results

Landing Guidance Method	Condition	Stochastic / Neural Network	Agent's Training Steps	Average Reward	Training Time	Solution Found Rate	Average Miss Distance (m)
Heuristic Search/Q-Learning	Known Environment, Known Agent, Computed Input State	No	487	117	52 sec.	95%	0.15
Deep Q-Learning Network	Unknown Environment, Known Agent, Estimated Input State	Yes	171911	86	63 min.	50%	0.2
Double Deep Q-Learning Network	Unknown Environment, Known Agent, Estimated Input State	Yes	487000	-228	70 min.	0%	Fail

4. Conclusions

From the three Lunar Lander experiments conducted, it can be analyzed that the performances of Lunar Lander's movement relate directly to the method's capability to reach a solution. Looking at a glance, the heuristic method showed an efficient method, with a very fast training time and a fairly large average reward. The heuristic movements are fairly smooth and the landing reward is never negative. The DQN method in the Lunar Lander case has a fairly good quality following the heuristic one. However, this will also vary, because the initial random factor also affects the movement of the Lunar Lander. DQN has spent quite a bit of computation on neural networks, including using experience replay and the target network. On the other hand, DDQN in the Lunar Lander case is strongly discouraged because the average reward obtained is never positive, thus still far from convergency. The proposed method of separating usage of online weight θ in the action selection process and action evaluation process in order to reduce overestimation didn't produce results as intended. Apparently, in our case, overestimation is needed to correct the negative reward. The only advantage of DDQN is its ability to produce quite diverse movements of the Lunar Lander that could be very different from the start of training, which suggests its ability to absorb more uncertainty in the environment. DDQN as an extension of DQN needs examination further in terms of hyperparameter adjustment to produce better Lunar Lander actions.

Acknowledgments

The authors would like to express gratitude to LAPAN Pustekroket, Politeknik Elektronika Negeri Surabaya (PENS), University of Adelaide, Australia, and Universitas Indonesia for their support in this research.

Contributorship Statement

LN is the main contributor of this research by developing the concept and preparing the manuscript, NRZ and NQ conduct the simulations, RAk and RAn proofread the writing, analyze the results and suggest improvements, SKW is the corresponding author and guides the whole process of research.

References

Allen, M. (2021). Double Deep Q Network (DDQN) – controlling a simple hospital bed system. Retrieved from https://pythonhealthcare.org/2020/07/05/double-deep-q-network-ddqn-controlling-a-simple-hospital-bed-system/

Bašić, B. D. & Šnajder, J. (2020). Unit 3: Heuristic search [PowerPoint slides]. Faculty of Electrical Engineering and Computing, University of Zagreb. https://www.fer.unizg.hr/_download/repository/AI-3-HeuristicSearch.pdf

Bengio, Y. (2013). Deep learning of representations: Looking forward. https://arxiv.org/pdf/1305.0445.pdf

Brockman, G., Cheung, V., Pettersson, L., Schneider, J., Schulman, J., Tang, J., & Zaremba, W. (2016). *OpenAI gym*. http://arxiv.org/abs/1606.01540

Cini, A., Eramo, C. D., Peters, J., & Alippi, C. (2020). Deep reinforcement learning with weighted Q-Learning. https://arxiv.org/pdf/2003.09280.pdf

Ermacora, G., Rosa, S., & Toma, A. (2016). Fly4SmartCity : A cloud robotics service for smart city applications. *Journal of Ambient Intelligence and Smart Environments*, *8*(3), 347–358. https://doi.org/10.3233/AIS-160374

Gaudet, B., Linares, R., & Furfaro, R. (2018). Integrated guidance and control for pinpoint Mars landing using reinforcement learning. *Advances in the Astronautical Sciences, 167,* 3135-3154.

Hasselt, H. van. (2010). Double Q-learning. *Advances in Neural Information Processing Systems, 2010,* 2613-2621.

Hasselt, H. van., Guez, A., & Silver, D. (2016). Deep reinforcement learning with double Q-learning. *Proceedings of the AAAI Conference on Artificial Intelligence, 30*(1).

Kersandt, K. (2018). Deep reinforcement learning as control method for autonomous UAVs [Master's thesis, Universitat Politecnica de Catalunya]. https://upcommons.upc.edu/handle/2117/113948

Klumpp, A. R. (1974). Apollo lunar descent guidance. *Automatica*, *10*(2), 133–146. https://doi.org/10.1016/0005-1098(74)90019-3

Latyshev, K., Garzaniti, N., Golkar, A., & Crawley, E. F. (2021). Technology roadmap for future human landing systems. Conference proceedings of ASCEND 2020. https://doi.org/10.2514/6.2020-4229

Meen, V. (n.d.). Modelling the 1/32 lunar module [Image]. Retrieved from http://spacemodels.nuxit.net/1-32 LM/Orientation1.jpg

Mitić, M., Miljković, Z., & Babić, B. (2011). Empirical Control System Development for Intelligent Mobile Robot Based on the Elements of the Reinforcement Machine Learning and Axiomatic Design Theory. *FME Transactions (2011)*39, 1-8.

Mnih, V., Kavukcuoglu, K., Silver, D., Rusu, A. A., Veness, J., Bellemare, M. G., Graves, A., Riedmiller, M., Fidjeland, A. K., Ostrovski, G., Petersen, S., Beattie, C., Sadik, A., Antonoglou, I., King, H., Kumaran, D., Wierstra, D., Legg, S., & Hassabis, D. (2015). Human-level control through deep reinforcement learning. *Nature*, *518*(7540), 529–533. https://doi.org/10.1038/nature14236

Quan, H., Li, Y., & Zhang, Y. (2020). A novel mobile robot navigation method based on deep reinforcement learning. *International Journal of Advanced Robotic Systems 17*(3), 1–11. https://doi.org/10.1177/1729881420921672

Sutton, R. & Barto, A. (1998). Reinforcement Learning: An Introduction. *MIT Press Cambridge: London, UK*.

Tanyolaç, T. & Yasarcan, H. (2012). Control heuristics for soft landing problem. Conference proceedings of the 30th International Conference of the System Dynamics Society.

Von Dollen, D. (2017). Investigating reinforcement learning agents for continuous state space environments (pp. 5–7). http://arxiv.org/abs/1708.02378

Watkins, C. (1989). Learning from delayed rewards [Doctoral dissertation, King's College (University of Cambridge)].

Yu, X. (2019). Deep Q-learning on lunar lander game. Retrieved from https://www.researchgate.net/publication/333145451_Deep_Q-Learning_on_Lunar_Lander_Game

Station-Keeping Simulation and Planning for LAPAN-A4 Satellite Using Finite-Burn Thruster

Muhammad Rizki Zuhri[1], Ridanto Eko Poetro [1]

[1,]Faculty of Mechanical and Aerospace Engineering, Bandung Institute of Technology

e-mail: muhammadrizkizuhri@gmail.com

Received: 02-11-2020. Accepted: 19-03-2021. Published: 30-06-2021

Abstract

To be a Sun-synchronous orbit (SSO), the orbit must have a certain value of nodal precession rate, which equals 360°/year. However, the value of nodal precession rate is usually drifted by orbit perturbations, mainly by the oblateness of the Earth and atmospheric drag, to be no longer 360°/year as expected for SSO. Thus, the local time of the satellite will change too, so it needs to be corrected by some correction maneuvers. In this research, the authors studied station-keeping planning for SSO satellite via inclination correction maneuver by simulation using GMAT, a software developed by NASA, with a finite-burn propulsion approach. In this research, LAPAN-A4 satellite is chosen to be the satellite that will be simulated. Some alternative plans of inclination correction maneuver based on maneuvering intervals are chosen, they are maneuvers for every 2 months, 4 months, 6 months, 12 months, and 24 months. The simulation results show that the station keeping planning with correction maneuver for every 2 months is recommended. This alternative gives the lowest fuel consumption so that the fuel and launch cost will be minimum, and the local time drift that is still may be tolerated.

Keywords*: LAPAN-A4; SSO; inclination maneuver; finite-burn thruster*

1. Introduction

Sun-synchronous orbit (SSO) is an orbit that allows the satellite to pass over the same point of the Earth's surface at the same instant of the true solar time (Kuznetsov & Jasim, 2016). Figure 1-1 illustrates a Sun-synchronous orbit over a year. As depicted in the figure, the satellite would pass over certain regions on the Earth at the same local time every day, 22.30 in this case. This will give advantages for imager satellites as the images taken would have the same proportion of lighting from the Sun.

To achieve this, i.e. the same local time every day, the orbit needs to precess at the same pace that the Earth revolves around the sun (Llop et al. 2015), or equals to 360°/year. This precession is called nodal precession rate as the orbit precession is indicated by the precession of its nodes. This nodal precession rate is affected by some orbital elements, those are eccentricity (*e*), semi major-axis (*a*), and inclination (*i*) (Kuznetsov & Jasim, 2016).

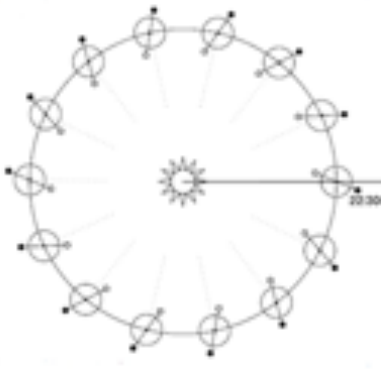

Figure 1-1: Sun-synchronous orbit (Capderou, 2005).

The nodal precession rate could be approximated by the effect of J_2 perturbation. The nodal precession rate caused by the Earth's zonal harmonic coefficient (J_2) is expressed by equations below (Utama, Saifudin, & Mukhayadi, 2018):

$$\dot{\Omega} = -\frac{3}{2} n J_2 \left(\frac{R_e}{p} \right)^2 \cos i \tag{1-1}$$

$$n = \sqrt{\frac{\mu}{a^3}} \tag{1-2}$$

$$p = a(1-e^2) \tag{1-3}$$

where $R_e = 6378\,km$ is the Earth's equatorial radius, n is mean anomaly, and $\mu = 3.986{\times}10^5\ km^3 s^{-2}$ is the Earth's standard gravitational parameter.

SSO satellites are mostly also LEO satellites (Macdonald et al., 2010), hence the orbit perturbation caused by the oblateness of Earth's shape and atmospheric drag will be greater. These perturbations will lead to the changes of some orbital parameters value. Consequently, the value of nodal precession rate may change too, so its value will be no longer 360°/year as would be expected for SSO.

Indonesian aerospace agency, LAPAN, has three satellites currently in orbit (Utama, Hakim, & Mukhayadi, 2019). Two of the satellites are SSO, they are LAPAN-TUBSAT (Triharjanto et al., 2004) and LAPAN-A3 (Hasbi & Suhermanto, 2013). After years in orbit, LAPAN-TUBSAT and LAPAN-A3 show drifted orbit (Utama et al., 2018). Figures 1-2, 1-3, and 1-4 respectively show the time history of LAPAN-A3 orbital parameters; semi major-axis, eccentricity, and inclination. There are drifts on those orbital parameters over time which could be an indication that the nodal precession rate value may be no longer 360°/year or, in other words, its orbit is no longer Sun-synchronous since the local time will be drifted. Figure 1-5 shows the local time drift that occurred on LAPAN-TUBSAT.

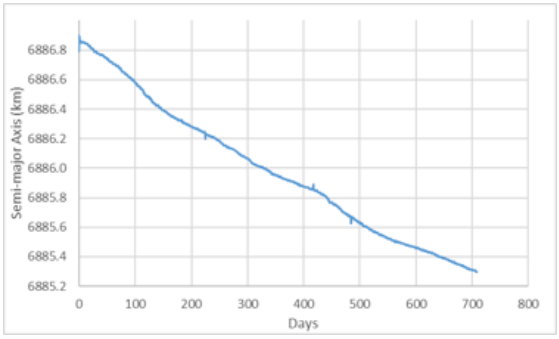

Figure 1-2: Semi-major axis drift of LAPAN-A3.

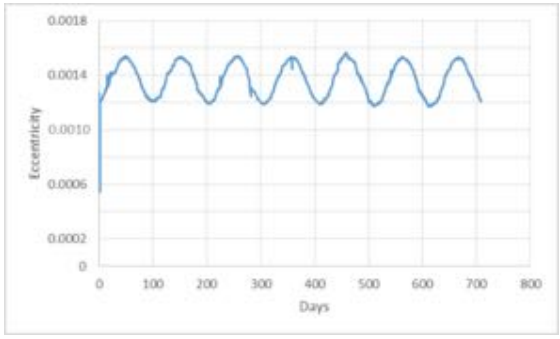

Figure 1-3: Eccentricity drift of LAPAN-A3.

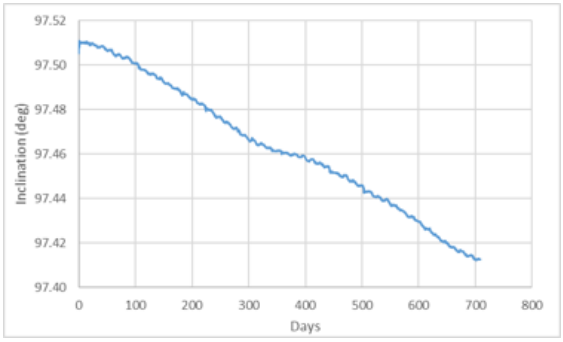

Figure 1-4: Inclination drift of LAPAN-A3.

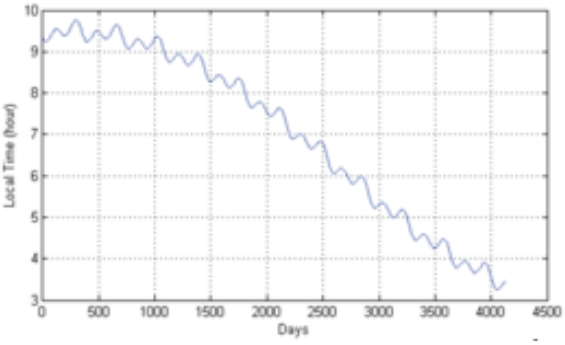

Figure 1-5: Local time drift of LAPAN-TUBSAT (Utama et al., 2018).

To deal with this problem, a certain method of correction maneuver needs to be carried out so that the nodal precession rate value remains at the desired value of 360°/year. According to Eq. (1-1), inclination, eccentricity, or semi-major axis changes would lead to the changes in the nodal precession rate value. Hence, those three are the possible maneuvers available to maintain the desired value of the nodal precession rate. However, as depicted in Figure 1-3, the time history of eccentricity is only sinusoidal with more or less a constant mean value. Moreover, the inclination maneuver is more effective to change the nodal precession rate value compared to the semi-major axis maneuver with the same ΔV applied (Zuhri, 2020).

LAPAN is planning to launch another SSO satellite, LAPAN-A4, in 2021 (Jemadu, 2020) with an expected local time of about 9.30 p.m. (Saifudin, Karim, & Mujtahid, 2018). This satellite is designed to have a propulsion system in order to carry out correction maneuvers including correction maneuvers to maintain the desired nodal precession rate as explained before. In this research, the authors schedule and simulate several alternative plans of station-keeping planning for the LAPAN-A4 satellite via inclination maneuver in the finite burn thruster approach by using GMAT (The GMAT Development Team, 2012), an open-source trajectory design and optimization software developed by NASA and private industry. A finite burn approach is adopted since it represents how thruster actually works, and GMAT is chosen because it is one of the best tested NASA's open-source software for space mission analysis (Hughes et al., 2014). The result and performance of the alternative plans will be compared, and a recommended alternative plan would be chosen to be a station-keeping planning recommendation for the LAPAN-A4 satellite.

2. Methodology

As mentioned before, this research focuses on a station-keeping simulation for the LAPAN-A4 satellite. The station-keeping planning was selected based on maneuvering intervals via inclination correction. The simulation was conducted using GMAT with a finite burn thruster approach.

2.1. Satellite Data

Satellite data used for this research is the proposed design of the LAPAN-A4 satellite. Table 2-1 shows the main characteristics of the LAPAN-A4 satellite.

Table 2-1: LAPAN-A4 Main Characteristics (Saifudin et al., 2018)

Data	Value
Dry mass (kg)	150
Dimension (mm×mm×mm)	744×700×520
Altitude (km)	500
Inclination (deg)	97.38[a]

[a]Decimal values are assumed to provide $\frac{d\Omega}{dt} = 360°/year$

LAPAN-A4 satellite is designed to have a propulsion system to support correction maneuvers in orbit. The thruster used in this satellite is 1 N HPGP (High-Performance Green Propulsion) (Utama et al., 2018), a thruster fueled by LMP-103S with blow-down operation mode developed by ECAPS. The data of this thruster is provided in Table 2-2. However, in this simulation, the satellite is assumed to carry fuel with maximum capacity.

Table 2-2: Thruster Data (Anflo & Möllerberg, 2009)

Data	Value
Tank Capacity (L)	4.5
Thrust (N)	1
Feed Pressure (MPa)	2.2
Blow-down ratio	4:1

2.2. Maneuver and Simulation Scenario

Alternative plans for station-keeping are scheduled to be based on maneuvering intervals. By assuming that the LAPAN-A4 satellite has 5 years of operation time, the alternative plans are:

1. Inclination maneuver for every 2 months.
2. Inclination maneuver for every 4 months.
3. Inclination maneuver for every 6 months.
4. Inclination maneuver for every 12 months.
5. Inclination maneuver for every 24 months.

Maneuvering targets are obtained by analyzing the $d\Omega/dt$ graph of no-maneuver simulation based on Eq. (1-1) (Figure 2-1). Since the value of $d\Omega/dt$ is oscillating over time, it would be useful to take a polynomial regression as shown by the red line of Figure 2-1. The regression yields the equation as a function of days below:

$$\frac{d\Omega}{dt}(°/year) = 360 + 5.636\times10^{-3}(days) + 8.619\times10^{-7}(days)^2 \quad (2\text{-}1)$$

The desired value of $d\Omega/dt$ is 360°/year. Hence, the deviation of $d\Omega/dt$ from the desired value ($\Delta\dot{\Omega}$) in the function of days is:

$$\Delta\dot{\Omega}(°/year) = 5.636\times10^{-3}(days) + 8.619\times10^{-7}(days)^2 \quad (2\text{-}2)$$

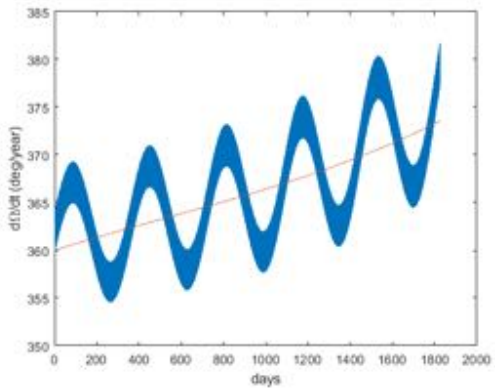

Figure 2-1: $\dot{\Omega}$ graph of no-maneuver simulation.

Computing the value of $\Delta\dot{\Omega}$ for every maneuvering intervals (i.e. 2 months, 4 months, 6 months, etc.), then we will come up to the required $\Delta\dot{\Omega}$ to be achieved by applying inclination maneuver for every alternative plan for each maneuver applied as provided by Table 2-3.

Table 2-3: The Required $\Delta\dot{\Omega}$ Correction Data

Maneuver intervals (Months)	Required $\Delta\dot{\Omega}$ correction (°/year)
2	0.34126
4	0.68873
6	1.04241
12	2.14066
24	4.50472

Since the simulation is using a finite-burn approach, the burning time of the maneuver will be significant. In the simulation, the required burning time to achieve $\Delta\dot{\Omega}$ requirement for each maneuver will be iterated along with orbit propagation. The error target of the iteration is set to be less than 0.001°/year.

Figure 2-2 shows the flowchart of the simulation built in GMAT. The mission is modeled to be a *while* loop with 5 years of operation constraint. While the propagation is still below 5 years of the operation, the satellite would be propagated for X days, with X is representing the alternative plan simulated (e.g. X = 60 for 2 months alternative plan). After that, the satellite is propagated to the node as an inclination-only maneuver must

occur at this point (Vallado & McClain, 2013). At this point, it is still not clear whether the satellite is at ascending node or descending node. In contrast, for uniformity, the satellite is set to apply the maneuver at ascending node. Therefore, a conditional statement is needed to ensure that the satellite will be around ascending node before the inclination maneuver is applied.

After the conditional statement, the value of burning time (bt) is iterated with an initial guess to be 0 s. Furthermore, if before conditional statement the satellite is at descending node, it will be propagated for $t = \frac{P}{2} - \frac{bt}{2}$ as represented by the white trajectory in Figure 2-3, where P is the orbit period. If before conditional statement the satellite is at ascending node, it will be propagated for $t = P - \frac{bt}{2}$ as represented by the white trajectory in Figure 2-4. This propagation is intended to ensure that the burning time of the inclination to be equally divided between above and below the ascending node as represented by the brown trajectory in Figure 2-3 and Figure 2-4.

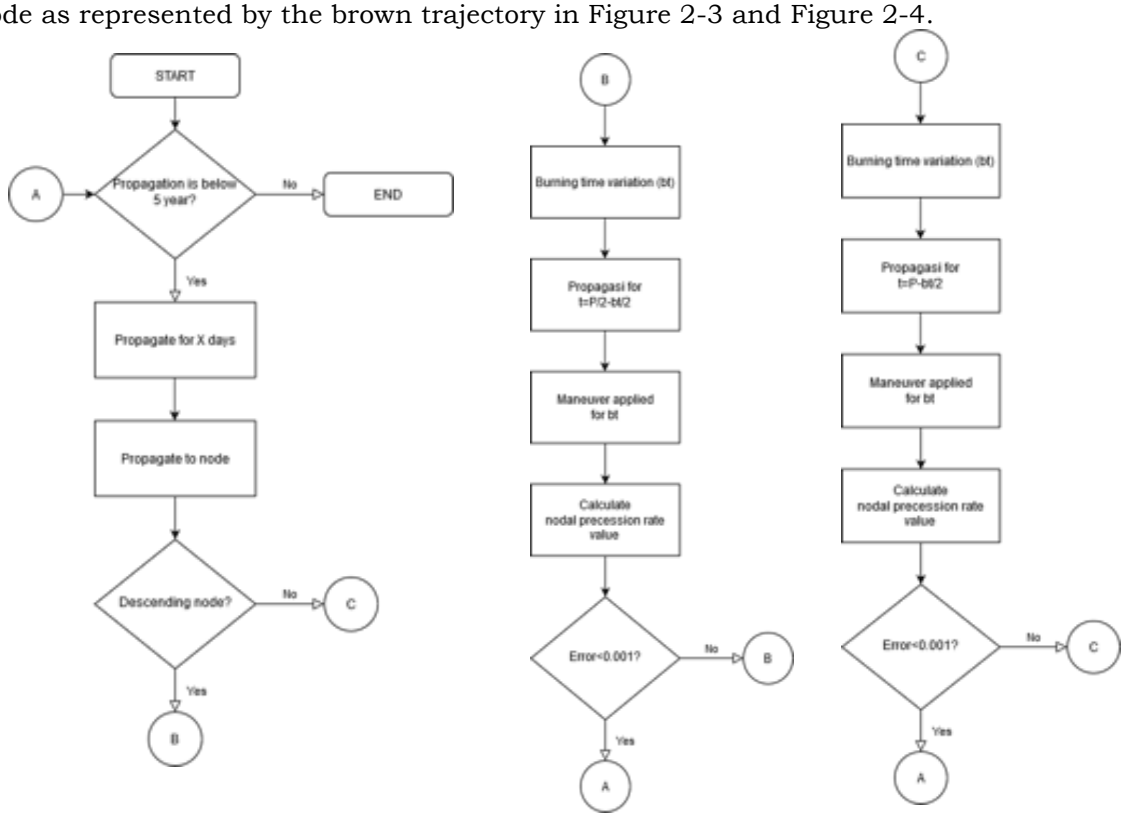

Figure 2-2: Simulation flowchart.

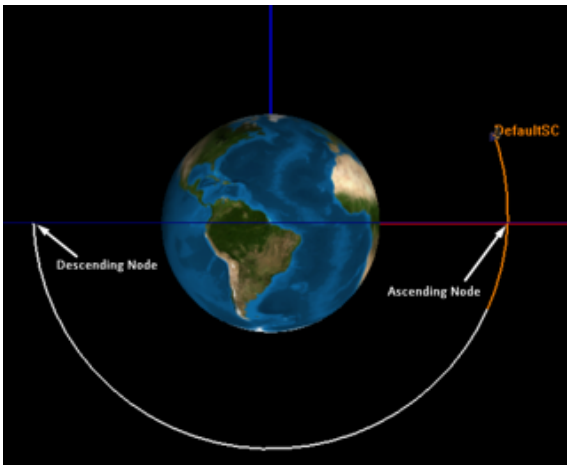

Figure 2-3: Trajectory if the satellite is at descending node before the conditional statement.

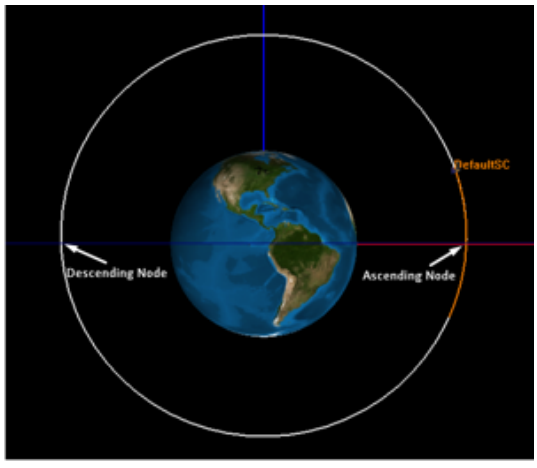

Figure 2-4: Trajectory if the satellite is at ascending node before the conditional statement.

Afterward, the inclination correction maneuver is applied for *bt*. The maneuver is directed perpendicular to the orbit where the maneuver inclination best performed (Ruggiero et al., 2011). The real value of $\Delta\dot{\Omega}$ after the maneuver applied is subsequently calculated and compared to the desired value of $\Delta\dot{\Omega}$. If the error is still beyond the desired error range, i.e. 0.001, the process will be repeated to iterate the value of burning time (*bt*) automatically in GMAT using the Newton-Raphson Algorithm. If the error is within the desired error range, the simulation will be repeated to propagate for X days. These processes repeat until the propagation has gone for 5 years of operation.

3. Result and Analysis

The $d\Omega/dt$ graph is oscillating as indicated by Figure 2-1. So, the same approach will be used for the resulting $d\Omega/dt$ graph of alternative maneuver plans, i.e. taking a second-order polynomial regression. Figure 3-1 shows the comparison of the regressed $d\Omega/dt$ graph for every alternative maneuver plan along with the no-maneuver simulation. Compared to the no-maneuver simulation, all of the alternative maneuver plans successfully lower the trend to be close to the desired value of 360°/year instead of increasing all the time. Notice that the longer the maneuver intervals, the closer the graph to the no-maneuver graph. Longer maneuver intervals mean the $d\Omega/dt$ value is left increasing during a longer time that leads to alternative maneuver plans with longer intervals to have a steeper graph.

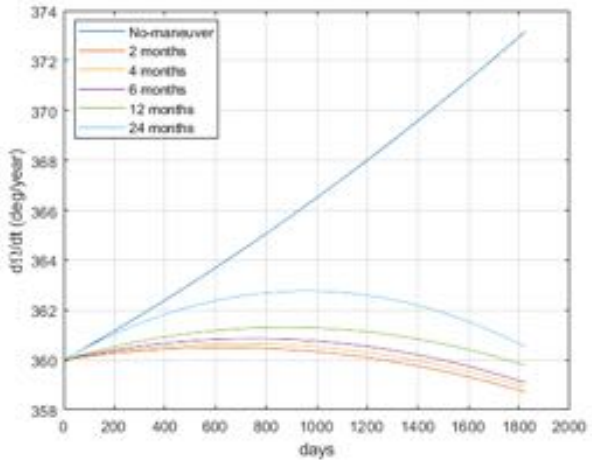

Figure 3-1: Regressed $d\Omega/dt$ graph comparison.

Moreover, if we look closely, the value of $d\Omega/dt$ goes below the desired value of 360°/year. This could happen because of the assumption used for the required $\Delta\dot{\Omega}$ correction. It is assumed that all of the required $\Delta\dot{\Omega}$ correction provided in Table 2-3 is not changing. In fact, the required $\Delta\dot{\Omega}$ is changing after each maneuver, the required $\Delta\dot{\Omega}$ for the first maneuver of the 2-month alternative plan might differ from the second or third maneuver for example. This assumption is used because regression is needed to calculate the required $\Delta\dot{\Omega}$ before maneuver applied. However, the $d\Omega/dt$ value oscillates with a considerably high period (approximately 1 year). For alternative maneuver planning with a short interval, the data for regression becomes unrepresentative as the maneuver interval is shorter than 1 year.

Furthermore, Figure 3-2 provides the comparison of the local time drift for all of the alternative maneuver plans along with the no-maneuver simulation. The local time drift is calculated by computing the difference between the time-history value of actual RAAN (Ω) obtained from GMAT and the time-history value of RAAN should be for SSO. The same as the $d\Omega/dt$ graph depicted by Figure 3-1, the local time drift for alternative maneuver plans with longer intervals is closer to the no-maneuver local time drift. There are also excesses where the local time drift goes to negative values as a consequence of the value of $d\Omega/dt$ which goes below 360°/year. However, all of the alternative maneuver plans give considerably small local time drift results. The largest local time drift occurs on the 24-month maneuver plan with ~24.5 minutes drift, while the smallest occurs on the 12-month maneuver plan with ~3.5 minutes drift only (see Table 3-1).

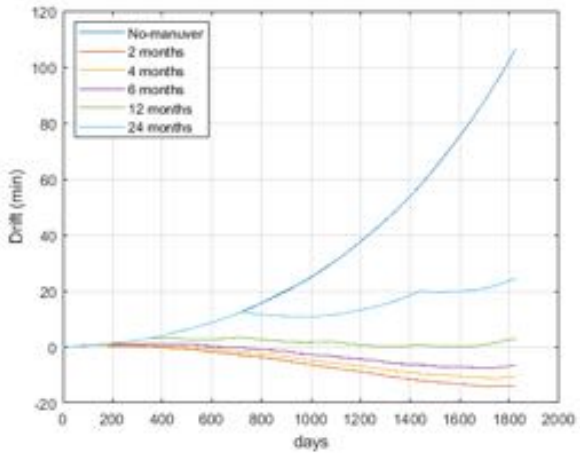

Figure 3-2: Local time drift comparison.

Table 3-1: Maximum Local Time Drift

Maneuver intervals (Months)	Maximum local time drift (minutes)
2	14.2
4	11.1
6	7.6
12	3.5
24	24.5

The local time drift would affect the image quality produced by LAPAN-A4 since the sunlight proportion of the images would be different. Also, this local time drift would affect the work hours of LAPAN employees. The bigger the local time drift, the bigger the issue to the quality of the produced images and LAPAN daily scheduling on LAPAN-A4 tracking. But, as the maximum local time drift resulted after the correction maneuver is in a few minutes range only, the local time drift should not too much disrupt the image quality and work hours of LAPAN employees, especially on LAPAN-A4 tracking.

Besides analyzing the local time drift, it also useful to analyze the burning time and the required fuel for each alternative maneuver plan. Figure 3-3 until 3-7 and Table 3-2 provides the burning time and the required fuel data for each alternative maneuver plan respectively. Alternative maneuver plan with shorter maneuvering interval gives less required fuel as accumulative effects from orbit perturbations are less. So, the required burning time for the maneuver is less too. Because of the less required burning time, the maneuver applied will be closer to the node, which leads to a more effective inclination maneuver as the inclination maneuver performs best at the nodes. As consequence, the required fuel obtained from the GMAT result is less for an alternative maneuver with a short interval.

The burning time graphs provided show decreasing trends. The decreasing trend of burning time is caused by the fact that the mass of the satellite is decreasing over maneuvers as fuel is consumed. Since the mass is decreasing, the maneuver could be performed 'easier' than the previous maneuver, and consequently, the required burning time is less. However, the decreasing trends are not always decreasing. There are fluctuations since the maneuvers also depend on the current value of orbital elements when the maneuver is applied.

Table 3-2: Total Required Fuel

Maneuver intervals (Months)	Required fuel (kg)
2	1.889
4	1.902
6	1.944
12	2.090
24	2.521

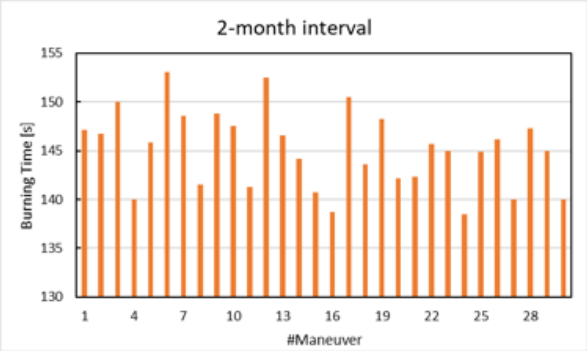

Figure 3-3: Burning times of 2-month interval maneuver.

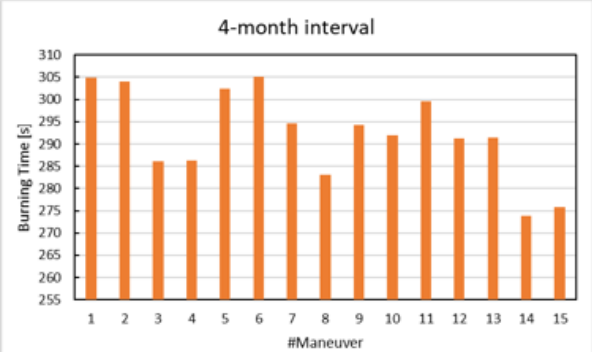

Figure 3-4: Burning times of 4-month interval maneuver.

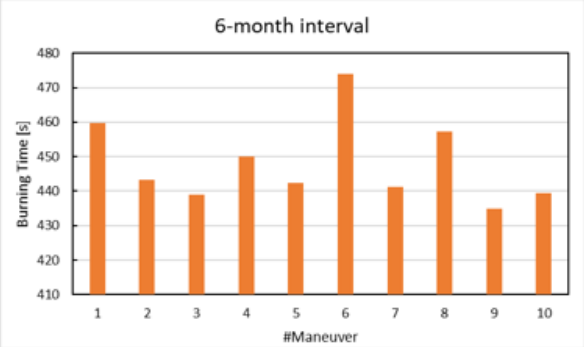

Figure 3-5: Burning times of 6-month interval maneuver.

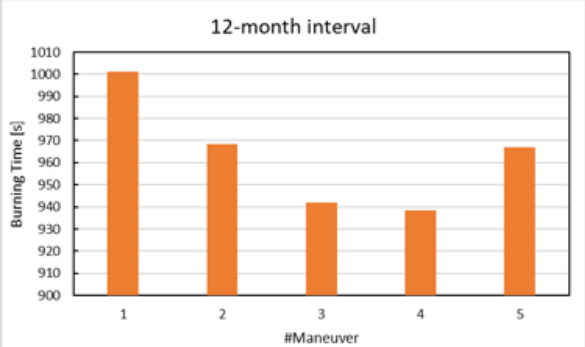

Figure 3-6: Burning times of 12-month interval maneuver.

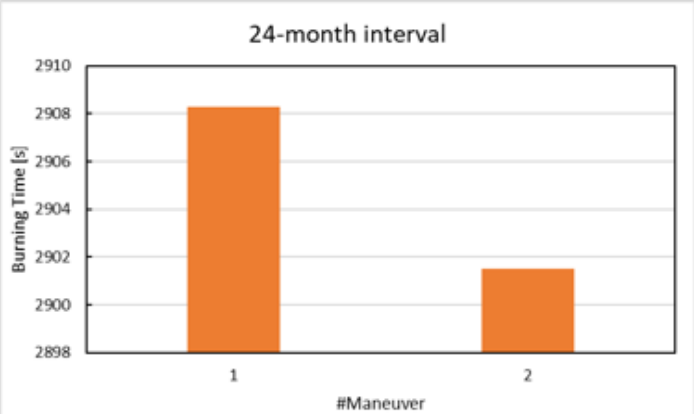

Figure 3-7: Burning times of 24-month interval maneuver.

The required fuels provided in Table 3-2 are the 'worst case' required fuel as the maneuvers are excessive for some alternative maneuver plans ($d\Omega/dt$ becomes lower than 360°/year). If the maneuvers are not excessive, the required fuel will be less. Moreover, in the simulation, the satellite is set to carry fuel with maximum tank capacity as stated in Section 2.1. As the required fuel is less than maximum tank capacity, the satellite could carry less fuel and the maneuver applied would be more effective. In conclusion, the actual required fuel will be less than the required fuel yielded by the simulation.

If we assume that the cost of thruster fuel, LMP-103s, to be 5000 USD/kg, the fuel cost for every alternative maneuver plan is as depicted in Table 3-3. The 2-month maneuver plan gives minimum required fuel compared to other maneuver plans. This alternative maneuver plan is $\frac{3}{4}$ times cheaper than the 24-month maneuver plan which gives the most expensive fuel cost.

Table 3-3: Required Fuel Cost

Maneuver intervals (Months)	Cost (USD)
2	9,445
4	9,501
6	9,720
12	10,450
24	12.605

More fuel to be carried means that the satellite will be heavier. This will affect to launch cost of the satellite. LAPAN-A4 launching will be a secondary payload of CARTOSAT launching from India via PSLV in which the cost depends on satellite mass. Therefore, more fuel to be carried means that the launch cost will be more expensive, especially the launch cost of previous LAPAN satellites are around 15% of the total cost (Paskalis, 2015).

By some considerations, the authors recommend the 2-month maneuver plan to be recommended maneuver plan compared to others. The main consideration is that this maneuver plan gives the cheapest cost either for fuel or launching. This maneuver plan indeed gives a disadvantage as the local time drift resulted is not the smallest. However, as mentioned before, the local time drift resulted is arguably tolerable.

Nevertheless, the 2-month maneuver plan is still not the best compared to all possible maneuver plans. If we watch carefully, the shorter the maneuver interval, the smaller the fuel required. So, maneuver plans with shorter maneuver interval (e.g. 1 month, 20 days, etc.) may give less required fuel and, along with arguably tolerable local time drift, be more optimum than the 2-month maneuver plan. However, in this research, the authors only analyze and choose a recommended maneuver plan from the selected alternatives (i.e. 2-month, 4-month, 6-month, 12-month, and 24-month maneuver plan). Hopefully, further research will be conducted to analyze the most optimum maneuver plan from all possible maneuver plans.

4. Conclusions

The recommended maneuver plan resulted from this research is the 2-month maneuver plan. This maneuver plan gives the lowest cost either for fuel or launching. On the other hand, this maneuver plan does not give the smallest local time drift. However, the local time that occurred in this maneuver plan is arguably tolerable (only 14.2 minutes).

But, this maneuver plan is not the best compared to all other possible maneuver plans. Maneuver plans with lower maneuver intervals may be more optimum than the 2-month one as the fuel required tends to be lower as the maneuver interval becomes shorter. Hopefully, further research will be conducted to analyze the most optimum maneuver plan from all possible maneuver plans. Moreover, the investigation of correction maneuver strategies controlling other parameters other than inclination could also reveal the most optimum correction maneuver in terms of controlled parameters.

Acknowledgments

The authors would like to thank Satriya Utama, M.T. who inspired the authors to research this topic, and the Faculty of Mechanical and Aerospace Engineering of Bandung Institute of Technology that provides supervision for this research.

Contributorship Statement

MRZ designed the methodology, developed the simulation, analyzed the results, and prepared the manuscript; REP designed the methodology and analyzed the results.

References

Anflo, K. & Möllerberg, R. (2009). Flight demonstration of new thruster and green propellant technology on the PRISMA satellite. *Acta Astronautica*, *65*(9–10), 1238–1249. https://doi.org/10.1016/j.actaastro.2009.03.056

Capderou, M. (2005). *Satellites: Orbits and missions*. France: Springer.

Hasbi, W. & Suhermanto. (2013). Development of LAPAN-A3/IPB satellite an experimental remote sensing microsatellite. *Proceedings of the 34th Asian Conference on Remote Sensing 2013, 2*, 1508–1515.

Hughes, S. P., Qureshi, R. H., Cooley, D. S., Parker, J. J. K., & Grubb, T. G. (2014). Verification and validation of the general mission analysis tool (GMAT). *Proceedings of the AIAA/AAS Astrodynamics Specialist Conference 2014*. https://doi.org/10.2514/6.2014-4151

Jemadu, L. (2020). *Peluncuran Satelit LAPAN-A4 Diundur ke 2021*. Retrieved October 2020, from https://www.suara.com/tekno/2020/07/10/221659/peluncuran-satelit-lapan-a4-diundur-ke-2021

Kuznetsov, E. D. & Jasim, A. T. (2016). On the long-period evolution of the sun-synchronous orbits. *Solar System Research*, *50*(3), 197–203. https://doi.org/10.1134/S0038094616030059

Llop, J. V., Roberts, P. C. E., Palmer, K., Hobbs, S., & Kingston, J. (2015). Descending sun-synchronous orbits with aerodynamic inclination correction. *Journal of Guidance, Control, and Dynamics*, *38*(5), 831–842. https://doi.org/10.2514/1.G000183

MacDonald, M., McKay, R., Vasile, M., & De Frescheville, F. B. (2010). Extension of the sun-synchronous orbit. *Journal of Guidance, Control, and Dynamics*, *33*(6), 1935–1939. https://doi.org/10.2514/1.49011

Paskalis, Y. (2015, November 23). *Satelit LAPAN-A3 Butuh Rp 65 Miliar untuk Mengorbit*. Retrieved from https://tekno.tempo.co/read/721510/satelit-lapan-a3-butuh-rp-65-miliar-untuk-mengorbit/full&view=ok

Ruggiero, A., Pergola, P., Marcuccio, S., & Andrenucci, M. (2011, September 11–15). Low-thrust maneuvers for the efficient correction of orbital elements [Paper presentation]. The 32nd International Electric Propulsion Conference, Wiesbaden, Germany.

Saifudin, M. A., Karim, A., & Mujtahid. (2018). LAPAN-A4 concept and design for earth observation and maritime monitoring missions. *Proceedings of the 2018 IEEE International Conference on Aerospace Electronics and Remote Sensing Technology*, 44–48. https://doi.org/10.1109/ICARES.2018.8547143

The GMAT Development Team. (2012). General mission analysis tool (GMAT): User's guide.

Triharjanto, R. H., Hasbi, W., Widipaminto, A., Mukhayadi, M., & Renner, U. (2004). LAPAN-TUBSAT: Micro-satellite platform for surveillance & remote sensing [Special publication]. European Space Agency, ESA SP, 277–283.

Utama, S., Hakim, P. R., & Mukhayadi, M. (2019). Quarter orbit maneuver using magnetorquer to maintain spacecraft angular momentum. *IOP Conference Series: Earth and Environmental Science, 284*, 012046. https://doi.org/10.1088/1755-1315/284/1/012046

Utama, S., Saifudin, M. A., & Mukhayadi, M. (2018). A green propulsion system requirement for LAPAN-A4. *Proceedings of the 2018 IEEE International Conference on Aerospace Electronics and Remote Sensing Technology*, 163–168. https://doi.org/10.1109/ICARES.2018.8547078

Vallado, D. A. & McClain, W. D. (2013). *Fundamentals of astrodynamics and applications* (4th ed.). Ohio: Microcosm Press.

Zuhri, M. R. (2020). Simulasi dan perencanaan station keeping satelit LAPAN-A4 (SSO) dengan menggunakan propulsi non-impulsif [Undergraduate's thesis, Bandung Institute of Technology]. Bandung Institute of Technology Digital Archive. https://digilib.itb.ac.id/index.php/gdl/view/48271/

Preliminary Power Budget Analysis for Equatorial Low Earth Orbit (LEO) Communication Satellite

Desti Ika Suryanti[1,3], Sri Ramayanti [2], Mohammad Mukhayadi [3]

[1]Satellite Technology Center, National Institute of Aeronautics and Space (LAPAN), Indonesia

e-mail: desti.ika@lapan.go.id

Received: 09-11-2020. Accepted: 01-03-2021. Published: 30-06-2021

Abstract

Satellite Technology Center – LAPAN would develop a constellation of 9 communication satellites in a low equatorial orbit. These satellites would perform as data collection platforms for many sensors that spread across the Indonesian territory. The data from the sensors will be downlink to Indonesia's ground stations in real-time. This research aims to analyze the power budget of those satellites to decide how many solar panels and batteries are required to perform their mission. The method in this research began by calculating the power requirements of each mission per orbit period to estimate power consumption and calculate the power generated by the solar panels. The results of these calculations will be implemented to the power system design to find the satellite solar cells/ panels arrangement and battery capacity allocation. To minimize the development time and cost, the solar array design in this study considers the utilization of previous solar panel design of LAPAN-A series satellites as a design constraint. This study shows the configuration of 3 body-mounted solar panels and 2 deployable solar panels that could support the mission operation of communication satellite in the low equatorial orbit. For energy storage, these satellites should be equipped with 28 V Li-ion in the 8Sx3P configuration.

Keywords*: Micro satellite; communication satellite; power budget, solar panel; li-ion battery.*

1. Introduction

Manuscript Satellites have a universal characteristic, with a lot of flexibility in the application, efficient in terms of costs, and able to answer various needs such as data communication or voice wireless, the need for financial transactions, internet connection means, and so on. Communication satellites are essentially relay stations placed on the Earth to receive, strengthen, and transmit the accepted analog signals and convert them into digital signals or radio frequencies. One of the satellite applications is its utilization as a means of communication due to many advantages compared to the terrestrial communication system. Satellite Technology Center (Pusteksat) of LAPAN has a heritage in developing low orbit small satellites such as LAPAN-TUBSAT (Triharjanto et al., 2004), LAPAN-A2 (M.A. Saifudin & Mukhayadi, 2013), LAPAN-A3 (Utama, Saifudin, & Mukhayadi, 2018). LAPAN-TUBSAT have imaging mission using video camera as its payload. Meanwhile the missions of LAPAN-A2 are earth observation, maritime monitoring and supporting disaster mitigation. And for the LAPAN-A3, the mission is similar with LAPAN –A2 with addition scientific research mission for earth magnetic field measurement. Aiming for mastery the satellite technology, Pusteksat develop satellites in low orbit constellation with communication mission. Due to the difference in missions, it is necessary to analyze the power budget of this satellite.

Figure 1-1 shows the conceptual design of a low orbit satellite constellation that carries a communication mission, which is composed of four segments, as follows:

a. *Space segments*. The space segment consists of nine satellites orbiting the equatorial Low Earth orbit (LEO) at an altitude of ± 600 km and a 0° inclination angle to perform a real-time communication for Indonesia and other countries in the equatorial region. The satellite carries several communication payloads:
   1. VHF Data Exchange System (VDES), which serves to collect data from sensors, in particular for disaster mitigation and early warning systems.

2. Voice Repeater (VR) and Automatic Packet Reporting System (APRS) to support the amateur communication as well as disaster/ emergency communication.
3. Automatic Identification System (AIS) receiver that serves for vessel detection.
4. Automatic Dependent Surveillance-Broadcast (ADSB) receiver for aviation surveillance.
5. Experimental communications in S and Ka-band.

The satellite in real-time using the X/S band frequency will retransmit all of the received digital messages from VDES, AIS, and ADSB. For Telemetry Tracking and Command (TTC), the satellite uses the UHF frequency.

b. *User segments*. The user segment consists of (1) the user terminals in the field to support disaster sensors and early warning such as tidal sensors, tsunami buoys, geomagnetic sensors, weather stations, and seismographs; (2) Handheld sound repeater to support disaster communication; and (3) additional missions for aircraft and ship monitoring and supervision.
c. *Ground segment*. The ground segment is responsible for mission control consists of the ground station located in Bukittinggi, Bogor, Parepare, and Biak. This will download all the payload data on the satellite using the S-Band frequency.
d. *Network segment*. Data from satellites will be processed and transferred in real-time via cloud servers to agencies, ministries, or private parties.

The design of the power system on a satellite must pay close attention to the power budget because satellite operations carry out many missions in the space duty cycle. This study aims to know the number of solar panels as well as the battery capacity required to support the mission operations of small satellite carrying communication devices in the low Earth orbit. As the design constraint to minimize the development time and cost, the solar array design in this study should estimate whether the previous solar panel design, i.e. panel design of LAPAN-A4 satellite, still could meet the requirements or not.

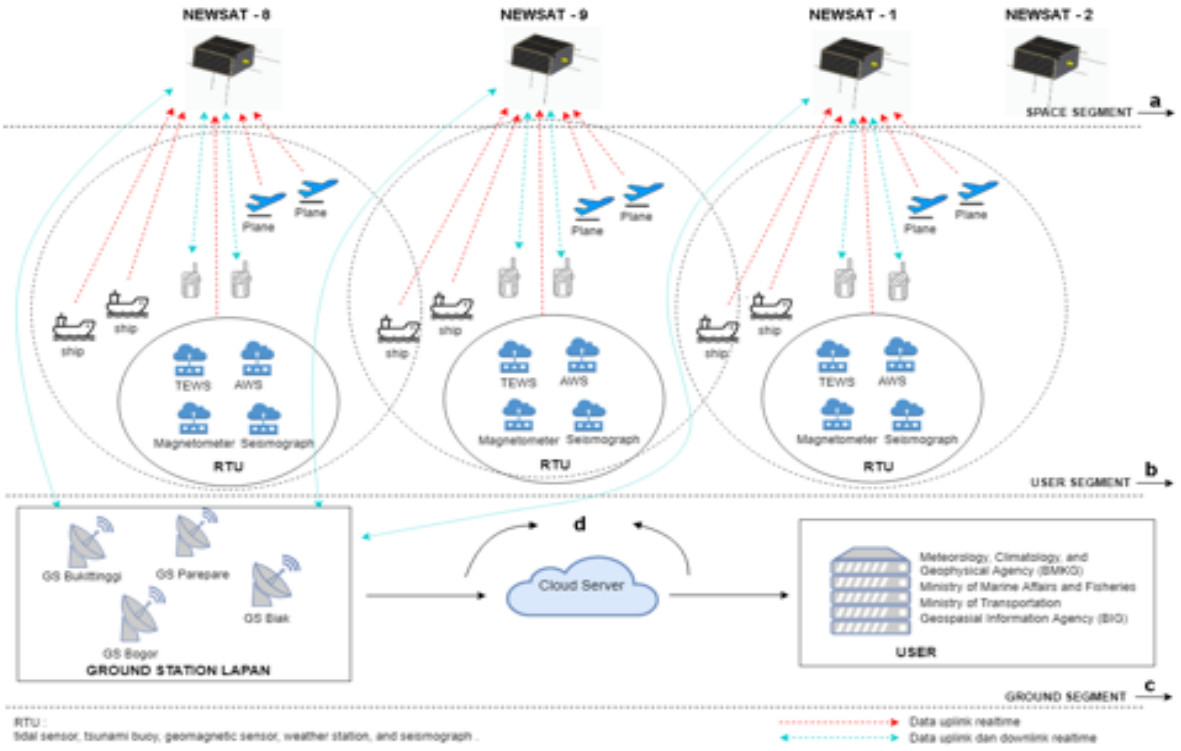

Figure 1-1: Low Orbit Communication Satellite Mission Architecture.

2. Methodology

The power budget analysis in this study is conducted by the following steps:

2.1. Identifying the amount of power consumption required per device

The first step in this study is to identify the devices that will be installed in the satellites, the number of each device to be carried, as well as the operating current and the

voltage of each device. In general, the power requirements of a satellite calculated are divided into two groups, namely the power requirements of the bus system and the power requirements of the payload system. The bus system requires power for operations of Power Control & Data Handling (PCDH), reaction wheels, gyro, magnetic torques, star sensors, Global Positioning System (GPS), and TTC. Meanwhile, the payload system requires power for the magnetometer operation, AIS receiver, VDES, ADSB, VR, APRS, S-band for Mobile Satellite Service (MSS), X/S Band Payload Transmitter, Ka-band communications, and payload data handling systems (PDHS).

2.2. Establishing the mission operation of low orbit communication satellites.

To establish the mission operation of low orbit communication satellite, roughly the satellite operations split into two modes, as follows:

a. Acquisition mode, where all the components of the bus and some satellite payloads ON continuously to collect data from sensors on Earth.
b. Active communication mode, where some communication devices are active while the satellites are in the Ground station coverage. Active communication mode is divided into 5 modes, namely:
    1. TTC active mode, in which the operator performs TTC activity for satellite's housekeeping or attitude maintenance through a series of command and telemetry.
    2. VR mode, in which the VR device is activated to repeat any voice signal from users.
    3. Data downlink mode, when the satellite sends the recorded data to the Earth station through X/S Band frequency.
    4. MSS mode, when the satellite delivers a telecommunication service to the mobile users.
    5. Ka-Band communications mode, which is used for experimental communication using a microwave.

2.3. Calculating the orbital period of Eclipse and Daylight.

In the power budget analysis, the duration of the eclipse and the daylight is crucial in determining the satellite power requirements during its operating cycle. Figure 2-1 gives the geometrical relation between spacecraft orbit and the Earth to find maximum eclipse duration. The eclipse will occur in every cycle of the orbital period. When the satellite enters the eclipse period, the solar panels on the satellite will not get sunlight so there is no power generated. Thus, satellites use the battery as a resource to keep running all the electronic devices. The orbital period can be found by Equation (2-1), while the duration of the eclipse, that illustrated in Figure 2-1, is obtained using Equation (2-2) (Apgar et al., 2005).

$$P = 1.658\times10^{-4}\times(6378.14 + h)^{3/2} \quad (2\text{-}1)$$

Where P is the orbit period (minutes), h is satellite altitude (km).

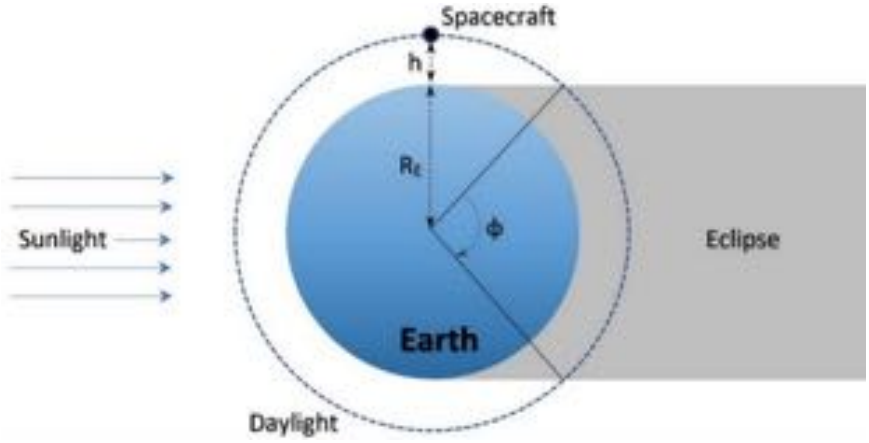

Figure 2-1: Illustration of duration eclipse time.

$$T_E = P(\Phi/360\,deg) \quad (2\text{-}2)$$

With Φ follow:

$$sin\left(\frac{\Phi}{2}\right) = [\frac{R_E}{R_E+h}]$$

Where R_E is the radius of Earth (km); h is satellite altitude (km); Φ is eclipse cover (degree); and T_E is eclipse period (minutes).

2.4. Set the concept design of the satellite power system

The design concept of satellite power systems for low orbit communications on this study adopted the power system design of the LAPAN-A4 satellite as shown in Figure 2-2. The main power resource comes from the solar panels that are mounted on the spacecraft body or assembled in the deploy mechanism. The solar panel consists of a solar cell compiled into 4 strings, and each string consists of 16 cells that produce a nominal voltage of 28 V with an operating voltage range of 24 V to 33 V. The electrical power generated by the solar panels is then stored in the Lithium-Ion batteries. The battery pack serves to provide the power to be used during the mission. The charging and discharging process of the battery is controlled by the Battery Charge Regulator (BCR) on PCDH (Muhammad Arif Saifudin & Karim, 2016). PCDH serves to detect battery under voltage and control charging and discharging processes.

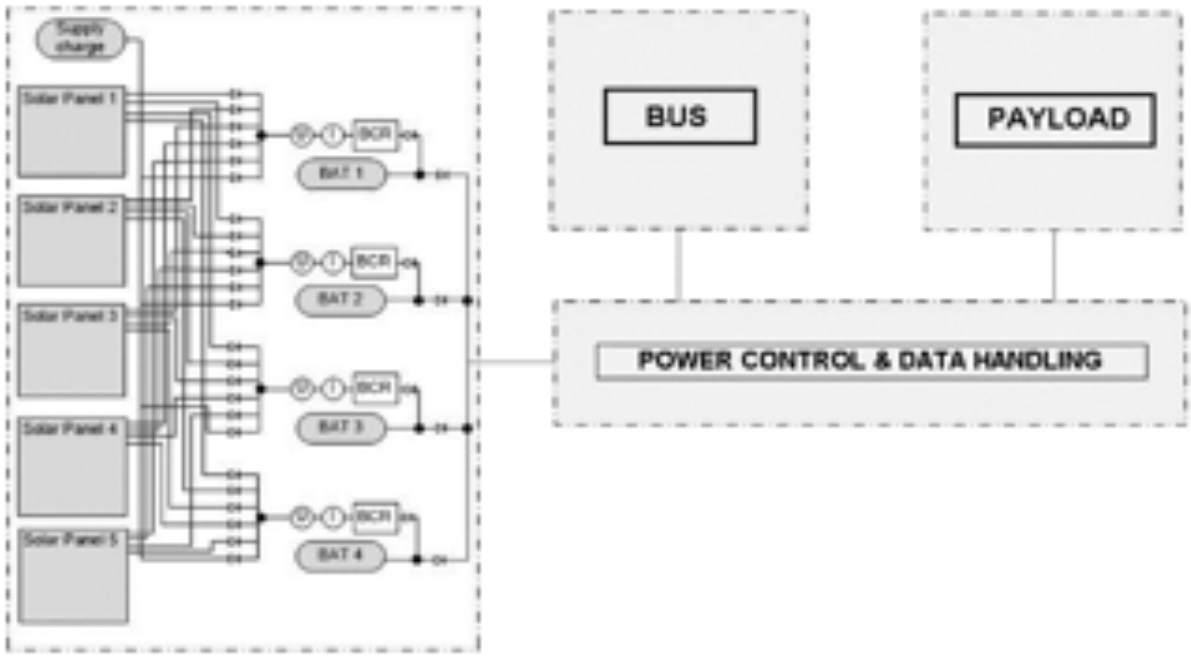

Figure 2-2: Low Orbit Communication Satellite Power System.

2.5. Calculating the power requirement

To determine the number of power needs on this satellite, calculation of the amount the power that should be produced using Equation (2-3).

$$P_{sa} = \frac{(\frac{P_e T_e}{X_e} + \frac{P_d T_d}{X_d})}{T_d} \quad (2\text{-}3)$$

Where Psa is power that must be generated by solar panels (W); Pe is spacecraft power requirement during eclipse (W); P_d is spacecraft power requirement during daylight (W); T_e is lengths of eclipse period (minutes); T_d is lengths of daylight period (minutes); X_e is path efficiency value for the eclipse; X_d is path efficiency value for daylight.

2.6. Calculating the power production of solar panel systems and the needs of energy storage systems

After calculating the amount of power to be produced, then the next step is to select the type of solar cell and estimate the power output, P_o, with the Sun normal to the surface of the cells by using Equation (2-4).

$$Po = 1367 W/m^2 \times \eta \tag{2-4}$$

Where P_o is the power output (W/m2); here P_o is the power output (W/m2) and ŋ is the efficiency of the solar cell; 1367 is the efficiency of the solar cell; 1367 W /m^2; ŋ is the solar constant in the vicinity of the Earth. By knowing the power output of the solar cells, then the beginning-of-life (BOL) power production capability per unit area of the array can be determined by using Equation (2-5).

$$P_{BOL} = P_o I_d \cos\theta \tag{2-5}$$

Where P_{BOL} is power production capability at beginning of life (W/m^2); Po is the power output (W/m^2); Id is inherent degradation; θ is sun incidence angle (degree).

The solar array must be able to supply power for operation and recharging the battery until the end of life (EOL). To determine the EOL power production capability, P_{EOL} (W/m^2), the life degradation of the solar array (L_d) should be determined. Factors that influence that L_d of solar array include thermal cycling in and out of eclipses, micrometeoroid strikes, plume impingement from the thrusters, and material out gassing for the duration of the mission (Apgar et al., 2005). Generally, the degradation of gallium arsenide and multi-junction in LEO is 2.75% per year and 0.5% per year respectively. Therefore, the actual lifetime degradation can be estimated using Equation (2-6).

$$L_d = (1 - degradation/yr)^{satellite\ life} \tag{2-6}$$

Therefore, the estimation of the array performance per unit area at EOL is obtained using Equation (2-7).

$$P_{EOL} = P_{BOL} L_d \tag{2-7}$$

Knowing the power requirement and the power EOL would enable to estimate the solar array area, A_{sa} (m^2) required for a spacecraft by using Equation (2-8).

$$A_{sa} = \frac{P_{sa}}{P_{EOL}} \tag{2-8}$$

Knowing the required solar array area is the starting point to design a configuration of solar panels. The other key reason to design the solar array configuration is an illumination of the Sun. Solar arrays illumination intensity depends on orbital parameters such as the Sun incidence angles, eclipse periods, solar distance, and concentration of solar energy. Aiming the maximum illumination, the solar panel needs to be always pointing to the Sun. However, the power production of solar panels depends on the relative motion of the Sun against the normal direction of solar panels. Especially for equatorial orbit, the Sun illumination is seasonal, in which the illumination is varying between equinox and solstice. In a one-year cycle, the equinox occurs in March and September, while the solstice took place in June and December. Equinox is a condition of the Earth when day and night has the same duration, while the solstice conditions make the area on the Earth experience the longest or shortest daylight. In the equatorial orbit, the power produced by the solar panels in the solstice could be reduced due to the inclination of the Sun would be up to 23.50° (Zahran, 2006). The comparison of Sun's illumination between the equinox and solstice condition of the solar panel for nadir pointing satellites in the equatorial orbit can be seen in Figure 2-3. The illumination value (I_l), calculated using the following Equation (2-9).

$$I_l = \cos\alpha \,.\cos\,(lat_{sun}) \tag{2-9}$$

Where α = ω. t in which ω is satellite's orbit angular velocity (0.062 deg/sec); lat_{sun} is the sun latitude position.

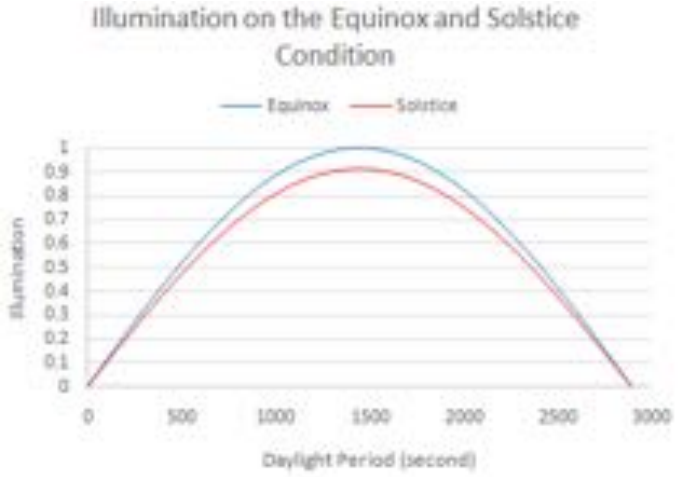

Figure 2-3: Illuminating solar panel of equatorial LEO satellite at 600 km altitude.

Included in the power system, batteries are a key component of the satellite that provides power during the eclipse. Indeed, in the daylight periods, the satellite is powered by the solar panels that in parallel recharge the battery; but in the shadow periods, the battery takes the relay and delivers power to the bus and payload (Borthomieu, 2014). Currently, Lithium-Ion type of batteries has been vastly used in the space mission. Table 2-1 shows the parameters for batteries to be used in LEO missions.

Table 2-1: Parameters for batteries (Borthomieu, 2014)

Parameter	Value
Life duration	2-15 years
DOD	10-40%
Charge rate	C/3
Discharge rate	C/2 to C/1.5
Temperature range	0°C to +40°C
Compliance standard	ESA and NASA standards

Two battery configurations by Li-ion satellite, namely S-P topology and P-S topology. This study uses S-P topologies that are characterized by serial strings of cells assembled in parallel. Usually, Equations (2-10) can be used to calculate the number of series cells

$$N_s = \frac{V}{V_c} \tag{2-10}$$

Where Ns is number of series cells; V is bus voltage (V); Vc is one cell voltage (V). Then, the calculation of battery capacity uses Equations (2-11).

$$C = \frac{P_e \times T_E}{N_s \times \tilde{V}cell_{EOL} \times DoD} \tag{2-11}$$

Where C is battery capacity (Ah); Pe is eclipse power (W); T_E is eclipse period (hour); $\tilde{V}cell_{EOL}$ is average cell voltage at EOL (V); DoD is depth of discharge. To calculate how many numbers of parallel cells, Equation (2-12) is used.

$$N_p = \frac{C}{C_c} \tag{2-12}$$

Where N_p is number of parallel cells; C is battery capacity (Ah); C_c is capacity of one cell (Ah).

3. Result and Analysis

3.1. Power Consumption of Devices

Satellites carry devices that consume certain power and duration to support the mission operation as shown in Table 2-2.

Table 2-2: Power Consumption of Equatorial LEO Communication Satellite

Device	No	Voltage (V)	Current (mA)	Duration (hour)	Power (Watt)	Energy (Wh)
BUS SYSTEM						
PCDH	1	28.0	98.15	1.6	2.75	4.40
TTC Active	2	28.0	685.71	0.3	7.20	311.52
TTC Idle	2	28.0	58.97	1.3	2.68	4.29
S Band TTC Uplink	1	28.0	58.97	1.6	1.65	2.64
S Band TTC Downlink	1	28.0	560.82	0.3	2.94	4.71
Reaction Wheel X	1	28.0	10.15	0.3	0.05	0.09
Reaction Wheel Y	1	28.0	114.73	1.6	3.21	5.14
Reaction Wheel Z	1	28.0	10.15	0.3	0.05	0.09
Gyro X	1	5.0	108.0	0.3	0.10	0.16
Gyro Y	1	5.0	108.0	1.6	0.54	0.86
Gyro Z	1	5.0	108.0	0.3	0.10	0.16
Coil	3	28.0	30.00	1.6	2.52	4.03
Star Sensor	2	28.0	67.33	0.3	0.71	1.13
GPS	1	28.0	99.62	1.6	2.79	4.46
TOTAL POWER CONSUMPTION OF BUS SYSTEM					27.31	43.69
PAYLOAD SYSTEM						
Magnetometer	1	28.0	32.80	1.6	0.92	1.47
AIS receiver	1	28.0	27.39	1.6	0.77	1.23
ADSB	1	3.3	400.0	1.6	1.36	2.18
VDES	1	28.0	27.39	1.6	0.77	1.23
VR	1	28.0	685.71	0.4	4.80	7.68
APRS	1	28.0	716.56	1.6	20.06	32.10
S Band MSS	1	28.0	560.82	0.3	2.94	4.71
X/S Band Payload Transmitter	1	28.0	2455.48	0.4	17.19	27.5
Ka Band Voice Communication	1	28.0	2455.48	0.3	12.89	20.63
PDHS	1	28.0	404.46	1.6	11.33	18.12
TOTAL POWER CONSUMPTION OF PAYLOAD SYSTEM					73.02	116.84
TOTAL					100.33	160.53

Each device has certain functions and tasks, some of them are working all the time, which are indicated by 1.6 hours duration equal to the orbital period. Generally, 70% of total power consumption is spent in the payload system. PCDH is the main computer on the spacecraft, which consists of a combination of the Power Control Unit (PCU) and Onboard Data Handling (OBDH) units (Karim, 2015). The reaction wheel is the main actuator for spacecraft attitude control that produces angular torque by rotating the wheel. Gyro is a sensor that measures angular motion. Magnetic torque (Coil) is a device made from coil wire that interacts with the Earth's magnetic field to produce control torque. It can compensate for magnetic residue on the spacecraft as well as dumping the angular momentum when the reaction wheel is saturated (Dear, 2010). Star Sensor is a reference sensor that provides star position data to navigate the spacecraft's orientation (Asadnezhad, Eslamimajd, & Hajghassem, 2018). GPS is used to provide position and time synchronization for the spacecraft. The TTC is a device that provides a connection between the satellite and the facilities on the ground. A magnetometer is a sensor for measuring the Earth's magnetic field. AIS receiver is a satellite payload that receives messages from ships in certain formats and frequency (Judianto & Agung, 2014). VDES is a radio communication system that enhanced the loading of the VHF Data Link (VDL) of the AIS and supports new digital services. ADSB is a system to detect aircraft that transmits the information of altitude, position, speed, direction, and other information (Nurhayati, 2014). VR is a device that receives a voice signal and retransmits it. APRS is a communications protocol and device that receives and retransmits digital broadcast messages (Hardhienata, Triharjanto, & Mukhayadi, 2011). S-Band and Ka-Band communication are a payload is used to support experimental communication between users on the ground. X/S Band payload transmitter is a system that transmits the payload data to the ground station. PDHS is a device that

handles all data management processes ranging from mission data collection, onboard data recording/ retrieval, and data protection (Suhermanto, 2017).

3.2. Solar Array Design

The constellation of communication satellites in this study will be placed into low Earth orbit within 600 km altitude and an inclination angle 0 degrees for 5 years' lifetime. By putting the altitude to the Equation (2-1), it found the orbital period of the satellite is 97 minutes while the eclipse duration from Equation (2-2) gives values of 35 minutes. According to Table 2-2, the average power consumption is defined as 100.33 Watt either during daylight (Pd) or during the eclipse (Pe). The efficiency of the satellite power subsystem in the daylight and eclipse are roughly Xd = 0.995 and Xe = 0.956 (Mukund, 2005). Nowadays, the efficiency of GaAs solar cells could achieve 29.5%, the inherent degradation (Id) is 0.981, and the degradation per year is 2.034 % (Company, 2016). For the prediction of solar cell degradation, this study uses the spectral irradiance reference of air mass zero (AM0) which is the extraterrestrial solar irradiance at a distance of one astronomical unit from the Sun (*ASTM E490 Standard Solar Constant and Zero Air Mass Solar Spectral Irradiance Tables*, 2006). The calculation result of the power requirement is summarized in Table 2-3.

Table 2-3: Power Requirement Calculation of Solar Panel

Parameter	Value
Power that must be generated by Solar Panel (W)	$P_{sa} = 161.66$
Power Output (W/m²)	$Po = 403.27$
Power BOL (W/m²)	$P_{BOL} = 395.7038$
Life Degradation	$L_d = 0.90$
Power EOL (W/m²)	$P_{EOL} = 357.0667$
Solar Array Area (m²)	$A_{sa} = 0.45$

Photovoltaic cells can be wired together to make solar panels for larger size loads (Shaikh, Waghmare, Labade, Fuke, & Tekale, 2018) (Id et al., 2019), (El-Ghonemy, 2012). The panels can be collected together to create a solar array for large-scale power generation (Heo et al., 2013). The placement of solar panels should orient their normal direction to the Sun so they will generate adequate power throughout the mission (Santoni et al., 2014). Typically, in the previous LAPAN-A satellite series, the solar panels were mounted on the spacecraft body. To meet the power requirements, the spacecraft could implement a deployable mechanism for solar panels. Sometimes, the deployable mechanism is equipped with a sun tracker rotator to maximize the illumination. However, implementing sun tracker rotator in the small satellite is not desired due to the increased complexity of the satellite design. Figure 2-4 illustrated the nominal flight configuration and solar panel placement in the defined axis of the equatorial satellite.

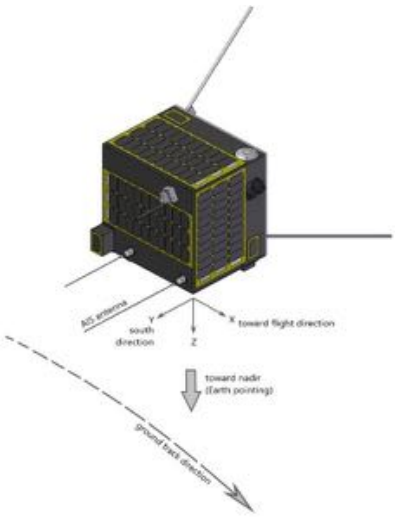

Figure 2-4: Nominal flight configuration and solar panel placement of the equatorial satellite (Source: Hasbi, Kamirul, Mukhayadi, & Renner, 2019).

The power production is equivalent to the Sun illumination on the solar panels (Amajama, 2016). For comparing the power production, there are four configurations of solar panel placement, from the simplest to the more complex one. Refer to the spacecraft axis is shown in Figure 2-5, Configuration A consist of one solar panel installed on -Z side; Configuration B contains three panels installed on +X, -X, and – Z sides; Configuration C contains five panels installed on +X, -X, +Y, -Y, and – Z sides; And Configuration D contains five panels which are three solar panels installed on +X, -X, and -Z sides, while the rest two panels placed on -Z side using the deployable mechanism.

According to Table 2-4, the required solar panel area is 0.45 m^2 to meet the power requirement. While the solar panel design adopts the panels of the LAPAN-A4 satellite that is consisted of four strings, every string contains 16 cells, and each solar cell area is 30.18 cm^2, then a one-piece of a solar panel has an effective area of 0.193 m^2. It means the satellite requires 2.33 solar panels that should face the Sun continuously. During the nadir pointing mission, in which one side of the spacecraft (usually defined as +Z side) always points to the Earth, the Sun illumination on each side is varying follow Equation (2-9) instead of tracking the Sun. The total accumulation of the illumination value acquired by each panel is defined as illuminated panels and presented in Table 2-4. It shows that only Configuration D would meet the power requirement in both equinoxes and solstice. The solar panel design and the configuration of placement are illustrated in Figure 2-5.

Table 2-4: Comparison of Solar Panels Power Production (Suryanti, Ramayanti, & Mukhayadi, 2019)

Parameter	Configuration A		Configuration B		Configuration C		Configuration D	
	1 body-mounted panel		3 body-mounted panels		5 body-mounted panels		3 body-mounted panels + 2 deployable panels	
	Equinox	Solstice	Equinox	Solstice	Equinox	Solstice	Equinox	Solstice
Illuminated Panels	0.64	0.58	1.27	1.17	1.27	1.57	2.55	2.34
Equivalent Area (m^2)	0.12	0.11	0.25	0.23	0.25	0.30	0.49	0.45

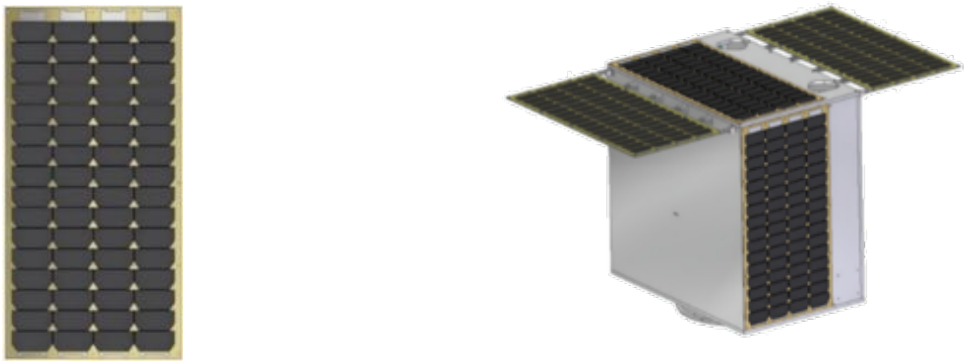

Figure 2-5: Solar Panel Design and the Proposed Placement of Equatorial LEO Satellite

3.3. Energy Storage Design

During the daylight period, spacecraft uses solar arrays to generate power and to charge the batteries. While in the eclipse period, the batteries use their energy storage to

perform the role of the solar panels and providing the satellite subsystem with their required power (Abdi, Alimardani, Ghasemi, & Mirtalaei, 2013). In this study, S-P topology is chosen since it is the most used in LEO satellites that using a regulated 28 V bus (Borthomieu, 2014). The bus voltage required to run electronic devices on the satellite is 28 V that has been implemented also on the LAPAN-A4 power system design.

A small Li-ion battery has the end of the discharge cutoff voltage of 2.7 V, average discharge voltages of 3.5 V, and an end-of-charge voltage of 4.2 V (Mukund, 2005). According to the study by Yannick Borthomieu, Satellite Lithium-Ion Batteries, a 28 V of 8S-1P battery with 15 Ah capacities was tested in a cycle within 20% DOD in LEO. After 40,355 cycles, the voltage of each cell in the test pack has been measured that results in the maximum deviation in voltages for the (eight) cells were 23 mV. Therefore, based on the previous operation of Li-ion battery in LEO, the design of the energy storage system in this study takes the value of 3.75 V of average battery cell voltage, 20% of DOD, 3.73 V of average battery cell voltage at EOL after 7 years (more than 40,000 cycles), and 6.5 Ah of Cell Capacity. Based on the aforementioned specification, the design of energy storage in low orbit communication satellites is presented in Table 2-5.

Table 2-5: Design Parameter of Energy Storage for Low Orbit Communication Satellite

Parameter	Value
Bus Voltage (V)	$V = 28$
Cell Voltage (Vc)	$V_c = 3.75$
Number of Series Cells (NS)	$N_s = 8$
Eclipse Power (W);	$P_e = 100.33$
Eclipse Period (hour)	$T_e = 0.6$
Average Cell Voltage at EOL (V);	$\tilde{V}cell_{EOL} = 3.73$
Depth of Discharge (%)	20
Battery Capacity (Ah)	$C = 9.95$
Cell Capacity (Ah)	$C_c = 6.5$
Number of Parallel Cells	$N_p = 2$

Table 2-5 also indicates that the battery configuration of this satellite is 8S x 2P meaning the battery consist of two strings and each string consists of eight cells of the battery-compiled series. In S-P configuration, if the cell fails the entire string is lost, along with the capacity that should have been provided. However, the voltage remains the same and therefore the satellite system can continue to operate the mission without the other effects of a small reduction in battery capacity (Borthomieu, 2014). However, to secure the mission operation, adding one more string could anticipate if one string is failed. Hence, the recommended configuration is 8S x 3P.

4. Conclusions

The design of the satellite power system, including the solar panels as well as the energy storage system, requires comprehensive power budget analysis. In the equatorial low orbit communications satellite, the solar panel design of the LAPAN-A4 satellite still could meet the power requirements. By implementing, the configuration that contains three body-mounted and two deployable panels, the solar panels can produce enough energy to run all operating modes of the satellite that required power of 100.33 Watt. Furthermore, this low orbit communications satellite has to carry 9.95 Ah of 28 V Li-ion batteries at a minimum in the 8S x 3P configuration to support the mission operation during the eclipse.

Acknowledgements

The author would like to thank Mr. Mujtahid as the Head of LAPAN Satellite Technology Center so that the research and preparation of this paper can be carried out properly.

Contributorship Statement

DIS, SR and MM together designed the method, analyzed the results and prepared the script. In this paper DIS is a major contributor.

References

Abdi, B., Alimardani, A., Ghasemi, R., & Mirtalaei, S. M. M. (2013). Energy Storage Selection for LEO Satellites. International Journal of Machine Learning and Computing, 3(3), 3–6. https://doi.org/10.7763/IJMLC.2013.V3.322

Amajama, J. (2016). Effect of Solar Illuminance (or Intensity) on Solar (Photovoltaic) cell's output and the use of Converging lenses and X or Gamma rays to enhance output performance. International Journal of Engineerng Research and General Science, 4(August), 284–289.

Apgar, H., Bearden, D. A., Bell, R., Berget, R. T., Blake, J. B., & Boden, D. G. (2005). Space Mission Analysis and Design (Third). Microcosm Press and Kuwer Academic Publisher.

Asadnezhad, M., Eslamimajd, A., & Hajghassem, H. (2018). Optical system design of star sensor and stray light analysis. Journal of the European Optical Society -Rapid Publications, 14, 1–11.

ASTM E490 Standar Solar Constant and Zero Air Mass Solar Spectral Irradiance Tables. (2006).

Borthomieu, Y. (2014). Satellite Lithium-Ion Batteries. In Lithium-Ion Batteries Advances and Applications (pp. 311–344). https://doi.org/10.1016/B978-0-444-59513-3.00014-5

Company, C. (2016). 3G30C - Advanced 3G30C - Advanced. Retrieved October 8, 2019, from http://www.azurspace.com/index.php/en/products/products-space/space-solar-cells

Dear, V. (2010). Potensi pemanfaatan sistem aprs untuk sarana penyebaran informasi kondisi cuaca antariksa. 11(3), 72–79.

El-Ghonemy, A. M. . (2012). Photovoltaic Solar ENergy : Review. International Journal of Scientific & Engineering Research, 3(11), 1–43.

Hardhienata, S., Triharjanto, R. H., & Mukhayadi, M. (2011). LAPAN-A2 : Indonesian Near-Equatorial Surveilance Satellite. 18th Asia-Pacific Regional Space Agency Forum (APRSAF), 1–10. Singapore.

Hasbi, W., Kamirul, Mukhayadi, M., & Renner, U. (2019). The Impact of Space-Based AIS Antenna Orientation on In-Orbit AIS Detection Performance. Applied Sciences, 9, 1–19.

Heo, J. H., Im, S. H., Noh, J. H., Mandal, T. N., Lim, C. S., Chang, J. A., … Seok, S. Il. (2013). Efficient inorganic-organic hybrid heterojunction solar cells containing perovskite compound and polymeric hole conductors. Nature Photonics, 7(6), 486–491. https://doi.org/10.1038/nphoton.2013.80

Id, F. F. M., Sangawi, A. W. K., Hashim, S., Ghoshal, S. K., Abdullah, I. K., & Hameed, S. S. (2019). Simple and efficient estimation of photovoltaic cells and modules parameters using approximation and correction technique. Plos One, 14(5), 1–19.

Judianto, C. T., & Agung, W. (2014). Automatic Identification System And Surveillance Technology For Indonesia Marine Security On Lapan-A2 Satellite. International Seminar Of Aerospace Science and Technology, 2, 115–122.

Karim, A. (2015). Power Control Data Handling Satelit Lapan-A2. Aktualita, 10(4), 47–50.

Mukund, R. P. (2005). Spacecraft Power Systems. CRC Press.

Nurhayati, Y. (2014). Implementasi Automatic Dependent Surveillance Broadcast (ADS-B) di Indonesia The Implementasion of Automatic Dependent Surveillance Broadcast (ADS-B in Indonesia. Junral Perhubungan Udara, 40, 147–162.

Saifudin, M. A., & Karim, A. (2016). LAPAN-A4 Concept and Design for Earth Observation and Maritime Monitoring Missions. 2018 IEEE International Conference on Aerospace Electronics and Remote Sensing Technology (ICARES), 5, 1–5. https://doi.org/10.1109/ICARES.2018.8547143

Saifudin, M. A., & Mukhayadi, M. (2013). LAPAN-A2 Attitude Control Strategy for Equatorial Surveillance Mission. Proc. of the 9th IAA Symposium on Small Satellites for Earth Observation.

Santoni, F., Piergentili, F., Donati, S., Perelli, M., Negri, A., & Marino, M. (2014). An Innovative Deployable Solar Panel System for Cubesats. Acta Astronautica, 95, 210–217. https://doi.org/10.1016/j.actaastro.2013.11.011

Shaikh, M. Ri. S., Waghmare, S. B., Labade, S. S., Fuke, P. Vi., & Tekale, A. (2018). A Review Paper on Electricity Generation from Solar Energy. International Journal for Research in Applied Science & Engineering Technology, 5(IX), 1884–1889. https://doi.org/10.22214/ijraset.2017.9272

Suhermanto, . (2017). Pengujian Modul Pengolah Data Telemetri Lapan-a3/Ipb Untuk Menghasilkan Produk Level-0 (the Testof Lapan-a3/Ipb Telemetry Data Processor Module To Produce Level-0 Product). Jurnal Teknologi Dirgantara, 14(2), 125. https://doi.org/10.30536/j.jtd.2016.v14.a2510

Suryanti, D. I., Ramayanti, S., & Mukhayadi, M. (2019). Iluminasi Panel Surya pada Satelit Orbit Rendah Ekuatorial. Elkomika, 7(3), 480–492.

Triharjanto, R. H., Hasbi, W., Widipaminto, A., Mukhayadi, M., & Renner, U. (2004). LAPAN-TUBSAT: Micro-satellite platform for surveillance & remote sensing. European Space Agency, (Special Publication) ESA SP, (571), 277–283.

Utama, S., Saifudin, M. A., & Mukhayadi, M. (2018). Momentum Biased Performance of LAPAN-A3 Satellite for Multispectral Pushbroom Imager Operation. Conference Series : Earth and Environmental Science. IOP Publishing.

Zahran, M. (2006). In Orbit Performance of LEO Satellite Electrical Power Subsystem - SW Package for Modelling and Simulation Based on MatLab . 7 GUI. International Conference on Energy and Environmental Systems, (May), 379–384. Chalkida.

.

Dynamic response of commuter category aircraft wing against drone collision

Budi Aji Warsiyanto[1], Muhammad Hadi Widanto[1], Ilham Musthofa[1], Ichsan Maulana[1]

[1]Faculty of Aerospace Technology, Air Marshal Suryadarma University, Indonesia

e-mail: budiajiwarsiyanto@gmail.com

Received: 30-12-2020. Accepted: 16-03-2021. Published: 30-06-2021

Abstract

The extensive application and development of drones provides high potential airborne collision between manned aircraft and civil Unmanned Aerial Vehicles (UAVs) or known as drone. This phenomenon is a serious threat to aircraft operation safety. The objective of this paper is to investigate the dynamic response of the aircraft wing section commuter category when experienced the drone collision. The 'Mavic' drone with a mass of 735 g was used as an impactor in simulation. Explicit dynamic code ABAQUS was employed to simulate the collision process based on the difference of collision scenarios to assess the hazard. The results showed that 735 g drone collision at the aircraft maximum approach flap speed and cruising speed could cause some damage on the wing front spar. The 735 g drone collision is more serious than 910 g bird strike providing information that component hardness plays an important role in wing damage. Furthermore, the potential source of ignition may be caused by the lithium-ion battery penetrated the airframe.

Keywords*: drone collision, damage assessment, wing section, finite element method.*

Nomenclature (Optional)

σ	=	stress, MPa
ε	=	strain, -
ν	=	poisson's ratio, -
E	=	elastic modulus, GPa
ρ	=	density, kgm^{-3}
G	=	shear modulus, GPa

1. Introduction

Aircraft components are vulnerable to collision from foreign objects such as debris, hail, or bird strike. The flight safety operations of civil aircraft are under threat from these collision incidents and may cause catastrophic accidents. Nowdays, the rapid growth in UAVs makes the impact scenarios even more complicated. (Jenkins & Vasigh, 2013) estimates that the total UAV market will grow to a total economic impact of $82.1 billion by the end of 2025. The airworthiness verification of aircraft structure in facing of drone collision has not been taken into account in its design process. That is, the possibility of impact between aircraft and UAVs exists, whereas its safety risk is unknown. So, evaluations of collisions between UAVs and commercial aircraft are necessary to minimize future damage.

The background of this research is because there are no regulations governing the airworthiness of a drone collision. In addition, up to now, there is no collision simulation between the drone and the commuter wing leading edge for commuters that could be found in published reports. Several published reports such as (Song et al., 2017)(Schroederi et al., 2017) investigated the dynamic response of a high-bypass engine during drone ingestion, different risk levels were classified and a comparison with

bird ingestion. (Meng et al., 2019) performed a collision simulation between a structure level drone and a commercial airliner horizontal stabilizer section to investigate the dynamic response of primary operation components with PAM-CRASH code. (Lu et al., 2020) performed a collision simulation using numerical and experimental between drones and nose aircraft. The research shows the configuration, material, weight, speed, and attitude of drones have significant effects on the impact damage to the windshield.

Based on the explanation of the paragraph above, this research performed a numerical test of the drone collision on the component of the wing section of the commuter category aircraft. The drone with 735 g was used as projectile and a section of a commuter category aircraft wing was employed as the target specimen. The objective of this paper is to investigate the dynamic response of the aircraft wing section when experienced the drone collision and compare it with the effects of bird strike and drone collision. Thus, it can be seen the ability of the wing structure to withstand the impact loads due to drone collisions and bird strikes. In addition, the difference in damage between the drone collision and bird strikes can be obtained. The investigations are performed numerically using the finite element method.

2. Methodology

2.1. Method

Drone collision experimentally provides a direct method to evaluate the damage severity but the high cost of the test makes it's challenging to enumerate all collision scenarios. With the finite element method (FEM), the collision scenario will be more efficient. Drone collision ground test still needs to be conducted to validate numerical simulations. However, due to limited equipment, testing was only carried out numerically. The collision simulations in this study were performed by explicit dynamic finite element solver ABAQUS. The simulation model was performed based on the difference of impact scenarios such as drone attitude (impact angle) and impact velocity to evaluate the damage severity. Comparison with bird strike was also performed in this paper.

2.1.1 The drone

The drone model used in this study has a geometry similar to 'Mavic' supplied by DJI. General size of the drone was about 435*517*70 mm and the total weight (with camera) was 735 g. This mass was close to the bird mass required by the bird strike resistance certification for airframe, namely 910 g. Geometric features and some minor components were eliminated in modeling but their mass was added to the main structure to keep the total mass and center of gravity unchanged. The thin-walled structures such as the frame, propeller, and electronic board were modeled by shell elements, whereas the battery, motors, and camera were modeled by solid elements. The drone's materials and mass distribution are shown in Figures 2-1a and 2-1b. Based on a mesh convergence study in Subsection 2.3.3, the average element size for overall components was 3 and 5 mm as shown in Figure 2-2. The mesh size of 5 mm for frame, propeller, electronic board, battery, and motors, whereas the camera has the mesh size of 3 mm because the geometric is smaller than others component. Overall, the drone model consists of 8,681 shell elements and 2,832 solid elements.

2.1.2 The commuter aircraft wing

The outer wing structure has a length of 2,000 m is used as the target in the impact simulation. The swept angle of the wing was 3.5° and the impact direction was along the aircraft's flight path. The wing mass was 21.81 kg consisting of skin, 11 ribs, and 2 spars fixed to the root as shown in Figures 2-3a and 2-3b. Each component on the wing is modeled with a shell element, S4R. The local mesh is employed on the wing, which is 10 mm in the impact area and larger in the area far from the impact as shown in Figure 2-3c resulting in 68,919 elements. Tie constraints are employed to simulate the rivets joining between skin and ribs and skin and spars.

2.1.3 Constitutive model for materials

The aluminum alloy 2024-T3, 6061-T6, and polycarbonate (PC) were implemented by incorporating isotropic hardening using the Von Mises yield criterion. The mechanical properties of aluminum alloy 2024-T3, 6061, and PC are investigated by ASM Inc. and DJI Technology Co., Ltd and listed in Table 2-1. Von Mises is a simple and convenient criterion to apply as it defines a smooth and continuous yield surface with good approximation at high stresses (Dar et al., 2013). At given principal stresses σ_1, σ_2, and σ_3, the yield criterion is defined as

$$(\sigma_1 - \sigma_2)^2 + (\sigma_2 - \sigma_3)^2 + (\sigma_1 - \sigma_3)^2 = 2{\sigma_y}^2 \quad (3\text{-}1)$$

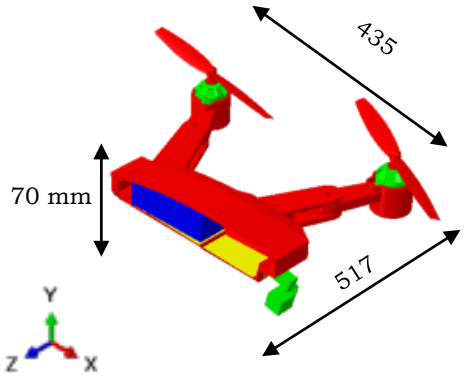

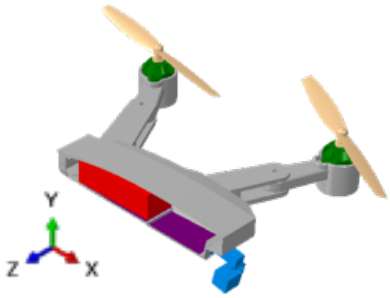

Code	Material
	Polycarbonate
	Lithium-ion
	6061-T6 aluminum alloy
	Glass-epoxy

(a)

Code	Component	Mass (g)
	Frame	237
	Motor	223
	Battery	119
	Electronic board	94.1
	Camera	26.5
	Propellers	35.4
Total		735

(b)

Figure 2-1: (a) Drone materials and (b) mass distribution

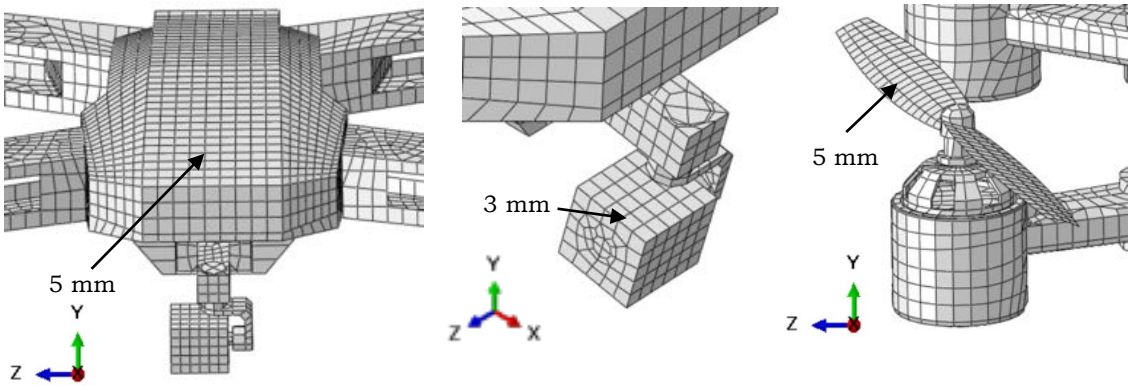

Figure 2-2: Drone element size

The maximum principal strain criterion implies that if the maximum tensile principal strain exceeds the prescribed limits, then the material will instantaneously fail. Failure is predicted when either of the principal strains ε_1 or ε_2, resulting from σ_1 or σ_2, equals or exceeds the maximum strain ε_f corresponding to the yield strength σ_y of the material in uniaxial tension or compression. For yielding in tension the minimum principal strain ε_1 would equal the yield strain in uniaxial tension (Dar et al., 2013). If the strains are expressed in terms of stress, then

$$\varepsilon_1 = \frac{\sigma_1}{E} - \frac{\nu}{E}(\sigma_2 + \sigma_3)$$
$$\sigma_y \geq \sigma_1 - \nu(\sigma_2 + \sigma_3) \quad (3\text{-}2)$$
$$\varepsilon_f = \varepsilon_t - \frac{\sigma_t}{E}$$

The mechanical properties of the glass-epoxy composite were measured by (Waqas et al., 2019) as shown in Table 2-2. Based on the study of (Sahraei et al., 2012)(Sahraei et al., 2014), the cells of lithium-ion batteries and a 60% porosity of the active particles are constructed with crushable foam material in the first approximation, which the mechanical properties are shown in Table 2-3.

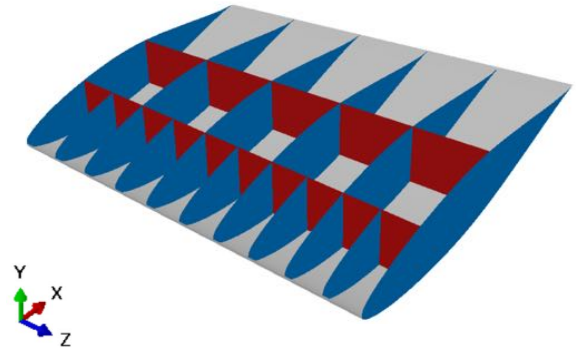

Code	Component	Thickness (mm)
	Skin	0.6
	Spar	1.2
	Rib	0.6

(a)

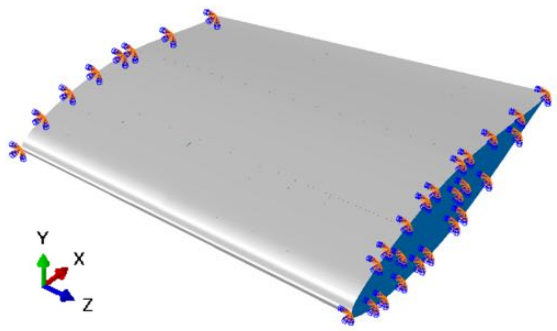

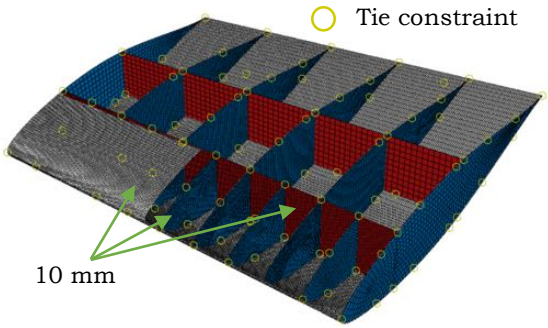

(b) (c)

Figure 2-3: (a) Geometric details, (b) boundary conditions, and (c) element size of the wing

Table 2-1: Mechanical properties of the material

	Density ρ (kgm^{-3})	Elastic modulus E (GPa)	Poisson's ratio ν	Yield stress σ_y (MPa)	Ultimate stress σ_u (MPa)	Failure strain ε_{max}
2024-T3	2,780	73.1	0.33	345	483	0.18
6061-T6	2,700	68.9	0.33	276	310	0.12
PC	1,180	6.2	0.3	62	75	0.2

Table 2-2: Mechanical properties of glass-epoxy

Density ρ (kgm^{-3})	Elastic modulus E_1 (GPa)	Elastic modulus E_2 E_3 (GPa)	Shear modulus G_{12} G_{13} (GPa)	Shear modulus G_{23} (GPa)	Poisson's ratio ν_{12} ν_{13}	Poisson's ratio ν_{23}
2000	45	10	5	3.85	0.3	0.4

Table 2-3: Mechanical properties of the battery

Density ρ (kgm^{-3})	Elastic modulus E (GPa)	Poisson's ratio ν
1,750	0.5	0.01

2.1.4 Computational model

To obtain a balance between accuracy and computational efficiency was performed a mesh sensitivity study. Drone component, i.e motor was impacted to an aluminum alloy 2024-T3 skin of wing at a velocity of 80 ms-1. The mesh sizes of the skin were 30 mm, 15 mm, 10 mm, 7 mm, and 5 mm. The internal energy of the skin was employed as the criterion which is shown in Figure 2-4. It can be seen that the performances of the FE models were almost identical when the mesh size was below 10 mm which equals 45,200 elements. Finally, an average element size of 10 mm was employed in this research.

The dynamic explicit analysis was employed in this simulation because of its effectiveness to solve highly non-linear problems. The critical time step was 1*10−5 s to capture all energy associated with the stress wave propagation during the impact process. The friction behavior between the drone and the wing was set to be 0.26 based on a material handbook. The skin, spar, and rib structure are modeled using a 4-node shell continuum (S4R) element with 5 integration points along the direction of the element thickness. Hourglass control with enhanced is used to prevent artificial zero energy deformation mode. Additionally, the integration point is used to prevent volumetric locking during impact. General contact was employed to define all contact's behavior for each component.

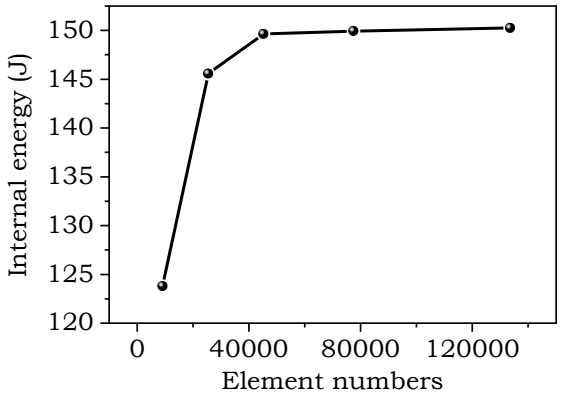

Figure 2-4: Mesh convergence study

3. Result and Analysis

3.1. Different impact location and drone attitude

Variation of simulations was performed to study the effect of different impact locations and drone attitudes on the dynamic response of the wing and determine the most serious scenario to damage the wing structure. The impact velocity was used to the simulations of different impact location and drone attitude was 80 ms^{-1}. This impact velocity was relative value which consists of the drone's maximum velocity of 18 ms^{-1} and aircraft velocity of 62 ms^{-1} at the aircraft maximum approach flap. The aircraft velocity was chosen because the airworthiness regulations for bird strikes, namely CASR 23.775 (Republic Indonesia Ministry of Transportation, 2014) set the impact parameter for commuter aircraft was a 910 g bird when the velocity of the aircraft is equal to the aircraft's maximum approach flap speed. Two locations of impact were analyzed, namely on the rib and between ribs as shown in Figure 3-1a. Figure 3-1b shows that there was global deformation at the leading edge of the wing and that there was no serious damage to the wing structure when the impact location was on the rib. However, when the impact on between the ribs, the drone broke the skin and hit the front spar so it is considered to be more serious than the rib situation. Figure 3-2 shows the wing internal energy for the difference in collision, that is, on the rib and between the ribs. It is seen

that the internal energy between the ribs is lower than collision on the ribs. This is due to when the collision on between the ribs, the skin structure fails so that the energy absorbed by the deformation is lower than the collision on the rib (no damage and the wing structure absorbs energy by deformation).

Different drone attitudes (impact angle) were also simulated, while the center of gravity of the drone was not changed. The attack angle varied from −45° to 45° at an interval of 22.5°. The impact scenarios were marked #1−#5 as shown in Figure 3-3. The principal strain of the wing was employed as the criterion to evaluate the impact consequences. Based on Figure 3-4, it can be assumed that the drone with no attack angle (0˚) would cause the plastic strain reaches a value equal to the strain failure. This is supported by Figure 3-5 which shows the comparison of internal energy of wing for different drone attitudes. As explained by the difference in impact location (on rib and between rib), the internal energy with no attack angle (0°) has the lowest value because the skin structure fails so that the energy absorbed by the deformation is lower than others scenario.

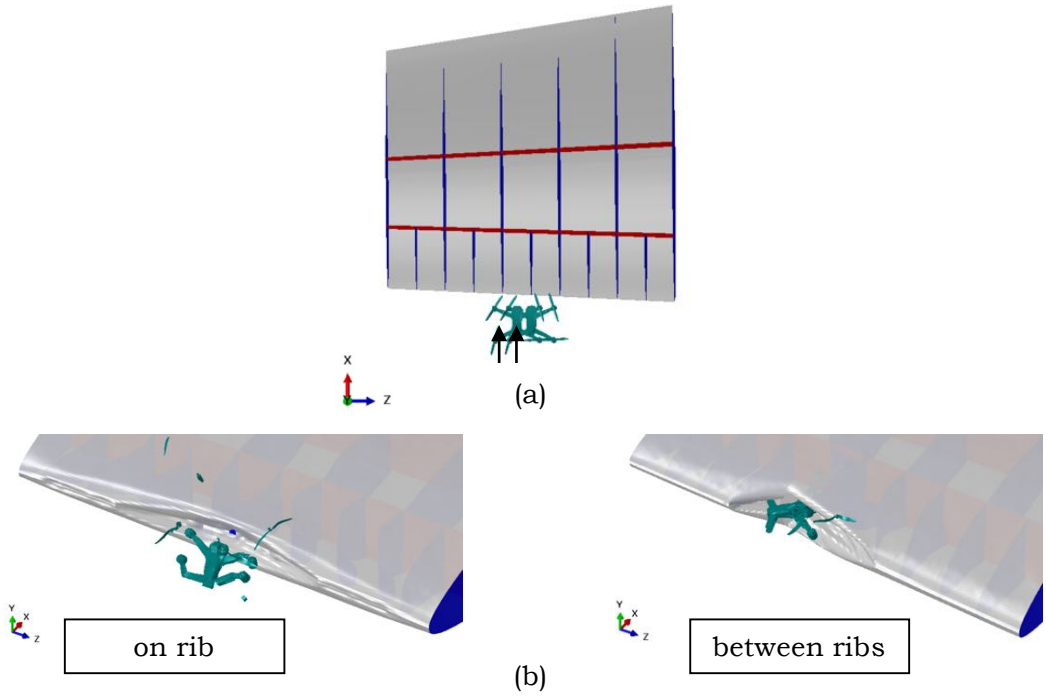

Figure 3-1: (a) Different impact locations and (b) damage characteristics

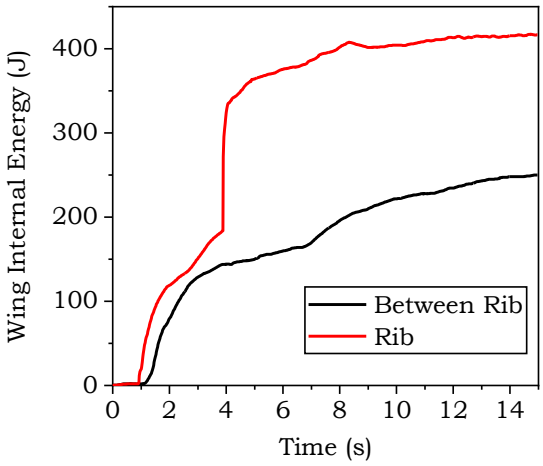

Figure 3-2: Wing internal energy during the drone collision on between rib and rib

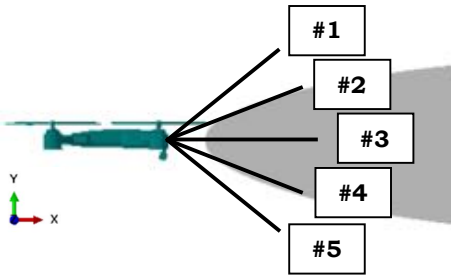

Figure 3-3: Different drone attitudes

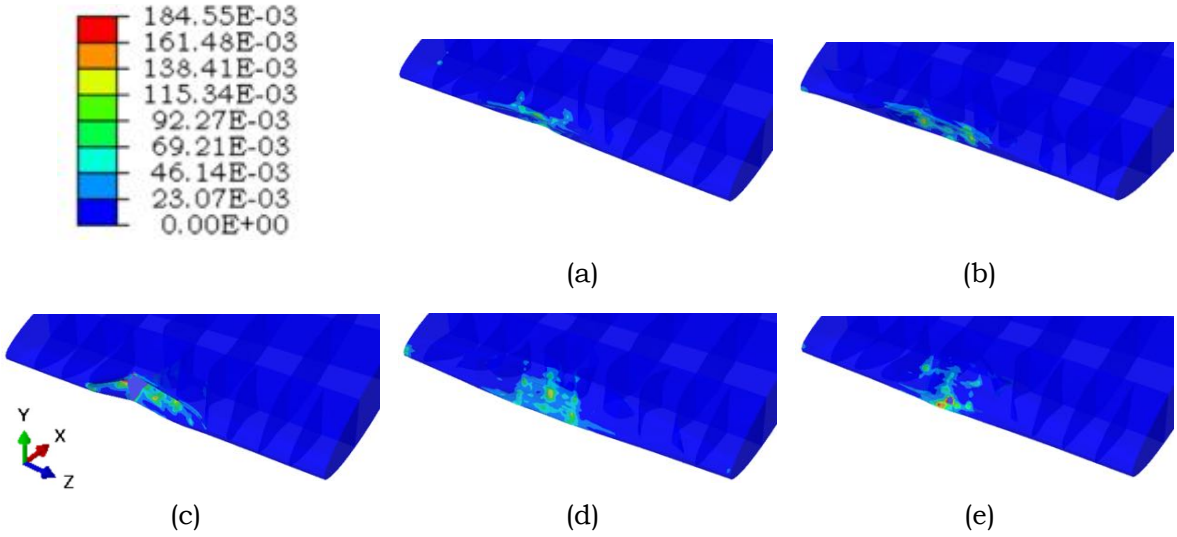

Figure 3-4: The plastic strain at impact angle (a) 45˚, (b) 22.5˚, (c) 0˚, (d) -22.5˚, and (e) -45˚

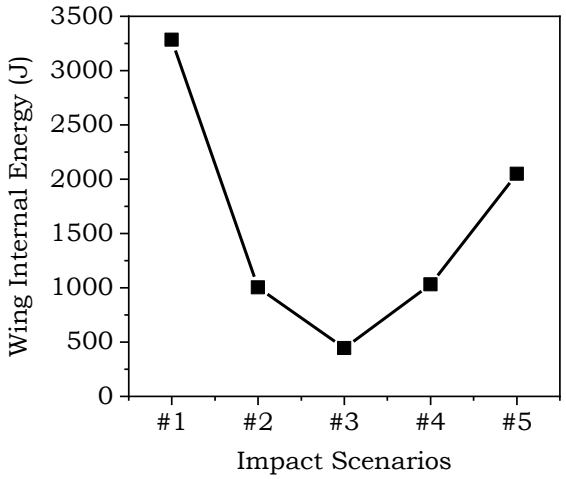

Figure 3-5: Comparison wing internal energy for the different drone attitudes

3.2. Different drone velocity

The impact velocity was varied to determine the minimum and maximum damage when the 735 g drone crashed on the wing. Three different velocities were investigated according to the following considerations. Firstly, based on (FAA, 2016), small UAVs are not permitted to be operated over 400 feet (approximate 120 m). Secondly, the maximum flight altitude of the above UAVs is restricted to be 500 m from the ground by DJI. Thirdly, (FAA, 1993) states that unless otherwise authorized by the Administrator, no person may operate an aircraft below 10,000 feet (approximate 3,000 m) MSL at an indicated airspeed of more than 250 knots. Therefore, three different velocities of aircraft

were 40 ms^{-1} at take-off (approximate 120 m), 62 ms^{-1} at approach (approximate 500 m), and 103 ms^{-1} at cruising conditions (approximate 3,000 m) are determined based on the flight envelope. The maximum flight speed of the drone was 18 ms^{-1} thus the impact velocities were 58 ms^{-1}, 80 ms^{-1}, and 121 ms^{-1}.

Figure 3-6 show the result summary of drone collision with velocity impact differences. It can be seen that at the velocity of 58 ms^{-1}, the skin is no fracture so that no drone component penetrated the structure of wing. At an impact velocity of 80 ms^{-1}, the drone broke the skin cause the maximum plastic strain exceeds the material failure strain, namely 18%. However, the front spar remained intact. At higher impact velocity, that is 121 ms^{-1}, the drone caused more fracture to the skin and damage to internal structures. The energy distribution is showed in chart form. At low impact velocity, the structural internal energy is higher than the impact velocity of 80 ms^{-1} and 121 ms^{-1}. Furthermore, the residual kinetic energy at the impact velocity of 58 ms^{-1} lower than the impact velocity of 80 ms^{-1} and 121 ms^{-1}. The drone's internal energy increases 180% when the kinetic energy was 4.35 times larger. At the impact velocities of 80 ms^{-1} and 121 ms^{-1}, the structural internal energy is lower than the impact velocities of 58 ms^{-1} because the structure failed at the initial impact so that no energy is absorbed by the deformation of the structure.

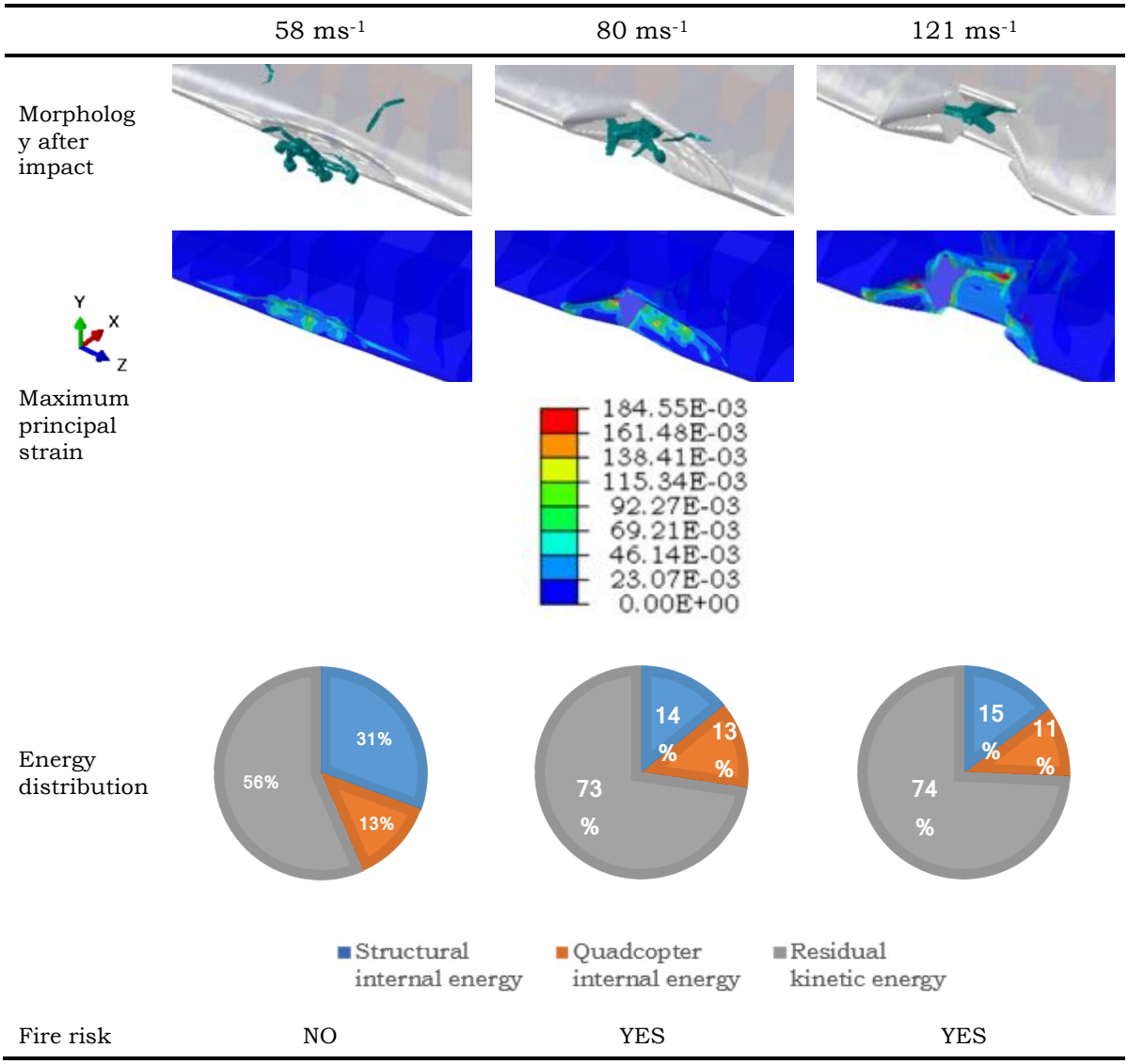

Figure 3-6: Summary chart of different drone velocities

According to the airworthiness standards, it can be assumed that at the impact velocity of 58 ms^{-1}, the aircraft could complete the flight. At the impact velocity of 80 ms^{-1}, the primary structure of the wing was not severely damaged, but the fire risk of the lithium-ion battery should be considered. However, at the impact velocity of 121 ms^{-1},

the front spar is subject to severe plastic deformation and the residual strength should be evaluated to ensure flight safety.

3.3. Comparison with a bird strike

3.3.1. Bird model

One of the methods to simulate bird was Smoothed Particle Hydrodynamics (SPH). The method was developed to overcome large mesh distortion in high-speed impact problems. Particles are nodes that connect each element obtained from the mesh. According to (Heimbs, 2011), SPH has the advantages in the accuracy and of the computation process. The same result was also obtained by (Liu et al., 2014) through a comparison between simulation results from Lagrangian and SPH model which is crashed on flat plates. (Hedayati & Ziaei-Rad, 2013) studied the effect of different bird geometries on impact results through the numerical method and obtained cylinder with hemispherical ends with a length to diameter ratio of 2 was recommended. As mentioned in Subsection 3.1, a bird with a mass of 910 g was adopted in this research based on (Republic Indonesia Ministry of Transportation, 2014). The average density of birds was 938 kgm^{-3} based on a report from (SIMULIA, 2011). The SPH bird model has 11,797 particles as shown in Figure 3-7. Note that this bird model is homogeneous that does not consider differences in bird organs such as muscles or bones and can only be used to predict the macro-response of the structure in bird strike simulations.

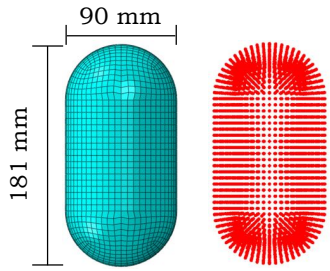

Figure 3-7: The SPH bird model

Hydrodynamics is described by the relationship of peak pressure to density ratio, known as the Equation of State (EOS) as shown in Figure 3-8. EOS considers fluid material variables, such as pressure, density, strain, and internal energy (Hedayati & Sadighi, 2015). Characteristic for bird materials during bird strike process has been investigated by (Barber & Wilbeck, 1987). (Smojver & Ivančević, 2012) employed different EOSs to study bird strikes on aircraft structures. The type of EOS used in this study is tabular based on (SIMULIA, 2011) which is formulated as follows:

$$p = f_1(\varepsilon_{vol}) + \rho_0 f_2(\varepsilon_{vol}) E_m \tag{3-1}$$

Where p and ρ_0 are the pressure and bird density at atmospheric pressure, $f_1(\varepsilon_{vol})$ and $f_2(\varepsilon_{vol})$ are the logarithmic functions of volumetric strain ε_{vol}, with $\varepsilon_{vol} = \ln(\rho_0/\rho)$, and E_m is the internal energy per unit mass. The contribution of internal energy to the pressure is usually neglected when dealing with the hydrodynamic impact. Therefore, $f_2(\varepsilon_{vol}) = 0$ and $p = f_1(\varepsilon_{vol})$. Real bird has a porosity between organs thus reducing the density which is the average density of birds ranges from 900-950 kgm^{-3} (Hedayati & Sadighi, 2015). Porosity has a significant effect on the resulting peak pressure. For example, a porosity of 0.1 can reduce peak pressures up to 50% compared to porosity of 0 (Wilbeck, 1978). In this study, a bird material with 0 porosity was employed to get conservative results. Parameters of 0 porosity are shown in Table 3-1.

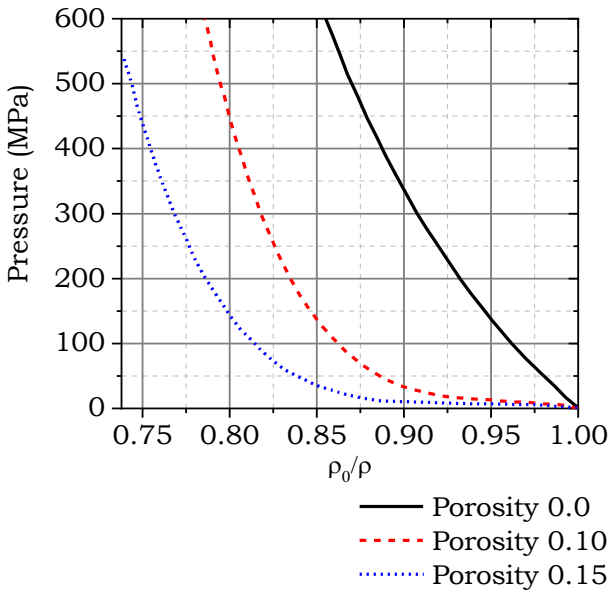

Figure 3-8: Hugoniot pressure of water-like homogenized bird materials (SIMULIA, 2011)

Table 3-1: Tabular EOS with 0% porosity parameters (SIMULIA, 2011)

No	f_1 (MPa)	ε_V	No	f_1 (MPa)	ε_V
1	0	0	14	263,29	-0,088
2	15,82	-0,007	15	289,34	-0,095
3	32,56	-0,014	16	315,39	-0,100
4	51,17	-0,021	17	342,37	-0,107
5	68,85	-0,028	18	370,29	-0,113
6	87,45	-0,035	19	399,13	-0,119
7	106,06	-0,042	20	429,83	-0,126
8	127,46	-0,049	21	460,53	-0,132
9	147,93	-0,055	22	493,09	-0,138
10	168,40	-0,062	23	526,59	-0,144
11	191,66	-0,068	24	561,01	-0,150
12	213,98	-0,075	25	595,43	-0,156
13	238,17	-0,081			

3.3.2. Result and discussion

The comparison between 735 g drone collision and 910 g bird strike is shown in Figure 3-9 (a) and 3-9 (b). The impact velocity was 80 ms^{-1} and the impact location was between ribs. During the bird strike process, the skin of the wing cut the bird body and the debris slid away from the structure, the skin suffered extensive permanent deformation but no penetration was observed. However, during the drone collision process, the drone broke the skin and penetrated the airframe, which may cause damage to the front spar. According to airworthiness standards, the drone collision was assumed to be more dangerous than a bird strike. Under the same impact velocity, the drone's kinetic energy was 81.1% of the bird's kinetic energy.

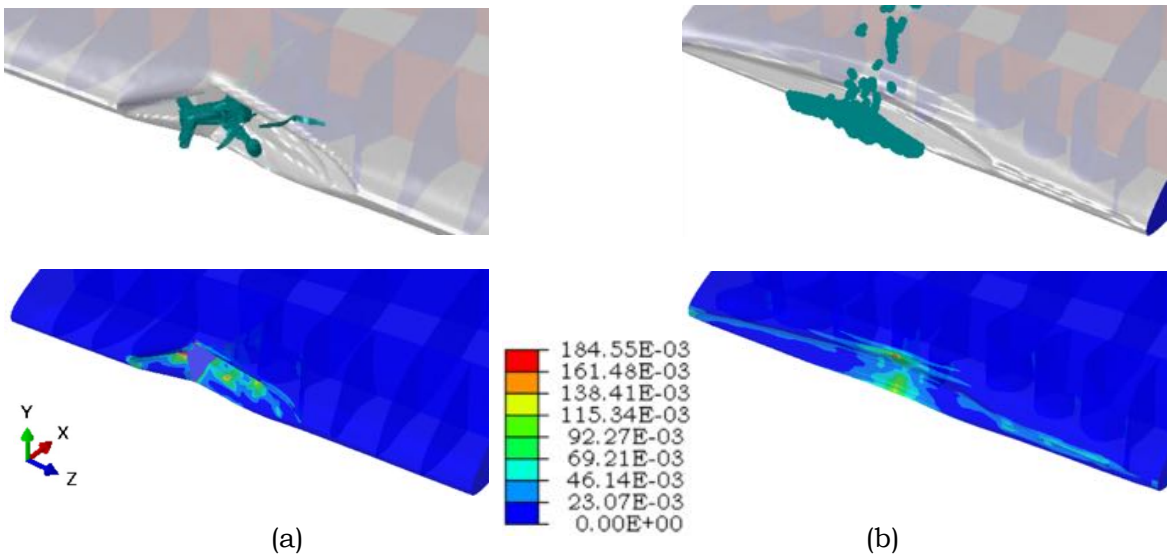

Figure 3-9: Damage characteristics of (a) drone collision and (b) bird strike

The impact level consequences between drone collision and bird strike can be considered for two reasons. First, the bird material was fluid-like would splash during the collision so that increasing the contact area and decrease impact loading. In other words, the stress distribution due to bird strikes is wider than the drone collision. In a bird strike problem, the energy absorbed by the deformation of the aircraft structure is 5.9% greater than that of a drone collision as shown in Figure 3-10 and the bird does not penetrate the aircraft structure. However, the drone component showed solid characteristics during the collision process. The impact load was more concentrated which is indicated by the maximum plastic strain only in the failure area. Additionally, the impact load caused a local fracture of the skin and then cause large penetration due to crack propagation. From the above discussion, it can be assumed that hardness plays an important role rather than kinetic energy which is the biggest difference between drone collisions and bird strikes.

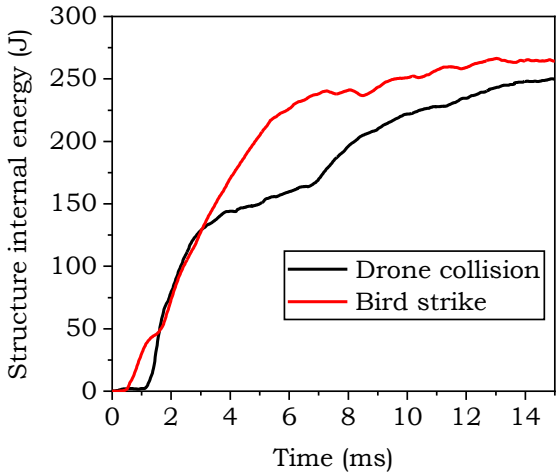

Figure 3-10: Aircraft structure internal energy

4. Conclusions

This research was performed to analyze drone and bird collision against aircraft commuter wing section. When a drone airborne collision occurs at the aircraft maximum approach flap speed and cruising speed, the commuter aircraft is in unairworthy condition. In other words, the commuter aircraft cannot complete the flight safely. This condition is caused by damage to the wing front spar and fire risk of the lithium-ion battery. The thickness of the skin, spar, and rib have been proven ineffective against drone airborne collisions so that increasing the thickness was needed. Drone collision

would cause more serious consequences than a bird strike at the same mass, the drone can easily penetrate the skin and cause damages to the primary structures of the aircraft. Therefore, relevant airworthiness standards should be drafted to ensure the safe operation of the aircraft.

Acknowledgments

This research was supported by Mr. Prio Adhi Setiawan as a Senior Advisor at the German Indonesian Association of Experts and Scholars. S

References

Barber, J. P., & Wilbeck, J. S. (1987). *Bird impact loading. The Shock and vibration bulletin Part 2. 48*.

Dar, U. A., Zhang, W., & Xu, Y. (2013). FE analysis of dynamic response of aircraft windshield against bird impact. *International Journal of Aerospace Engineering*, *2013*. https://doi.org/10.1155/2013/171768

FAA. (1993). *FAR 91.117 Aircraft speed. 18334*.

FAA. (2016). Small Unmanned Aircraft Systems (sUAS) Part 017. *Area*, *January*, 1–4.

Hedayati, R., & Sadighi, M. (2015). Bird Strike: An Experimental, Theoretical and Numerical Investigation. In *Woodhead Publishing*. https://doi.org/10.1016/C2014-0-02336-2

Hedayati, R., & Ziaei-Rad, S. (2013). A new bird model and the effect of bird geometry in impacts from various orientations. *Aerospace Science and Technology*, *28*, 9–20. https://doi.org/10.1016/j.ast.2012.09.002

Heimbs, S. (2011). Computational Methods for Bird Strike Simulations: A Review. *Computers and Structures*, *89*(23–24), 2093–2112. https://doi.org/10.1016/j.compstruc.2011.08.007

Jenkins, D., & Vasigh, B. (2013). The Economic Impact of Unmanned Aircraft Systems Integration in the United States. In *Association for Unmanned Vehicle Systems International*.

Liu, J., Li, Y., & Gao, X. (2014). Bird strike on a flat plate: Experiments and numerical simulations. *International Journal of Impact Engineering*. https://doi.org/10.1016/j.ijimpeng.2014.03.006

Lu, X., Liu, X., Li, Y., Zhang, Y., & Zuo, H. (2020). Simulations of airborne collisions between drones and an aircraft windshield. *Aerospace Science and Technology*. https://doi.org/10.1016/j.ast.2020.105713

Meng, X., Sun, Y., Yu, J., Tang, Z., Liu, J., Suo, T., & Li, Y. (2019). Dynamic response of the horizontal stabilizer during UAS airborne collision. *International Journal of Impact Engineering*. https://doi.org/10.1016/j.ijimpeng.2018.11.015

Millan, R. M., von Steiger, R., Ariel, M., Bartalev, S., Borgeaud, M., Campagnola, S., Castillo-Rogez, J. C., Fléron, R., Gass, V., Gregorio, A., Klumpar, D. M., Lal, B., Macdonald, M., Uk Park, J., Sambasiva Rao, V., Schilling, K., Stephens, G., Title, A. M., & Wu, J. (2019). Small Satellites for Space Science. *Advances in Space Research*. https://doi.org/10.1016/j.asr.2019.07.035

Republic Indonesia Ministry of Transportation. (2014). *Civil Aviation Safety Regulation Part 23 amdt1 Airworthiness Standard: Normal, Utility, Acrobatic, and Commuter Category Airplanes*. 1–272.

Sahraei, E., Hill, R., & Wierzbicki, T. (2012). Calibration and finite element simulation of pouch lithium-ion batteries for mechanical integrity. *Journal of Power Sources*. https://doi.org/10.1016/j.jpowsour.2011.10.094

Sahraei, E., Meier, J., & Wierzbicki, T. (2014). Characterizing and modeling mechanical properties and onset of short circuit for three types of lithium-ion pouch cells. *Journal of Power Sources*. https://doi.org/10.1016/j.jpowsour.2013.08.056

Schroederi, K., Song, Y., Horton, B., & Bayandor, J. (2017). Investigation of UAS ingestion into high-bypass engines, Part II: Drone parametric study. *58th AIAA/ASCE/AHS/ASC Structures, Structural Dynamics, and Materials Conference, 2017*.

SIMULIA. (2011). *A Strategy for Bird Strike Simulations using Abaqus / Explicit* (Issue Dassault Systems Online Support Document, Answer ID-4493 (Best Practices for Bird Strike Analysis)).

Smojver, I., & Ivančević, D. (2012). Advanced modelling of bird strike on high lift devices

using hybrid Eulerian-Lagrangian formulation. *Aerospace Science and Technology*. https://doi.org/10.1016/j.ast.2011.07.010

Song, Y., Horton, B., & Bayandor, J. (2017). Investigation of UAS ingestion into high-bypass engines, Part I: Bird vs. drone. *58th AIAA/ASCE/AHS/ASC Structures, Structural Dynamics, and Materials Conference, 2017*. https://doi.org/10.2514/6.2017-0186

Waqas, H. M., Shi, D., Imran, M., Khan, S. Z., Tong, L., e Ahad, F., Zaidi, A. A., Iqbal, J., & Ahmed, W. (2019). Conceptual design of composite sandwich structure submarine radome. *Materials*. https://doi.org/10.3390/ma12121966

Wilbeck, J. S. (1978). *Impact Behavior of Low Strength Projectiles. Technical Report AFML-TR-77-134. Air Force Materials Laboratory. Wright-Patterson Air Force Base*, *Ohio*, *45433*, *USA*.

.

Research on the Transmissibility of Wire Rope Insulators as Damping Equipment on the RX 200 Rocket Payload

Agus Budi Djatmiko[1] , Ediwan, Ronald[1], Gunawan Putra[1]

[1]Rocket Technology Center, National Institute of Aeronautics and Space (LAPAN), Indonesia

e-mail: agusbudi60@gmail.com

Received: 07-03-2021. Accepted: 22-04-2021. Published: 30-06-2021

Abstract

Wire rope insulator or steel wire rope insulator has applications for vibration isolation in equipment and structures in many industrial machinery. Steel wire rope insulators can also be used as suitable equipment to dampen vibrations in rocket loads. The disturbance acceleration as the excitation caused by the combustion process on the rocket can cause a vibration with a large amplitude which results in damage to the rocket's payload structure and the electronic equipment on the rocket's payload cannot work as desired. Based on the experience of electronic equipment, it will be damaged if the disturbance acceleration of 3 g acting on the rocket is not reduced, for this reason a vibration damping device is designed, the apparatus consists of several stainless steel wire ropes tied between two parallel binders arranged in such a way as to provides a damping effect on the rocket's payload. A wire rope insulator consists of several stainless steel wire ropes tied between two parallel straps. One application of this type of wire rope insulator is to isolate the vibrations that occur in the rocket, so that it does not interfere with the performance of the electronic equipment on the rocket's payload. Electronic equipment is used to determine the position of the rocket and its stability. In this study, the wire rope material used is stainless steel with σ_{yield} = 350 e+6 N / m2 with a diameter of d = 3 mm.

The research objective of the vibratory damper of wire rope insulators was to determine the magnitude of the transmissibility of the ruffler during and after resonance. Transmissibility (TR) is the ratio of the force transmitted to the disturbing or excitation force.

The results of the research on a damper with a disturbance acceleration of 3 g at resonance ($\omega/\omega_n = 1$), obtained the transmissibility value (TR) = 2.54, the spring stiffness k = 200537.3 N/m and the damping coefficient c = 331.5 N/m/sec, then after conditions $\omega/\omega_n = 2.38$ obtained transmissibility (TR) <1 This shows that the damper with steel wire isolator is good enough to dampen vibrations in the RX 200 rocket payload.

Keywords: *Wire rope isolator, Resonance, Transmissibility*

Nomenclature

m	=	mass of payload, kg
k	=	isolator vibration stiffness, N/m
c	=	wire rope damping coefficient, N/m/s
Fo	=	the excitation force of the rocket, N
F_T	=	force transmitted by rocket payload, N
kx	=	force of compression, (N)
x	=	the deviation from the equilibrium position, m
TR	=	Transmissibility
A_0	=	acceleration of disturbance (m / sec2)
A_T	=	the acceleration transmitted to the rocket's payload (m / sec2)
ω	=	frequency of work of rocket (rad / second)
ξ	=	damping factor
ω_n	=	natural frequency (rad / second)

$m\ddot{x}$ = inertia force, (N)
$c\dot{x}$ = damping force (N)

1. Introduction

Vibration becomes intolerable, the isolation system is applied to cut off the path of the vibration to enhance the safety of the receiver. A general isolation system has two main components namely, Stiffness (K) and Damping (C) Firstly, the stiffness of the isolation system provides the restoring force and also influences the natural frequency of the isolated system. The lower value of transmissibility can be achieved by decreasing the stiffness which results in shifting the natural frequency of the system to a lower value (Balaji et al., 2016)(Ledezma-Ramirez et al., 2016). Secondly, the damping component of the isolator enables the energy dissipation of the external excitation to suppress it. The amount of damping required is subjective and varies with respect to applications. Vibrations and shocks are studied using various techniques and analyzed to predict their detrimental effect on the equipment and structures. In many cases, the vibrations are unavoidable, but it will be within tolerable limits. In other cases, where the vibration becomes intolerable, it is required to analyse the system for the effects of vibrations and improve the mechanical properties or in a place where are system design restricted in improving mechanical properties, it is then required to add an isolation system to counter the vibrations (Ledezma-Ramirez et al., 2012)(Balaji et al., 2015). The application of vibration isolation system requires an understanding of the vibration control components, namely, source, path and receiver of the vibration (Balaji et al., 2016)(Ledezma-Ramirez et al.,2016).

Vibration is undesirable in many domains, especially engineering systems such as vibrations in rocket payloads and methods have been developed to prevent the transfer of vibrations to such systems (Voss et al., 2009). In other cases, where the vibration becomes intolerable, the isolation system is applied to cut off the path of the vibration to enhance the safety of the receiver (Balaji et al., 2015)(S. Pagano & S. Strano, 2013). A general isolation system has two main components namely, Stiffness (K) and Damping (C) (Ledezma-Ramirez et al., 2014)(Rao, 2007). Firstly, the stiffness of the isolation system provides the restoring force and also influences the natural frequency of the isolated system. The lower value of transmissibility can be achieved by decreasing the stiffness, which results in shifting the natural frequency of the system to a lower value (Puff et al., 2015). Over the past few years, many variant and isolating devices have been designed to reduce vibration or isolate structures from unwanted vibrational energy. Among these devices, wire rope insulators are noted for their high performance in vibration and shock isolation. They have found many insulation applications in aerospace systems and other sensitive equipment. One application of this type of wire rope insulator is to isolate the vibrations of electronic equipment present in the rocket's payload(Voss et al., 2009)(Rao, 2007)

Wire Rope Isolators (WRI), an elastic stiffness and damping, has become the subject Passive systems are of two types, linear and nonlinear system. The linear systems earlier developed displacement relation, and they are effective only when less than the external excitation frequency. However, in the cases such as low frequency vibrations which can the linear isolation system limitations can be overcome using vibration isolators and comprehensive survey of recent n which many cited stiffness are of great benefit in vibration linear behavior in both Passive systems are of two types, linear and nonlinear system. The linear systems were earlier developed behavior in force-displacement relation, and they are effective only when less than the external excitation frequency. However, in the cases such as motions, shocks or impact loads, there can be low frequency vibrations s. However, the linear isolation system limitations can be overcome using Several authors have developed different types of nonlinear vibration isolators and investigated the unique dynamic behaviors (Ledezma-Ramirez et al.,2016) (Patent, 2014).

A wire rope insulator consists of several stainless steel wire ropes tied between two parallel straps. Due to the shear friction between the wire strands and the internal friction of the cable, the insulator exhibits nonlinear hysteresis behavior. Apart from mechanical damping characteristics in the three main directions, they have other advantages such as attenuating strong shocks, aging and thermal insensitivity as well as low cost. For the purpose of predicting the vibration response and for better use and

design of insulation systems with wire rope insulators, it is necessary to accurately identify their hysteresis restoring strength under static and dynamic loads. (Ledezma-Ramirez et al.,2016)(Balaji et al., 2015)(ITT Enidine Inc, 2014).

2. Methodology

The research was started from the design of the device, looking for the disturbance acceleration data, the damping factor, then the equation of motion analysis of the vibration damper. After that, determine the magnitude of the squeezing constant k (N / m). After that, look for the vibration transmissibility equation to determine the magnitude of the acceleration transmitted to the rocket's load, and finally the research on the transmissibility of the vibration damper on the RX 200 rocket charge at the time of resonance.

The research was conducted at the Vibration Test Laboratory at the LAPAN Ranca Bungur Satellite Technology Center, Bogor.

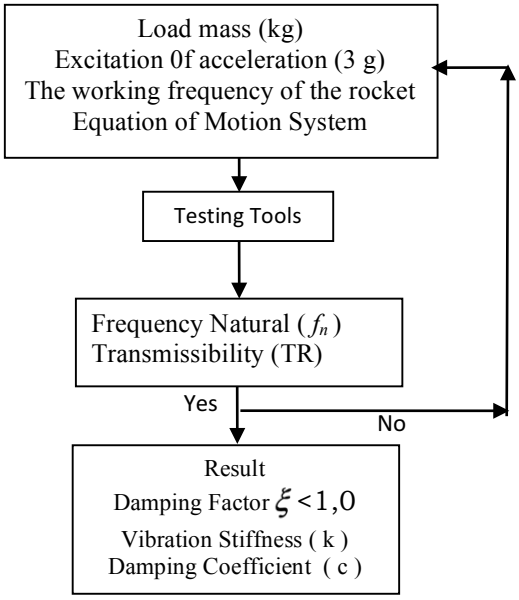

Figure 2-1: Flow chart of vibration damper testing

2. 1. Problem Definitions

The phenomenon of vibration occurs at the time of rocket's flight. This will cause problems in the body and systems that exist in the rocket due to the forces that arise due to the vibration phenomenon. This should be a concern because if left unchecked, the rocket will fail not only in its electronic system, but also in its structure, indeed the rocket must have a vibration insulator system that will dampen the forces acting on the vibration phenomenon.

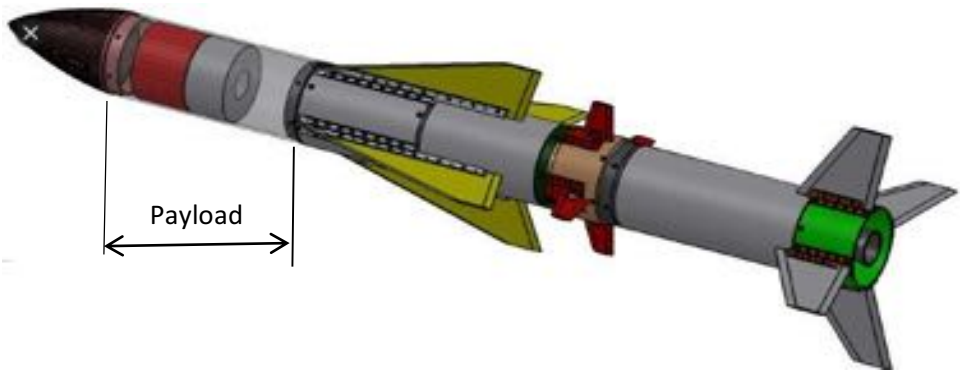

Figure 2-2: Rocket RX 200

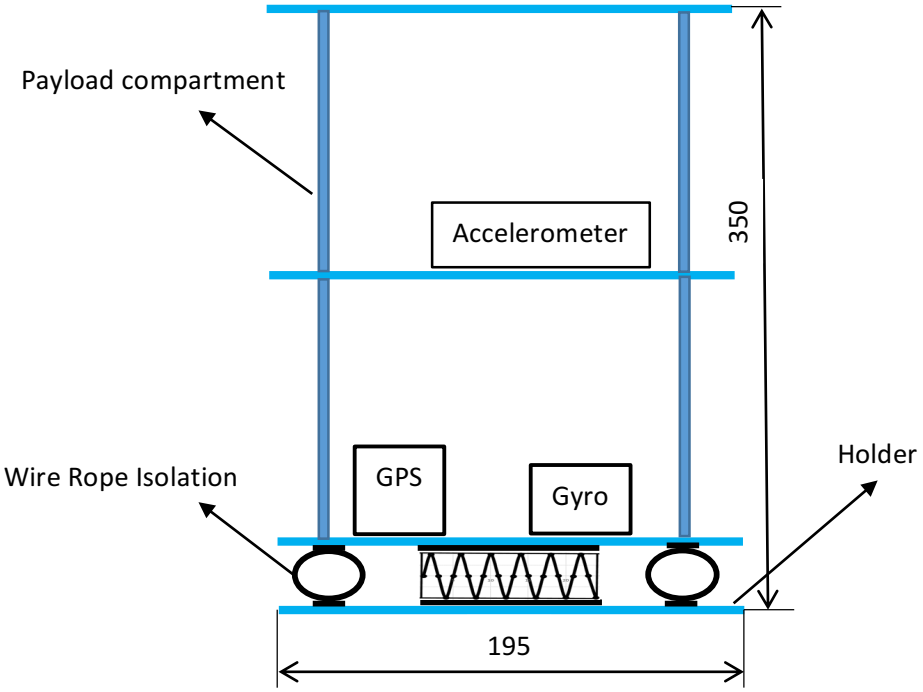

Figure 2-3: Payload System

2. 2. Method

The system is simplified as vibrational elements, namely mass, stiffness, and damping which are analogous to the mass of the object, spring, and damper, then the equation of motion of the rocket system is determined which is derived from all the elements in the rocket system. From this equation of motion, an important characteristic of the vibration system will be obtained, namely the damping factor and transmissibility (Rao, 2007).

3. Result and Analysis

The motion equation for the vibration dampening system model in Figure 2-3 is:

$$m\ddot{x} + c\dot{x} + kx = F_o(t) \tag{3-1}$$

$$-m\omega^2 X + c\omega X + kX = F_o \tag{3-2}$$

$$X = \frac{F_o/k}{\sqrt{\left[1-\left(\frac{\omega}{\omega_n}\right)^2\right]^2 + \left(2\xi\frac{\omega}{\omega_n}\right)^2}} \tag{3-3}$$

The solution to the equation is F_o (t) = 0. where the equation will give an understanding of the role of damping with the homogeneous equation.

The force that passes the load through the springs and dampers is

$$F_T = \sqrt{(kX)^2 + (c\omega X)^2} \tag{3-4}$$

And the excitation or disturbance force F_o of the rocket in the force balance system in the rocket charge suppressor system is given by the following equation:

$$F_0 = \sqrt{(kX - m\omega^2 X)^2 + (c\omega X)^2} \tag{3-5}$$

Finally transmissibility (TR) can be determined as

$$\frac{A_t}{A_O} = TR = \frac{\sqrt{1 + \left(2\zeta \frac{\omega}{\omega_n}\right)^2}}{\sqrt{\left[1 - \left(\frac{\omega}{\omega_n}\right)^2\right]^2 + \left[2\zeta \frac{\omega}{\omega_n}\right]^2}} \tag{3-6}$$

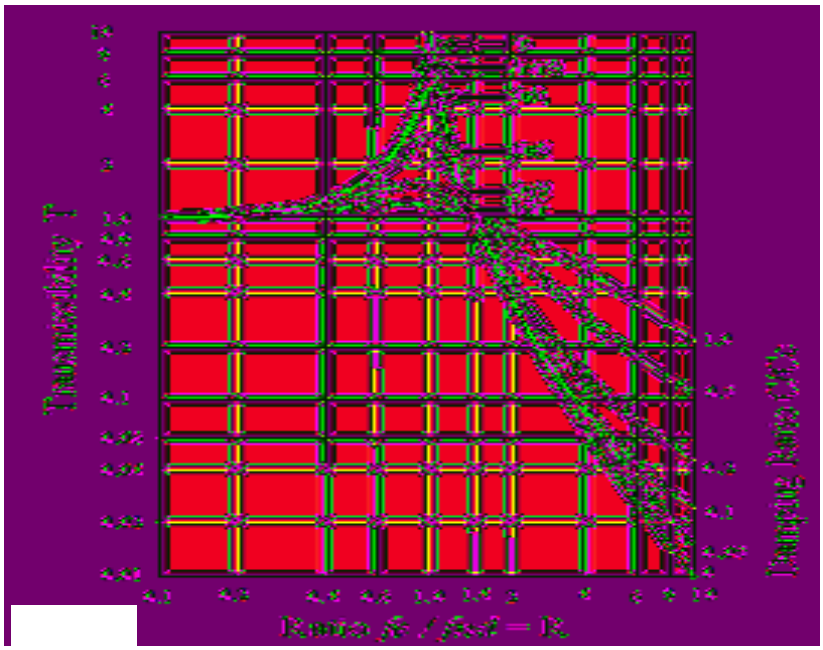

Figure 3-1: The relationship between transmissibility to the frequency ratio (Rao, 2007).

Figure 3-2: Wire Rope Isolation

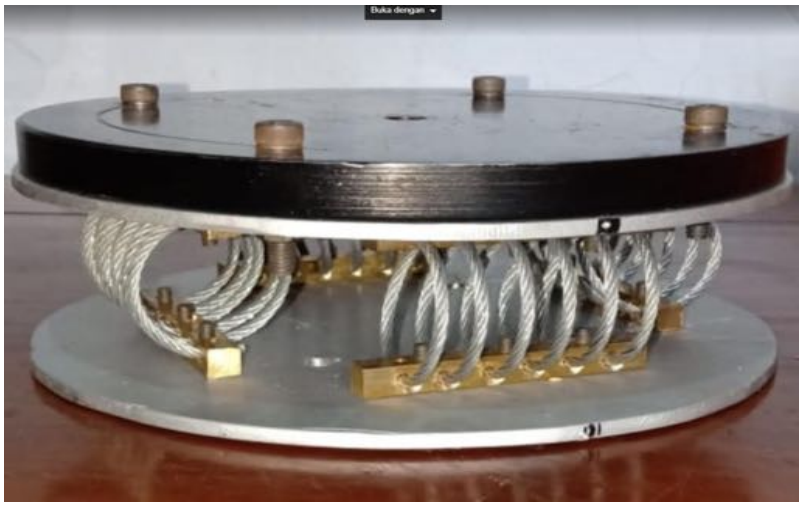

Figure 3-4: Wire Rope Isolation of RX 200 LAPAN Payload

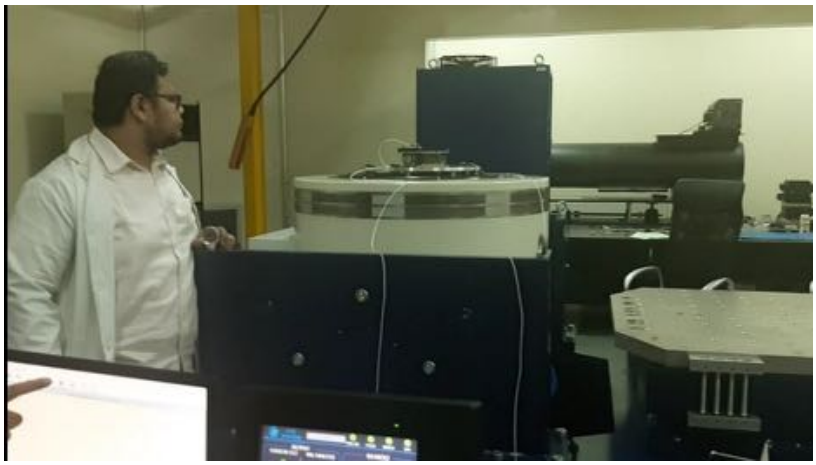

Figure 3-5: Testing of Wire Rope Isolation of RX 200 LAPAN Payload

Research data :
Wire rope diameter, dr = 3 mm
Wire rope circle diameter, dl = 30 mm
Material: Stainless steel wire rope with σ_{yield} = 350 e6 N / m2.
Load m = 2.8 kg
G force = 3 g

Table 3-1: Vibration Testing Result

f_n	G_O			G_T		TR
43.9207	3	3.02223	3.02233	7.68886	1.000033088	2.544101541
44.0485	3	3.02251	3.0224	7.70078	0.999963606	2.547809602
105.33	3	3.00949	3.00951	3.01184	1.000006646	1.000780863
105.637	3	3.01005	3.01006	3.001	1.000003322	0.996993405
105.944	3	3.01017	3.01016	2.9903	0.999996678	0.993399044

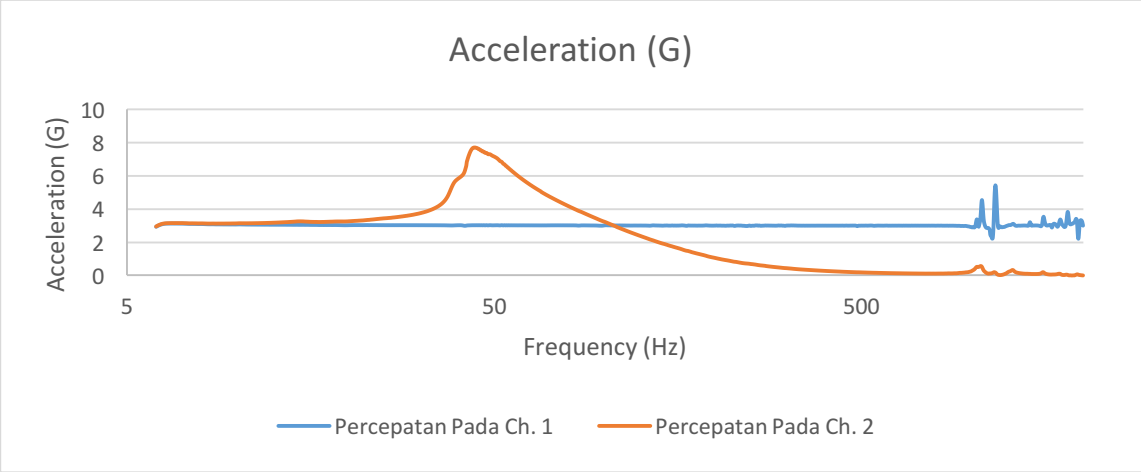

Figure 3-6: Natural Wire Rope Isolation RX 200 Frequency Testing Graph

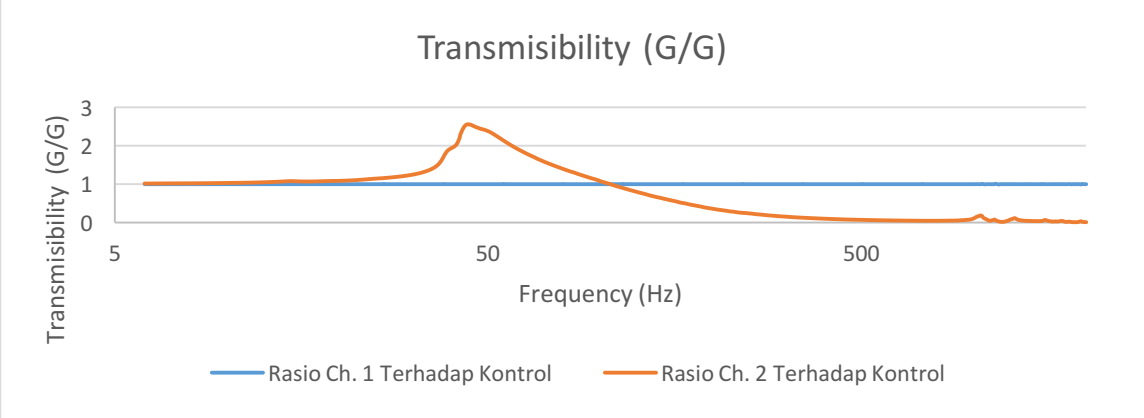

Figure 3-7: Transmissibility Wire Rope Isolation RX 200 Testing Graph

Table 3-2: Test results and calculations for wire rope isolation

Properties	Value (unit)
Natural Frequency (f_n)	44,485 Hz
Transmissibility Resonance (TR)	2,54
Viscous Damping Ratio (ξ)	0,214
Damping Coefficient (c)	331,5 (N/m/second),
Isolator Vibration Stiffness (k)	200537,3 (N/m)
Critical Damping (c_c)	1549, (N/m/second),

4. Conclusions

From the test results of wire rope isolation as a vibration dampening device on the RX 200 rocket load, it can be said to be quite satisfying because at the time of resonance where the transmissibility of TR = 2.54, the vibration dampening device can work as desired and does not experience damage and the wire rope isolation shows as a good damper after a frequency of 105.637 Hz, has a transmissivity (TR) smaller than one. In addition, wire rope isolation on the RX 200 rocket load also has a damping factor ξ = 0.214, which is fulfilled as a clamp tool because ξ <1 (under-damped system)

Acknowledgements

With the completion of this research, I as the author would like to thank the Head of LAPAN Rocket Technology Center and the Leader of Engineering Structures.

Contributorship Statement

Agus Budi Djatmiko developed the simulation, designed the method, analyzed the results, Ediwan and Ronald G.P. prepared the testing method and manuscript.

References

Palani S. Balaji, Moussa Leblouba, Muhammad E. Rahman & Lau Hieng Ho. (2016) Static lateral stiffness of wire rope isolators. International Journal of Mechanic Based Design of Structur and Machine, Volume 44, 2016- Issue 4

Diego Francisco Ledezma-Ramirez, Fernando Javier Elizondo-Garza, Pablo Ernesto Tapia-Gonzalez, Adrian García-Mederez. (2016) Experimental characterization of dry friction isolators for shock vibration isolation. PROCEEDINGS of the 22nd International Congress on Acoustics Buenos Aires – 5 to 9 September

Ledezma, D.F., Ferguson, N.S., Brennan, M.J. (2012) An experimental switchable stiffness device for shock isolation, Journal of Sound and Vibration, Vol. 331, No. 23, pp. 4987-5001.

P.S.Balaji1,M.E.Rahaman , Leboula Moussa, Lau Hieng Ho. (2015) Vibration isolation of structures and equipment using Wire rope isolators. International Journal of Modern Trends in Engineering and Research (www.ijmter.com)-ISSN No.:2349-9745

S. Pagano and S. Strano. (2013) Wire rope springs for passive vibration control of a light steel structure. WSEAS Transactions on Applied and Theoretical Mechanics, vol. 8, pp. 212-221

M. Puff, A. Kopanoudis, A. v. Seck & S. Ruan ITT Control Technologies EMEA GmbH, Germany 2Siemens AG, Germany ITT Enidine Inc., USA (2015). Introduction of an innovative base isolation system for seismic protection of HV components based on a combination of wire ropes and viscous dampers" WIT Transactions on The Built Environment, Vol 152, WIT Press

Patent no.: 2014E03763 DE/2014P20533 US. (2014) Invention: Standard Base Isolation System for single supported HV Components based on a combined arrangement of wire rope and viscous dampers through the example of 3AP3 Circuit Breaker base isolation, New Zealand Pole3 project

Wire rope Isolators.2014. ITT Enidine Inc, New York, www.enidine.com

Luke Voss, Tony Allais, Sean King, Jeff Parkins., (2009) Plans and Specifications of A Suborbital Rocket Payload. AKPV Engineering University of Wyoming

Rao S.S, 2007. *Vibration of Continuous Systems.* Jhon Wiley & Sons Publishing Company, Published Online: 23 MAR 2007 Print ISBN: 9780471771715

Effects of Bleeder Schedule to Fiber Mass Fraction and Composites Surface Topography on Wet Lay-up Manufacturing Process

Wiwiek Utami Dewi[1], Rizky Sutrisna[1], Sutrisno[1]

[1] Rocket Technology Center, National Institute of Aeronautics and Space (LAPAN), Indonesia

e-mail: wiwiek.utami@lapan.go.id

Received: 23-03-2021. Accepted: 22-04-2021. Published: 30-06-2021

Abstract

The thermal protector materials of the rocket's motor are made by a wet lay-up manufacturing process. Since the fiber mass fraction of the product is low, several experiments have been conducted to solve this problem including changing the type of the epoxy resin and selecting the most suitable bleeder schedule. Bleeder cloth application results in increasing the fiber mass fraction. The fiber mass fraction of thermal protector material manufactured by hand lay-up can reach a maximum of 56.78%, whereas vacuum bagging can reach a maximum of 66.43%. Peel ply and breather fabric combination are the best bleeder schedule for the hand lay-up method meanwhile perforated release film and breather fabric are the best bleeders for the vacuum bagging method. Composite surface topography obtained from peel ply is visible on the surface. The imprints of the nylon peel ply weave are visible through SEM analysis. Meanwhile, the surface topography obtained from the perforated release film is not visible. The vacuum bagging method helped reduce the number of voids and ductile polymer fractures from the composite surface. This paper recommends peel ply usage in the thermal protector manufacturing process to replace the sanding or filling method that the author use nowadays.

Keywords: *thermal protector material, bleeder schedule, fiber mass fraction, SEM analysis, peel ply.*

Nomenclature

X_f	=	fiber mass fraction
m_f	=	fiber mass, g
m_t	=	composite total mass, g
A_f	=	fiber area, cm^2
F_{aw}	=	fiber areal weight, $^{g}/_{cm^2}$

1. Introduction

LAPAN's rocket motor thermal protector materials are made of fiberglass and fiber carbon epoxy composites. The materials are manufactured by the wet lay-up process. Wet lay-up is a method of making a reinforced product by applying a liquid resin system while or after the reinforcement is put in place (U.S. Departement of Defense, 2002). The resin and fiber are applied to the working surface by hand. The fiber mass fraction of the composites product made by wet lay-up is low (less than 50%). The thermal protector materials are rich in polymer resin. Experiments are conducted to increase the fiber mass fraction. Since the manufacturing process cannot be replaced, there are efforts to replace the type of epoxy resin and to apply the bleeder cloth during the manufacturing process. Change in the type of epoxy will be described in another work. This work is focused on the bleeder type effect on the fiber fraction and composite surface laminate.

Bleeder cloth is a nonstructural layer of material used in the manufacture of composite parts to allow the escape of excess gas and resin during cure. The bleeder cloth is removed after the curing process and is not part of the final composite (U.S. Departement of Defense, 2002). During the manufacturing process, the excess polymer resins are adsorbed by the bleeder cloth, increasing the fiber fraction of the composites product.

There are many types of bleeder: peel ply fabric, perforated release film, woven fabric, breather fabric, etc. Peel ply and perforated release film are often used as the first bleeder facing the laminates. Woven fabric and breather fabric are put upon the peel ply or perforated release film. Peel ply, the most popular one, is an extra layer of fabric material that is laid upon the outer surface of the composite during fabrication (Raymond F. Wegman, 2013). Peel ply fabric is usually made of nylon or polyester. Meanwhile, the perforated release film is a thin layer of plastic film with pores to control the flow of the excess resin during the early stages of the curing process. Perforated release films are made of polyethylene or HDPE. Peel ply can adsorb the excess resin but the perforated release film cannot. Therefore, the difference between bleeder properties gives a unique texture to the surface of the laminates.

2. Methodology

2.1. Related Works

The optimization of the lining system for solid rocket motors has been conducted multiple times. Sutrisno in 2011 and Wiwiek Utami Dewi in 2014 have addressed this issue in the papers related to the lining process of the RX1220 rocket motor. Sanding is the method used to prepare the surface of thermal protector material for the lining process (Dewi, 2014). This paper also describes the change of the epoxy resin type to optimize the lining process but did not provide further discussion on fiber fraction. Jeswani and Roux in 2010 have investigated the correlation of fiber volume fraction and resin viscosity. The paper stated that complete wet out of the dry fiber reinforcement by the liquid resin depends strongly on the fiber volume fraction and the resin viscosity.

Similar research was conducted by Abdurohman et al. in 2018. The author made a comparison between hand lay-up, vacuum bagging, and vacuum infusion towards e-glass epoxy composite. The author found that the hand lay-up method resulted in a 61% fiber mass fraction, while the vacuum bagging resulted in a 73% fiber mass fraction. Recent research to improve laminate quality in wet lay-up/vacuum bagging process by magnet assisted composite manufacturing (MACM) has been conducted by Mehrad Amirkhosravi et al. in 2017. The paper stated that laminate quality successfully improved the fiber volume fraction. The fiber volume fraction increased more than 55% from 17% to 27% and void content decreased by 53% to under 3% compared to the laminates made without magnetic pressure.

Flinn (2007) has investigated the influence of peel ply type on adhesive bonding on composite. The fracture path during removal of peel ply has a strong effect on the quality of the bond. Peel ply remnants on the substrate surface were shown to be detrimental to bond quality. Flinn performed the surface topography analysis by SEM. Studies on the influence of surface treatment type, in the effectiveness of structural adhesive bonding, for carbon fiber reinforced composites have been conducted by Martínez-Landeros et al (2019). The paper correlates the effectiveness of surface preparation type (pre-bonding), such as solvent cleaning, sanding (mechanical abrade), chemical etching (alkaline and acid), and peeling of the sacrificial surface layer (peel ply) of carbon fiber reinforced composite (CFRC) test specimens, with the corresponding effect to the final strength of adhesive bonding. It was performed using several techniques including SEM. Flinn (2005), Kanerva and Saarela (2013), Wegman and Van Twisk (2013) and Holtmannspotter et al. (2013) also conducted similar research.

2.2. Problem Definition

When manufacturing thermal protector materials, fiberglass and fiber carbon are impregnated with epoxy resin. The fiber is laid down one layer at a time and the epoxy resin is poured on and spread with a roller or a squeegee. Multiple layers are often required to achieve the designated thickness. The fraction of fiber reinforcement is very important in determining the mechanical and thermal properties of the composite.

Higher fiber fraction provides better mechanical strength. Fiber mass fraction in typical thermal protector material manufactured by wet lay-up is low (less than 50%). Bleeder cloth then added to adsorbs the excess resin. Bleeder schedule affects the fiber fraction of composites because it provides different adsorption ability.

The surface of the thermal protector material must be fairly rough to provide better bonding with the liner layer in the rocket motor. Sanding and filing are the common method used to prepare the thermal protector material for the lining process. The sanding or filing method has some disadvantages: (1) the surface is too large so it requires more working time, (2) it results in non-uniform roughness since it is manually applied by hand, (3) the abrasive work changes the thickness of the thermal protector material, (4) the excess fiber particulate becomes airborne during sanding. It can get stuck in the lungs. It is better to eliminate the exposure.

The application of bleeder cloth is not only to adsorbs excess resin but also to gives better surface preparation. It increases efficiency since it does not require more surface preparation work. The laminates surface will be fairly rough after bleeder cloth removal. The effect of bleeder cloth on the laminates surface were investigated by preparing laminates with peel ply and perforated release film.

2.3. Method

Thermal protector material samples are made of fiberglass and fiber carbon composite. Epoxy resin is used as the matrix. It is manufactured by wet lay-up and wet vacuum bagging methods. The specifications of the material are shown in Table 2-1.

Table 2-1: Material Specifications

No	Materials	Specifications
1	Epoxy A	Epoxy Bisphenol A. Justus Kimia Raya
2	Hardener EPH 555	Hardener Cycloaliphatic Amine. Justus Kimia Raya.
3	LP3	Liquid Polysulfide LP3. Morton Thiokol USA.
4	Fiber Glass Cloth	E-Glass. Twill Weave. Thickness 0,22 mm ± 10%. Fiber areal weight (FAW) 200 g/m^2. Density 1 gr/cm^3.
5	Fiber Carbon	Plain Weave, Carbon 3K. Density 1,78 g/cm^3. Tensile Strength 3310 MPa. Tensile Modulus 240 GPa. Fiber areal weight (FAW) 220 g/cm^3
6	Peel Ply	Nylon. FAW 85 g/m^2. Justus Kimia Raya
7	Breather Ply	Polyester non-woven. White. FAW 150 g/m^2. Width 1500 mm. Heat resistance up to 200^{o}C. Justus Kimia Raya.
8	Perforated Release Film	Polyethylene with small pores. Thickness 40 micron. Width 1500 mm. Justus Kimia Raya.

In this study, 9 samples of composite material made by different bleeder schedules. Sample 1 was manufactured without bleeder cloth. Sample 2 - 5 were manufactured by hand lay-up. Meanwhile, samples 6 - 9 were manufactured by vacuum bagging. Vacuum bagging was applied to provide better suction for the excess resin to escape. The mold was a working table, topped with 1 cm thick tempered glass. The tempered glass was coated with a Frekote 700-NC release agent. The composite samples were cured at room temperature for 24 hours. The room temperature was 23^{o}C – 25^{o}C with humidity 75% - 78%. Thermal protector material samples are presented in Table 2-2 and the vacuum bagging method is presented in Figure 2-1.

Table 2-2: Thermal Protector Material Samples

Sample Name	Resin Compositions (% wt.)	Bleeder Schedules
Sample 1B	Epoxy A: EPH555 : LP3 = 50% : 25% : 25%	No Bleeder
Sample 2B		Peel Ply Nylon + Fiberglass
Sample 3B		Peel Ply Nylon + Breather Fabric
Sample 4B		Perforated Release Film + Fiberglass
Sample 5B		Perforated Release Film + Breather Fabric
Sample 6B		Peel Ply Nylon + Fiberglass + Vacuum
Sample 7B		Peel Ply Nylon + Breather Fabric + Vacuum
Sample 8B		Perforated Release Film + Fiberglass + Vacuum
Sample 9B		Perforated Release Film + Breather Fabric + Vacuum

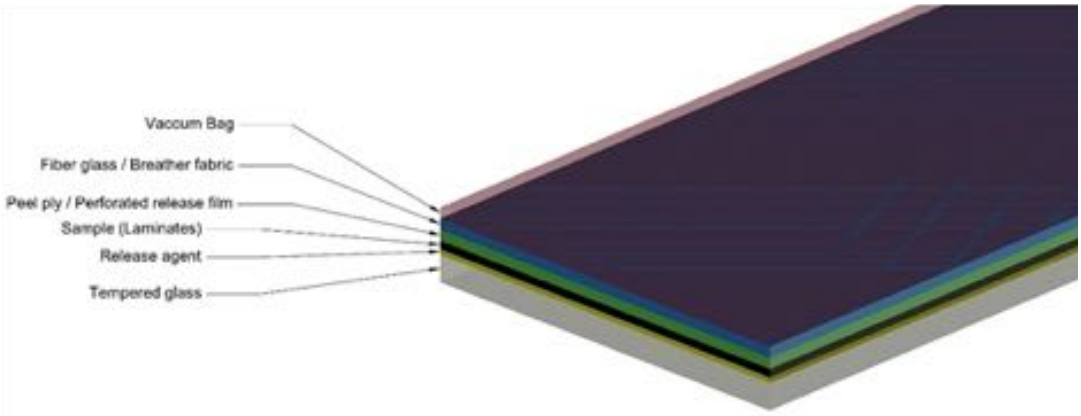

Figure 2-1: Arrangement in Vacuum Bagging Method

The fiber mass fractions were determined by eq. 2-1.

$$X_f = {}^{m_f}/_{m_t} \tag{2-1}$$

and

$$m_f = A_f \times F_{aw} \tag{2-2}$$

According to Table 2-1, the fiber areal weight (F_{aw}) of fiberglass is 200 gr/m^2 and F_{aw} of fiber carbon is 220 gr/m^2.

When the composites cured, the bleeder is removed and the samples were trimmed to provide a uniform area. The total mass of the samples is obtained from weighing the trimmed samples. The topography of the laminate surfaces was analyzed after bleeder removal through scanning electron microscopy (SEM). The SEM was Mini-SEM Phenom World. The viscosity of the epoxy resin was measured by Brookfield DVII+ Pro viscometer.

3. Result and Analysis

The viscosity of the epoxy resin is 451 – 472 cp. The fiber mass fraction of the thermal protector samples are shown in Tables 3-1 below.

Table 3-1: Fiber Fraction of Thermal Protector Samples

Sample Name	Bleeder Schedules	Fiber Mass Fraction
Sample 1B	No Bleeder	56.27%
Sample 2B	Peel Ply Nylon + Fiberglass	56.14%
Sample 3B	Peel Ply Nylon + Breather Fabric	56.78%
Sample 4B	Perforated Release Film + Fiberglass	47.72%
Sample 5B	Perforated Release Film + Breather Fabric	49.18%
Sample 6B	Peel Ply Nylon + Fiberglass + Vacuum	56.59%
Sample 7B	Peel Ply Nylon + Breather Fabric + Vacuum	64.94%
Sample 8B	Perforated Release Film + Fiberglass + Vacuum	58.16%
Sample 9B	Perforated Release Film + Breather Fabric + Vacuum	66.43%

According to Table 3-1, the fiber mass fraction of the thermal protector samples without bleeder has already surpassed 56%. The addition of bleeder cloth did not affect the fiber mass fraction in the hand lay-up method. When peel ply was replaced by perforated release film, the fiber mass fraction decrease below 50% (Figure 3-1). The perforated release film is made of plastic therefore it did not adsorb the excess resin well enough compare to peel ply. Perforated release film allowed the fiber to adsorb more resin therefore the fiber mass fraction decreased. Nevertheless, breather fabric provided better adsorption as a second layer of bleeder when perforated release film was the first layer of the bleeder (sample 5B). The adsorption increase 1.46% from 47.72% to 49.18%. In opposite, neither fiberglass nor breather fabric increased the fiber mass fraction when peel ply was used as the first layer of the bleeder. When peel ply was used as the first layer, the excess resin has already been adsorbed in the peel ply thus the fiberglass and breather fabric cannot absorb more. Fiberglass was not a decent bleeder in the hand lay-up method. It poorly adsorbed the excess resin hence it decreased the fiber mass fraction.

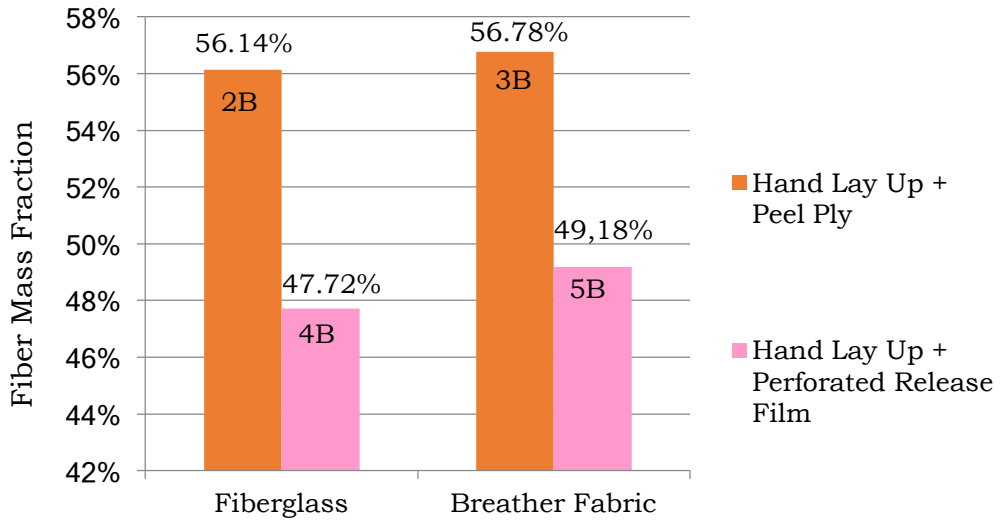

Figure 3-1: Fiber Mass Fraction Comparison on Hand Lay-up Manufacturing Process

When the vacuum was applied to sample 6 – 9, the fiber mass fraction increased significantly (Figure 3-2) from 56% to 66%. Whether the vacuum bagging method used peel ply or perforated release film, the fiber mass fraction increased. The interesting finding is that the perforated release film provided a higher fiber mass fraction than the peel ply. It is the opposite of the hand lay-up method. The pores throughout the film surface facilitated better excess resin transfer to the second layer bleeder (fiberglass and breather fabric). Similar to the hand lay-up method, fiberglass was not a decent bleeder

in the vacuum bagging method. Accordingly, it confirmed the fiberglass's poor adsorption ability as a bleeder. Breather fabric showed great performance in the vacuum bagging method.

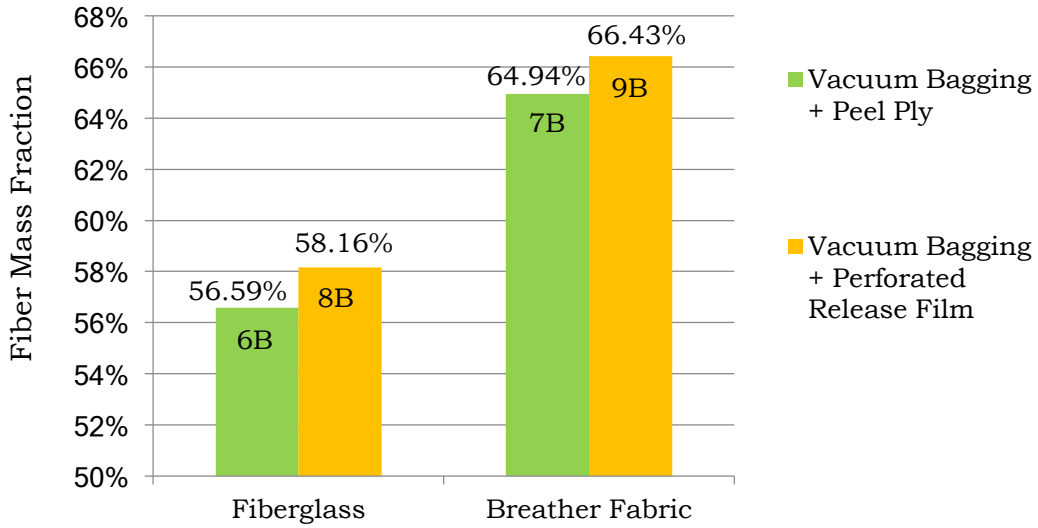

Figure 3-2: Fiber Mass Fraction Comparison on Vacuum Bagging Manufacturing Process

The composite surface topography was the author's concern because this work aims to eliminate sanding or filing as the surface preparation method for the lining process. The scanning electron microscope (SEM) analysis was performed after the removal of peel ply and perforated release film. Representative SEM images of the composite surface are shown in Figures 3-3 to 3-7.

Figure 3-3 is the surface of the thermal protector material without bleeder. This surface is different from any other surface. It has rich resin but the fiber pattern is seen. In some areas, fiber is not covered thoroughly with resin (red arrows). The yarn remnants were found imbedded in the surface (blue arrows). They were suspected to be left-out brush yarn or chopped fibers. EDS analysis should be performed to determine the source.

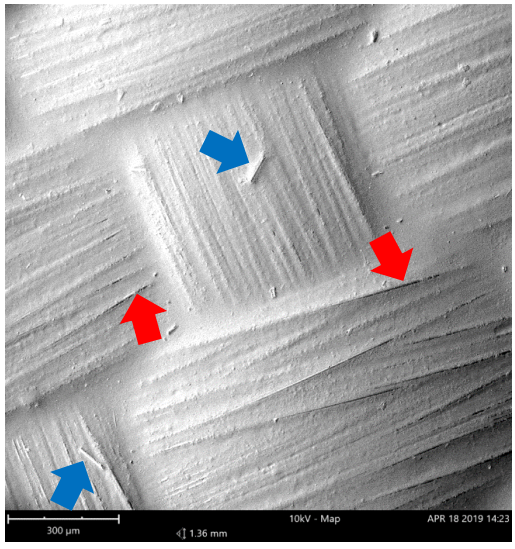

Figure 3-3: SEM Image of Composite's Surface Without Bleeder Cloth. The red arrows are fibers were not covered by resin, and the blue arrows are the yarn remnants that were embedded in the surface

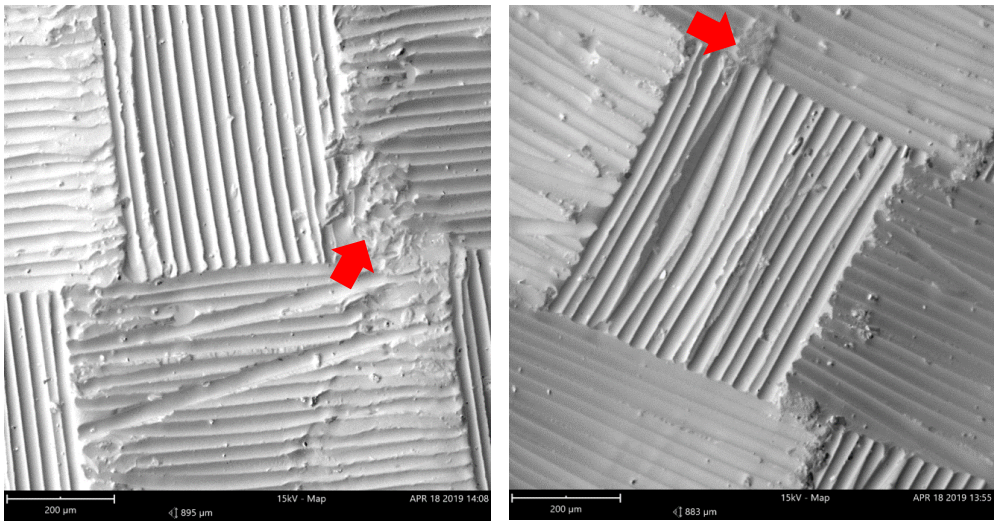

(a) 2B (b) 3B

Figure 3-4: Composite with Bleeder Schedule: (a) Sample 2B - Peel Ply & Fiberglass, and (b) Sample 3B - Peel Ply & Breather Fabric. The red arrows are ductile wisps on the epoxy surface.

Figure 3-4 is the comparison of the surface after the removal of peel ply - fiberglass (2B) and peel ply - breather fabric (3B). Both were manufactured by hand lay-up method. The imprints of the nylon peel ply weave are seen on the surface. The surface is fairly rough. Ductile wisps on the epoxy surface are also visible (red arrows). These are typical of a ductile polymer fracture (Flinn, 2007). 2B has more ductile wisps than 3B. Since tendrils are not present on the surface, it is likely that no remnants of the nylon peel ply fibers.

Figure 3-5 is the comparison of the surface after the removal of perforated release film - fiberglass (4B) and perforated release film - breather fabric (5B). They both were manufactured by hand lay-up method. There are no imprints seen on the surface. The surface is smooth with several voids. Several voids are likely air trapped below the perforated release film (red arrows). The imprints of the pores from perforated release film are seen as well on the surface (blue arrows). Also, the imprints of the plastics folding from uneven hand lay-up work are shown on the surface.

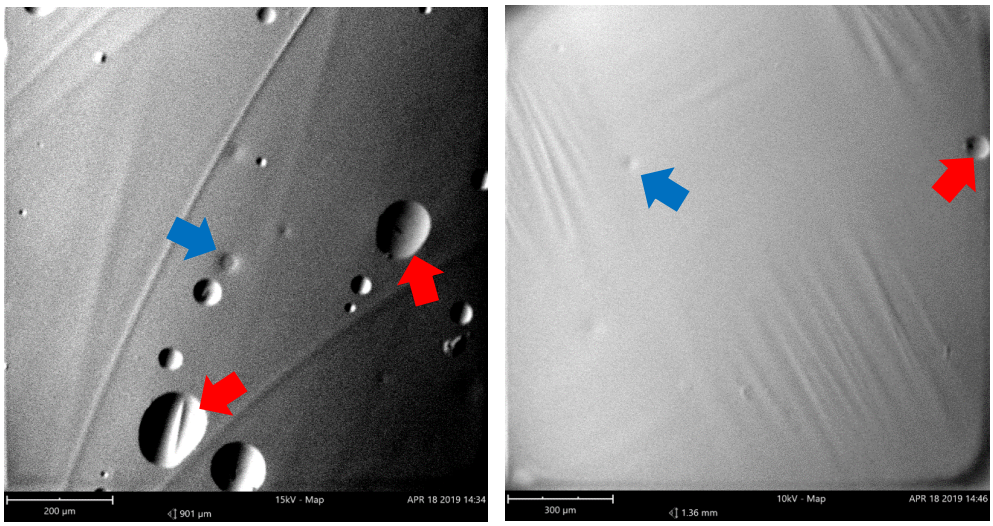

(a) 4B (b) 5B

Figure 3-5: Composite with Bleeder Schedule: (a) Sample 4B – Perforated Release Film & Fiberglass, and (b) Sample 5B – Perforated Release Film & Breather Fabric. The red arrows are imprints of the pores from the perforated release film, and the blue arrows are voids made from air trapped below the perforated release film.

Figure 3-6 is the comparison of the surface after the removal of peel ply - fiberglass (6B) and peel ply - breather fabric (7B) manufactured by vacuum bagging. The imprints of the nylon peel ply weave are visible on the surface. Few ductile polymer fractures are visible but not too large compare to Figures 3-4. Vacuum bagging reduces the existence of the ductile wisps. Figure 3-6 shows that 6B has more ductile polymer fractures than 7B. This indicates that breather fabric can adsorb more resin than fiberglass. It is shown in a higher fiber mass fraction of 7B than 6B. There are no remnants of the nylon peel ply fibers on both surfaces since tendrils are not visible.

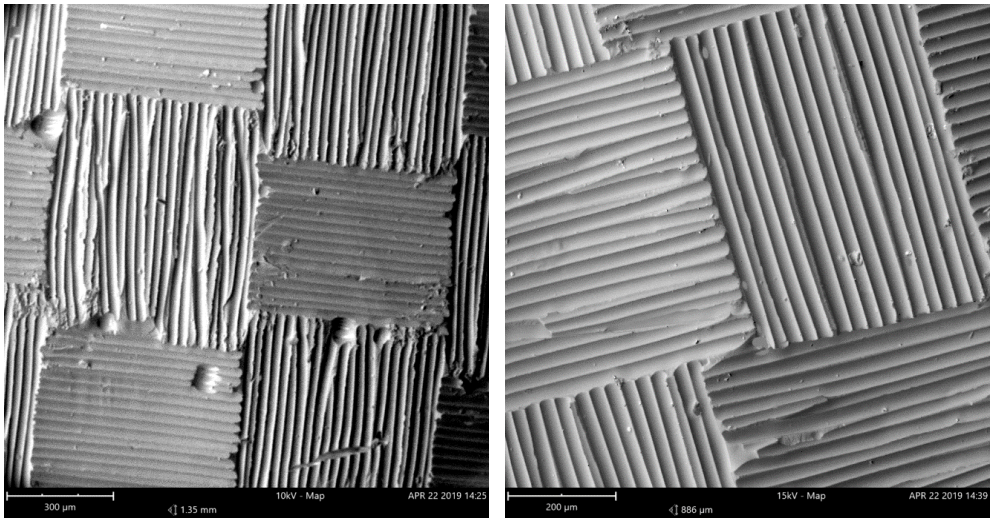

(a) 6B (b) 7B

Figure 3-6: Composite with Bleeder Schedule: (a) Sample 6B - Peel Ply & Fiberglass, and (b) Sample 7B - Peel Ply & Breather Fabric. Both were manufactured by vacuum bagging.

Figure 3-7 is the comparison of the surface after the removal of perforated release film - fiberglass (8B) and perforated release film - breather fabric (9B) manufactured by vacuum bagging. Similar to Figures 3-5, there are no imprints seen on the surface. Several voids are visible on 8B but there were not many compare to the previous one (Figure 3-5). Vacuum bagging reduces the existence of trapped air. The surface of the 9B is surprising. There are large voids with fibers on their bottom. During the vacuum condition, the resin was drawn out from the fiber's surface unevenly. It created those large voids.

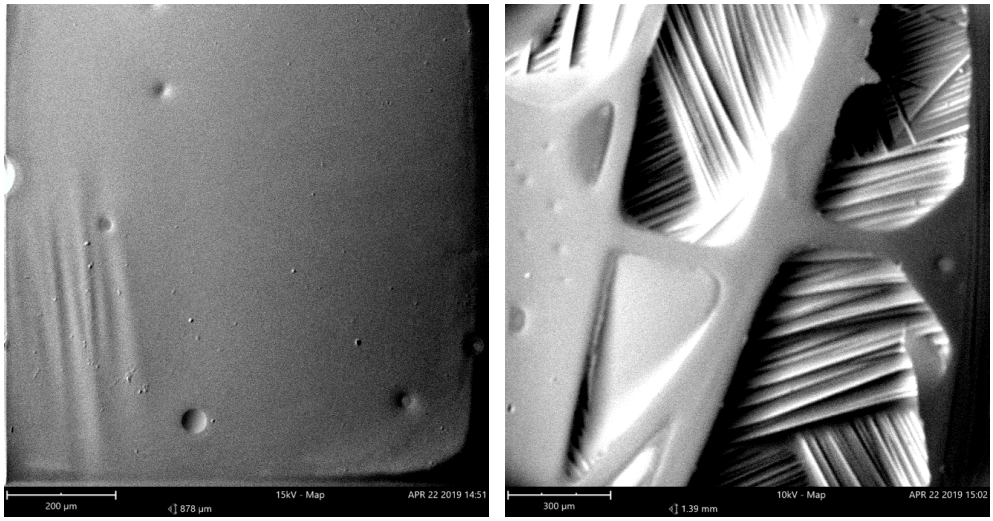

(a) 8B (b) 9B

Figure 3-7: Composite with Bleeder Schedule: (a) Sample 8B – Perforated Release Film & Fiberglass, and (b) Sample 9B – Perforated Release Film & Breather Fabric. Both were manufactured by vacuum bagging.

The ductile wisps and the tendril on the composite surface require further analysis by EDS (Energy Dispersive Spectrometry) or XPS (X-ray Photoelectron Spectroscopy) to confirm the source. Nylon peel plies usually coated with a release agent such as silicone, it is important to ensure that the silicone release agent is not transferred to the laminate's surface. The silicone will contaminate the surface, therefore, decreasing the bonding strength (Hart-Smith et al, 1996). EDS or XPS analysis should be performed to determine whether the silicone release agent is transferred to the laminates.

4. Conclusions

The highest fiber mass fraction (66.49%) was achieved by vacuum bagging manufacturing process with perforated release film and breather fabric bleeder schedule. Meanwhile, the lowest fiber fraction (47.72%) was achieved by hand lay-up process with peel ply and fiberglass bleeder schedule. The fiber mass fraction of thermal protector material manufactured by hand lay-up can reach a maximum of 56.78%, whereas vacuum bagging can reach a maximum of 66.43%. In terms of fiber mass fraction, peel ply and breather fabric combination are the best bleeder schedule for the hand lay-up method meanwhile perforated release film and breather fabric are the best bleeders for the vacuum bagging method. In both methods, breather fabric adsorbs more excess resin than fiberglass. Composite surface topography obtained from peel ply is visible on the surface. Meanwhile, the surface topography obtained from the perforated release film is not visible. This paper recommends peel ply usage in the thermal protector manufacturing process to replace the sanding or filling method that the author use nowadays.

Acknowledgements

This work was funded by the National Institute of Aeronautics and Space (LAPAN Indonesia) in 2019. The authors would like to show gratitude to Sutrisno for his guidance.

Contributorship Statement

WUD is the main contributor. Both WUD and RS did the experiment and analysis.

References

Abdurohman, K., Satrio, T., Muzayadah, N. L., & Teten. (2018). A comparison process between hand lay-up, vacuum infusion and vacuum bagging method toward e-glass EW 185/lycal composites. In R. Ramdani, S. F. Junjunan, & F. Kurniawati (Eds.), Proceedings of the 6th International Seminar of Aerospace Science and Technology. *Journal of Physics: Conf. Series, 1130*, 012018.

Amirkhosravi, M., Pishvar, M., & Altan, M. C. (2017). Improving laminate quality in wet lay-up/vacuum bag processes by magnet assisted composite manufacturing (MACM). Composites Part A: Applied Science and Manufacturing, 98, 227–237. doi:10.1016/j.compositesa.2017.03.032

Buchmann, C., Langer, S., Filsinger, J., & Drechsler, K. (2016). Analysis of the removal of peel ply from CFRP surfaces. *Composites Part B: Engineering*, *89*, 352–361. doi:10.1016/j.compositesb.2015.11.019

Dewi, W. U. (2014). Optimasi sistem lining motor roket padat RX1220 melalui perubahan komposisi material liner dan metode lining. *Jurnal Teknologi Dirgantara, 12*, 27-36.

Flinn, B. D., Clark, B. K., Satterwhite, J., & Van Voast, P. J. (2007). Influence of peel ply type on adhesive bonding of composites. Proceedings of the 52nd International SAMPE Symposium and Exhibition.

Flinn, B. D., Phariss, M. K. M., Ballien, B., Grace, W. B., & Van Voast, P. J. (2005). Peel-ply surface preparation variables and their effect on bond quality. Proceedings of the International SAMPE Technical Conference.

Gude, M. R., Prolongo, S. G., & Ureña, A. (2012). Adhesive bonding of carbon fibre/epoxy laminates: Correlation between surface and mechanical properties. Surface and Coatings Technology, 207, 602–607. doi:10.1016/j.surfcoat.2012.07.085

Hart-Smith, L. J., Redmond, G., & Davis, M. J. (1996). The curse of the nylon peel ply.

Proceedings of the 41st International SAMPE Symposium and Exhibition.

Holtmannspötter, J., Czarnecki, J. V., Wetzel, M., Dolderer, D., & Eisenschink, C. (2013). The use of peel ply as a method to create reproduceable but contaminated surfaces for structural adhesive bonding of carbon fiber reinforced plastics. The Journal of Adhesion, 89(2), 96–110. doi:10.1080/00218464.2012.731828

Jeswani, A. L., & Roux, J. A. (2010). Impact of fiber volume fraction and resin viscosity with die detached tapered chamber in resin injection pultrusion. Journal of Manufacturing Science and Engineering, 132(2), 021007. doi:10.1115/1.4001138

Kanerva, M., & Saarela, O. (2013). The peel ply surface treatment for adhesive bonding of composites: A review. International Journal of Adhesion and Adhesives, 43, 60–69. doi:10.1016/j.ijadhadh.2013.01.014

Kanerva, M., Sarlin, E., Hoikkanen, M., Rämö, K., Saarela, O., & Vuorinen, J. (2015). Interface modification of glass fibre–polyester composite–composite joints using peel plies. International Journal of Adhesion and Adhesives, 59, 40–52. doi:10.1016/j.ijadhadh.2015.01.016

Mund, M., Lippky, K., Blass, D., & Dilger, K. (2019). Influence of production based surface topography and release agent amount on bonding properties of CFRP. Composite Structures, 216, 104–111. doi:10.1016/j.compstruct.2019.02.026

Kim, S.-Y., Shim, C. S., Sturtevant, C., Kim, D. (Dae-W., & Song, H. C. (2014). Mechanical properties and production quality of hand-layup and vacuum infusion processed hybrid composite materials for GFRP marine structures. International Journal of Naval Architecture and Ocean Engineering, 6(3), 723–736. doi:10.2478/ijnaoe-2013-0208

Martínez-Landeros, V. H., Vargas-Islas, S. Y., Cruz-González, C. E., Barrera, S., Mourtazov, K., & Ramírez-Bon, R. (2019). Studies on the influence of surface treatment type, in the effectiveness of structural adhesive bonding, for carbon fiber reinforced composites. Journal of Manufacturing Processes, 39, 160–166. doi:10.1016/j.jmapro.2019.02.014

Shang, X., Marques, E. A. S., Machado, J. J. M., Carbas, R. J. C., Jiang, D., & da Silva, L. F. M. (2019). Review on techniques to improve the strength of adhesive joints with composite adherends. Composites Part B: Engineering, 177, 107363. doi:10.1016/j.compositesb.2019.107363

Such, M., Ward, C., Hutabarat, W., & Tiwari, A. (2014). Intelligent composite layup by the application of low cost tracking and projection technologies. 8th International Conference on Digital Enterprise Technology - DET 2014 – “Disruptive Innovation in Manufacturing Engineering towards the 4th Industrial Revolution. pp. 122 – 131. Procedia CIRP, 25. doi:10.1016/j.procir.2014.10.020

Sutrisno. (2011). Analisis bagian kritis pada pembuatan sistem insulasi termal motor roket LAPAN. Proceedings of the 15th Seminar Nasional IPTEK Penerbangan dan Antariksa (pp. 258-269).

U.S. Department of Defense. (2002). Composite material handbook, volume 1: Polymer matrix composite guidelines for characterization of structural material. Warrendale, PA: SAE International.

Wegman, R. F., & Van Twisk, J. (2013). Chapter 8 - Plastics. In J. V. Raymond F. Wegman, Surface Preparation Techniques for Adhesive Bonding (Second Edition) (pp. 115-130). doi:10.1016/b978-1-4557-3126-8.00008-7